GENERATION AND PROPAGATION OF OPTICAL VORTICES

by

David Rozas

A Dissertation
Submitted to the Faculty
of the
WORCESTER POLYTECHNIC INSTITUTE
in partial fulfillment of the requirements
for the Degree
of
Doctor of Philosophy
in
Physics

August 20th, 1999

APPROVED:

Dr. Grover A. Swartzlander, Jr., Dissertation Advisor

Dr. Alex A. Zozulya, Committee Member

Dr. William W. Durgin, Committee Member

ABSTRACT

Optical vortices are singularities in phase fronts of laser beams. They are characterized by a dark core whose size (relative to the size of the background beam) may dramatically affect their behavior upon propagation. Previously, only large-core vortices have been extensively studied. The object of the research presented in this dissertation was to explore ways of generating small-core optical vortices (also called *optical vortex filaments*), and to examine their propagation using analytical, numerical and experimental methods. Computer-generated holography enabled us to create arbitrary distributions of optical vortex filaments for experimental exploration. Hydrodynamic analogies were used to develop an heuristic model which described the dependence of vortex motion on other vortices and the background beam, both qualitatively and quantitatively. We predicted that pair of optical vortex filaments will rotate with angular rates inversely proportional to their separation distance (just like vortices in a fluid). We also reported the first experimental observation of this novel fluid-like effect. It was found, however, that upon propagation in linear media, the fluid-like rotation was not sustained owing to the overlap of diffracting vortex cores. Further numerical studies and experiments showed that rotation angle may be enhanced in nonlinear self-defocusing media.

The results presented in this thesis offer us a better understanding of dynamics of propagating vortices which may result in applications in optical switching, optical data storage, manipulation of micro-particles and optical limiting for eye protection.

To all who believed in me despite their good judgment

ACKNOWLEDGMENTS

To paraphrase Churchill, never in the history of graduate research has one person been grateful to so many. It is impossible to mention all the people who have helped me during the six years at WPI and I apologize in advance for not being able to acknowledge everyone.

I would like to thank my research advisor, Dr. Grover A. Swartzlander, Jr., for guiding me through the vast world of nonlinear optics. He taught me a great deal, from aligning lenses in the lab to aligning xeroxed paper sheets before stapling them, and a lot of things in between. It is a blessing to work for a man with vision and I was very fortunate in this regard.

I am also grateful to the members of my Graduate Committee, Dr. Alex A. Zozulya and Dr. William W. Durgin for taking the time to review and critique this work.

Zachary S. Sacks, a former WPI Master's student,[*] deserves a lot of credit for developing software to produce computer-generated holograms of optical vortices and designing the initial experimental setup for recording high-efficiency holograms.

I would like to acknowledge fruitful discussions with Anton Deykoon (WPI), Dr. Chiu-Tai Law (U. of Wisconsin, Milwaukee, WI), Dr. Marat S. Soskin (Ukraine Academy of Sciences, Kiev, Ukraine) and Ivan D. Maleev (WPI), as well as advice

---

[*] Now with the U. of Michigan at Ann Arbor

on optical experiment design from Dr. Adriaan Walther (WPI).

I would also like to thank Roger W. Steele for technical assistance and Severin J. Ritchie for designing and machining numerous gadgets for my experimental setups. Sev is a virtuoso craftsman and his talent is rare in this age of computer-controlled machine tools.

My grateful acknowledgments go out to WPI Department of Physics and its past and present Department Heads, Dr. Stephen N. Jasperson and Dr. Thomas H. Keil. From the moment six years ago when Dr. Jasperson called me in Lithuania to tell me about my being accepted to the graduate Physics program at WPI, I always felt the support of this Department in all my endeavors. Department's assistance, financial and otherwise, gave me the welcome security and peace of mind to concentrate on the research. I would also like to thank all the secretaries at Department of Physics who had to put up with me all these years: Earline Rich, Robyn Marcin and especially Susan Milkman, who transferred to another Department (after realizing I may never graduate and leave). Sue, you can come back now.

Research presented in this dissertation was supported[†] by the Research Corporation Cottrell Scholars Program, the U.S. National Science Foundation Young Investigator Program, Newport Corporation and Spectra-Physics.

I am grateful to my friend, Dr. Sergey B. Simanovsky, for finding me a job.

Most importantly, I would like to thank my parents, Misha and Feige-Taube Rozas, my brother Simon, and all the wonderful people who made me feel at home in this country: the Jaffees, Peter Stark, Phyllis Spool, Gloria Aisenberg, the Katz family and the Pemsteins. Thank you for your love and cooking.

[†] Principal Investigator: Grover A. Swartzlander, Jr.

CONTENTS

LIST OF FIGURES

SYMBOLS AND ABBREVIATIONS

Greek Symbols

α - light absorption coefficient.

β - phase modulation parameter.

β_{HWHM} - ratio of the beam size to vortex size.

Γ - circulation of the velocity field around a vortex in fluid.

Δn - characteristic nonlinear change in index of refraction.

η - period of an amplitude hologram measured in units of resolvable printer dots.

η_B - efficiency of a Bragg hologram.

θ - azimuthal cylindrical coordinate in real space.

Θ - azimuthal cylindrical coordinate of a vortex.

κ - strength of a fluid vortex (analogous to topological charge of an optical vortex).

λ - wavelength.

Λ - spatial period of an amplitude hologram *or* period of transverse modulation of a periodic field.

Λ' - fringe spacing of a thick phase hologram.

π - 3.141592654.

ρ - density of the fluid *or* the radial cylindrical coordinate in Fourier space.

σ_z,σ_{FT},σ_V - sign factors (± 1) in various phase expressions.

ϕ - azimuthal cylindrical coordinate in Fourier space.

ϕ_{V} - angular displacement of a vortex with respect to its initial position.

Φ - phase.

Ω - angular rate of rotation for a pair of vortices.

Roman Symbols

A, A_m - electric field amplitude.

D - heat diffusion coefficient *or* thickness of a hologram or mask.

d_{V} - separation of vortices in a pair.

E - electric field.

e - 2.718281828.

$\mathcal{FT}$ - Fourier transform.

floor() - “floor” function, floor(x) is equal to the largest integer equal or less than x.

f_x, f_y - transverse Cartesian coordinates in Fourier space.

G_{BG} - background field amplitude.

$\mathbf{H}_n()$ - Struve function of order n.

i - imaginary unit, $i = \sqrt{-1}$.

I - intensity of the electric field.

$I_\nu()$ - modified Bessel function of the first kind of fractional order ν.

$\Im()$ - imaginary part of a complex number.

$J_n()$ - cylindrical Bessel function of order n.

k - wavenumber.

$\vec{k}$ - wavevector.

$\vec{k}_\perp$ - transverse wavevector.

m - topological charge of an optical vortex.

n - index of refraction.

n_0 - linear index of refraction.

n_2 - nonlinear refraction index coefficient.

Δn - characteristic nonlinear change in index of refraction.

$N.A.$ - numerical aperture.

N_p - resolution of a laser printer.

$O()$ - proportional to the number of operations in an algorithm.

P - power.

Q - quality factor of a thick hologram.

R - radial cylindrical coordinate of a vortex.

$\Re()$ - real part of a complex number.

Sgn() - “sign” function: $\mathrm{Sgn}(x) = x/|x|$.

t - time.

T - temperature.

TEM_{ij} - transverse electromagnetic mode of order (ij).

u - electric field envelope.

$\vec{v}$ - velocity of a fluid.

v - speed of a fluid ($v = |\vec{v}|$).

w - radial size of a beam.

w_0 - radial size of a Gaussian beam at its waist.

w_{HWHM} - half-width at half maximum size of the beam.

w_{OVS} - radial size of a vortex soliton.

w_{r} - arbitrary scaling factor, used for large-core vortices.

w_{V} - radial size of a vortex.

x, y - transverse Cartesian coordinates in real space.

x_{NL} - transverse nonlinear scaling factor.

z - Cartesian coordinate along the optical axis.

z_{NL} - longitudinal nonlinear scaling factor.

Z_{V} - characteristic vortex diffraction length, $Z_{\mathrm{V}} = kw_{\mathrm{V}}^2/2$.

Z_0 - Rayleigh length of a Gaussian beam.

Z_T - Talbot distance.

Mathematical Symbols

$\vec{\nabla}$ - gradient operator (3-dimensional).

$\vec{\nabla}_{\perp}$ - transverse gradient.

∇^2 - laplacian operator (3-dimensional).

$\nabla_{\perp}^2$ - transverse laplacian operator.

1. INTRODUCTION

Vortices are fascinating topological features which are ubiquitous throughout the Universe. They play an important role in a great number of physical processes ranging from microscopic structure of superfluid helium[1–4] to global weather patterns[5] and possibly to formation of matter in the Big Bang.[6] Over the last decade potential applications have driven a surge of interest in vortices in optical fields owing to potential applications. In self-defocusing media an optical vortex (OV) induces a waveguide[7,8] which may be used for optical switching.[9] In linear optics OV's have been already utilized as "optical tweezers" to manipulate small objects.[10–12] OV's may also be useful for optical limiting purposes[13] or for optical data storage. From the physical sciences point of view our understanding of vortices in optical fields may provide insights into vortex behavior in other physical systems.

This thesis covers two main topics: (1) the generation of optical vortices and (2) vortex propagation in linear and nonlinear media. Several methods may be used to embed OV's onto a "background" beam, such as a Gaussian laser beam. These include mode-converters,[14] phase masks[7,15] and computer-generated holograms[16] (CGH's). In this work we describe only CGH's and phase masks. Using analytical, numerical and experimental methods we investigated the propagation of OV's and explained how the propagation of a vortex is affected by other vortices and by the background beam in which the vortex resides. The main contribution of the author of this dissertation and his collaborators is the investigation of small-core optical vortices, which were not considered before. Based on hydrodynamic analogies we predicted that small-core vortices will exhibit effective interactions *both* in linear and nonlinear media similar to the ones known for vortex filaments in a fluid. By applying the CGH technology to create, for the first time, arbitrary distribution of small-core optical vortices we were able to confirm our theoretical analysis. These novel results provide us with a better understanding of dynamics of propagating vortices potentially allowing the control of OV motion by modulating the background beam or introducing other vortices.

The chapters in this thesis are organized as follows. A brief historical account concerning optical vortices presented with a literature overview is given in Chapter 2. The generation of optical vortex filaments using computer-generated holography is described in Chapter 3. The fluid-like effective interactions between small-core vortices are discussed in Chapter 4, revealing that OV filaments may orbit one another at rates that are orders of magnitude larger than those having non-localized cores. Experimental observations and confirmations of this rotational enhancement are presented in Chapter 5. In Chapter 6 we discuss other effects in vortex propagation, including the influence of periodic background conditions and the optical analog of the Magnus effect. A brief overview of vortex filament motion in hydrodynamics is given in Appendix A. The numerical algorithm used to model the propagation of light in linear and nonlinear media is described in Appendix B. Finally, Appendix C describes the sign conventions for the optical vortex phase.

Parts of this thesis have been published in or submitted to the following journals:

1. D. Rozas, G. A. Swartzlander, Jr., "Vortex Rotation Enhancement in Defocusing Nonlinear Refractive Media", in preparation for Opt. Lett.
2. Z. S. Sacks, D. Rozas, G.A. Swartzlander, Jr., "Holographic formation of optical vortex filaments", J. Opt. Soc. Am. B **15**, 2226-2234 (1998).
3. D. Rozas, C. T. Law, G. A. Swartzlander, Jr., "Propagation dynamics of optical vortices", J. Opt. Soc. Am. B **14**, 3054-3065 (1997).
4. D. Rozas, Z. S. Sacks, and G. A. Swartzlander Jr., "Experimental Observation of Fluidlike Motion of Optical Vortices", Phys. Rev. Lett. **79**, 3399-3402 (1997).

and were presented at the following international conferences:

1. D. Rozas and G. A. Swartzlander, Jr., "Enhanced Vortex Rotation in Nonlinear Refractive Media", Quantum Electronics and Laser Science Conference '99, Baltimore, MD (May 1999).
2. INVITED: D. Rozas, C. T. Law and G. A. Swartzlander , Jr., "Vortex dynamics in linear and nonlinear media", Annual Meeting of Optical Society of America, Baltimore, MD (Oct 1998).
3. D. Rozas, Z. S. Sacks and G. A. Swartzlander, Jr., "Experimental observation of the fluid-like motion of optical vortices", Annual Meeting of Optical Society of America, Long Beach, CA (Oct 1997).

4. G. A. Swartzlander, Jr. Z. S. Sacks, X. Zhang, D. Rozas, and C. T. Law, "Formation and propagation of optical vortices", Digest of the International Quantum Electronics Conference, 1996 OSA Technical Digest Series, p. 31 (Optical Society of America, Washington, D.C., 1996).

2. HISTORY

The essential characteristic of a field vortex is the phase profile, given by $\Phi(r, \theta, z_c) = m\theta$, where (r, θ, z_c) are the cylindrical coordinates, z_c is the path of the vortex core, and m is a signed integer called the "topological charge". As one travels a full circle around the center of the vortex, the phase of the electric field changes by an integer factor of 2π* and thus the phase is continuous everywhere except for the path, z_c, where $r = 0$. At the center of the core the phase is an undefined singularity; it is physically acceptable since the intensity vanishes there. Assuming the path of the vortex lies on the optical axis, z, and adding a phase factor, $-kz$ to describe light propagating paraxially along z axis we obtain the phase $\Phi(r, \theta, z) = m\theta - kz$, where k is the wavenumber. In this case, the equiphase surfaces will have a form of helical spirals with a pitch of $m\lambda$, where λ is the vacuum wavelength. Thus, an OV is essentially a *screw dislocation* in the phase fronts of a light wave. In the plane, perpendicular to propagation, initial electric field envelope of a single vortex may be expressed as

$$u(r, \theta, z = 0) = A_m(r, z = 0) \exp(im\theta), \tag{2.1}$$

where the core is colinear with the optical axis, z, and A_m is a radially symmetric amplitude profile function.

---

* Unless noted otherwise the phase is measured in radians

Vortices or topological phase defects occur as particular solutions (Laguerre modes) to the wave equation in cylindrical coordinates.[17,18] These modes may be used to describe a radiating electromagnetic field.[19] Perhaps the most familiar example of an optical vortex (OV) is the TEM_{01}^{*} "doughnut" mode of a laser cavity.[20–23] Like all field vortices, this mode has an intensity profile characterized by a dark core extending through space. The diameter of the core is determined by the wavelength and the diameter of the cylindrical resonator. This vortex is an auto-normal solution of the wave equation - it propagates without changing its shape. In this regard it behaves very differently from small-core OV's or OV filaments which are the main objects of interest in this dissertation.

Unlike the aforementioned case of a single vortex, other physical systems may give rise to a number of vortices. For example, in large-area cavities multiple radiation modes are allowed by boundary conditions of the wave equation. Spontaneous birth and death, propagation dynamics of vortex modes and stable spatial structures in various resonators have been extensively explored.[24–37] In addition a number of vortex phenomena which may find applications in parallel data processing were investigated, including self-organizing pattern formation, spatial symmetry breaking and spatial multi-stability of solitons in laser cavities.[38–43]

While the presence of vortex modes in systems with cylindrical symmetry seems natural owing to the azimuthal nature of the vortex phase profile, it was somewhat surprising to find vortices in unbound systems. Early experiments in optics and acoustics found that field vortices are generated when the waves scatter from surface imperfections.[44–47] In their landmark 1974 paper Nye and Berry[44] showed that wave pulses reflected from rough surfaces will contain defects similar to the ones found in imperfect crystals: edge, screw and mixed edge-screw dislocations. Nye and Berry emphasized that their findings apply to any limited coherent wavetrains which travel in different directions and interfere. Indeed, laser speckle contains large numbers of randomly distributed OV's.[46]

The spatial position of the vortices described above could not be easily controlled - they either spontaneously appear at random locations or, as in the case of a "doughnut" mode, a single vortex appears at the center of the cavity. From the experimental point of view one would like to be able to produce arbitrary distributions of optical vortices. An innovative approach using computer-generated holograms (CGH's)[16, 48–52] has a number of advantages. It provides a complete control over the number, core size, locations and topological charges of the vortices, while allowing one to specify the phase and spatial resolution. In addition, CGH's can be made in low-cost production using readily available commercial high-resolution printing services. Bazhenov *et al.*[16] was the first to propose the following procedure. An interference pattern obtained by beating a beam containing vorticity with an off-axis plane wave is calculated by computer and transferred onto a transparency. A laser beam passed through this amplitude hologram will contain the calculated distribution of vortices in the first diffractive order. Heckenberg *et al.*[48] proposed a slightly different method, where the reference wave is co-linear with the signal wave. The resulting holograms are similar to spiral Fresnel zone plates. Our research group at WPI has applied Bazhenov's approach to design and produce CGH's of small-core vortices.[51, 52]

Most of the early research on OV dynamics has focused on large-core vortices.[53–59] Their amplitude function may be written as

$$A_m(r, z = 0) = (r/w_r)^m, \tag{2.2}$$

where w_r is a scaling factor, not affecting the size of the vortex. Indebetouw[57] obtained closed-form analytical solutions describing the propagation of an arbitrary combination of large-core vortices nested in a background Gaussian beam. Surprisingly, he found that only vortices with opposite topological charges affected each other's propagation. In the case of a beam containing an array of vortices with identical topological charges, the propagation of an individual vortex was not affected by the presence or the position of other vortices. Namely, as the beam propagated, the vortex array rigidly rotated, owing to the phase evolution of the background Gaussian beam. In the far field, the angular displacement of the vortices with respect to the center of the beam asymptotically approached 90° (the so-called Gouy phase[60,61]), while the dark cores of the vortices adiabatically diffracted with the beam. Since the large-core vortices are self-similar solutions of the paraxial wave equation, their intensity profile does not change upon propagation.

At the same time, seemingly surprising correlations and rules have been found by Freund *et al.*[62–75] in the topology of random Gaussian distributions of optical vortices. These correlations can be derived from certain fundamental physical assumptions. E.g., by requiring the electric field function to be single-valued (since multiply valued field functions are unphysical) Freund was able to prove the "sign principle". It states that there is a high probability of the near-neighbor vortices having opposite topological charges.[65] It was proven earlier by Zel'dovich *et al.*[76] that vortices with high topological charge are improbable in the speckle. Freund also showed that the positions of the phase defects alone exhaust the content of a Gaussian speckle field.[†]

[†] These results are valid for any random scalar field obeying circular Gaussian statistics, including light, electron and neutron waves.

In addition, Freund *et al.* reported extensive correlations between numerous near-neighbor vortex parameters (besides topological charge) and suggested the presence of an underlying ordered structure in the geometry of apparently random wave fields.[67]

Meanwhile, vortices were also being discussed in the context of nonlinear optics. The optical vortex soliton (OVS) was experimentally discovered by Swartzlander and Law.[7,77] Simultaneously, Snyder[8] discussed the possibility of self-guided dark nonlinear modes based on a waveguide analogy. The OVS is a robust (2+1)-dimensional spatial structure which can propagate without changing its size. It may be formed in self-defocusing medium from an initial phase singularity when the nonlinear index change in the medium compensates the effect of diffraction. It is interesting to note that in the experiment cited in Ref. 7 a phase mask with only minimal phase resolution - 3 phase steps ($0,\pi$ and 2π) was sufficient to induce the OVS in the medium. The soliton was not only observed in a beam initially containing vorticity: pairs of solitons with opposite charges were reported to form spontaneously from 1-D dark soliton stripes.[7,78–82] This mechanism was attributed to a Kelvin-Helmholtz type “snake” instability. Kuznetsov and Turitsyn[83] predicted that 1-dimensional solitons are stable with respect to small-period transverse modulation but become unstable when the modulation period is greater than the critical value, resulting in spatial turbulence.

As described above, the research on large-core vortices[53–59] showed that identical neighboring vortices did not affect each other’s propagation. On the other hand, theoretical and numerical work by Roux[84] and Rozas *et al.*[85] predicted that quasi-point vortices, or “vortex filaments”, may exhibit fluid-like effective interactions which were long known to be present for vortex filaments in liquids.[86–88] Namely, a pair of vortex filaments in a fluid rotates around the center of the pair with the angular rate of rotation proportional to the inverse square of vortex separation: $\Omega \sim 1/d^2$. Small-core vortex amplitude profile may be approximated as

$$A_m(r, z = 0) = \tanh(r/w_{\mathrm{V}}), \tag{2.3}$$

where w_{V} is the size of the vortex. The CGH technology has enabled us to observe experimentally[89, 90] the fluid-like interaction of quasi-point OV's in linear medium. Section 5.3 describes the experimental measurement of rates of rotation for quasi-point OV pairs, which were two orders of magnitude greater than the ones previously reported for pairs of large-core vortices. However, these high rotation rates for quasi-point vortices could not be sustained upon propagation as vortex cores overlapped owing to diffraction. In contrast, numerical simulations showed[85] that if OV core diffraction were arrested (as in nonlinear self-defocusing medium), these high rotation rates would be sustained over a larger propagation distance, resulting in a greater net angular displacement. Recent experiments, described in see Section 5.3 confirm this prediction.[91, 92]

Vortex birth from a beam with zero initial vorticity may be also achieved without this instability.[93–98] Ilyenkov *et al.* reported the birth of vortices from in self-focusing SBN crystal[95] and photorefractive $\mathrm{LiNbO_3:Fe}$ crystal[94] using an initially smooth elliptical Gaussian beam. This profile induces a Gaussian lens[‡] which causes aberrations in the beam by directing the light in the central region towards the edge of the beam, while focusing the peripheral light to the center. As the beam propagates, one may observe the birth, evolution and annihilation of quadrupoles of vortices ow-

---

[‡] A lens with optical thickness given by a Gaussian function, resulting in the central region and the periphery having opposite-sign curvatures.

ing to the symmetry breaking (ellipticity) of the beam. This effect was also observed in defocusing thermal liquid[98] and, earlier, in sodium vapor.[93]

Under strong illumination one may expect even more pronounced irregularities in the initially smooth beam. A new phenomenon of nonlinear Cusp Diffraction Catastrophe (CDC) was observed in the high-power regime. CDC's were well studied in linear media,[99–102] where they may be formed from thin elliptical annular light sources. In the case of the thermal liquid[98] the nonlinearity facilitates the formation of an elliptical bright annulus from the initial Gaussian elliptical beam, which then gives rise to a CDC.

As far as potential applications are concerned, one of the most important properties of an OVS is its inherent waveguiding effect.[8] In nonlinear defocusing medium, the dark vortex core and the bright area around it induce a high-index "waveguide core" and a low-index "waveguide cladding", respectively. This property may be useful in optical switching where the most important challenge is to control light with light. A proof-of-principle experiment, reported in Ref. 7, used a $\lambda = 514$ [nm] pump beam with an initial phase singularity to induce an OVS waveguide in nonlinear medium (thermal liquid). A probe beam ($\lambda = 632.8$ [nm]), was directed through the induced waveguide. In a more sophisticated experiment[9] a temporally modulated gate beam was added to simulate the transistor effect. At the output of the nonlinear cell the intensity of the probe beam was successfully controlled by the pump beam intensity.

Recent research on OVS's has been greatly benefited by earlier theoretical and experimental work on soliton solutions to nonlinear equations,[2,3,103,104] research on nonlinear propagation of light[105–115] and 1-dimensional dark and bright solitons.[116–121]

Preliminary analyses of the OVS[8,122,123] were followed by other theoretical investigations: vortex birth via nonlinear instability,[78,124–126] quantum nonlinear optical solitons,[127,128] stable[129,130] and unstable[129] polarization effects, higher-order nonlinearities,[131] propagation dynamics of vortices and vortex pairs,[81,85,132–137] propagation of vortex arrays,[138,139] and other effects.[140]

Experimentally, dark solitons were investigated in a number of nonlinear media, including slightly absorbing thermal liquid,[7,141] atomic vapors[81,93,133,142] and photorefractive medium[79,80,143–145] biased into the Kerr-like regime.[146] The photorefractive medium has certain interesting properties for nonlinear experiments. The magnitude and the sign of the nonlinearity may be controlled by changing the applied static electric field. Although the response time of this medium is generally on the order of $10-100\,[\mathrm{sec}]$, strong nonlinear effects may be observed. Photorefractive media do not respond as ideal Kerr media; e.g. they exhibit nonlocal response, inherent anisotropy and certain instability phenomena.[79] For example, Mamaev *et al.*[144] reported that a small vortex of unit topological charge is unstable in photorefractive medium and it is stretched anisotropically upon propagation. Anisotropy of the medium only supports oppositely-charged vortex pairs aligned perpendicularly to the direction of the applied electrostatic field,[144] otherwise the pairs tend to rotate to realign perpendicular to the field or coalesce and annihilate.

A weakly absorbing thermal liquid behaves as a Kerr-like saturable defocusing medium with nonlocal nonlinear response. In this medium, an “optical shock-wave” surrounding the vortex was observed[141] in certain regimes. When the initial size of the vortex is much greater than the size of the soliton for the particular nonlinearity of the medium, the OV shrinks dramatically upon propagation and a bright overshooting ring is formed around the dark core of the vortex. It is interesting to compare this regime to the case when the initial size of the vortex is matched to the nonlinearity of the medium and the soliton is formed without the change of the vortex size. In the latter case the shock-wave ring is not formed. Owing to the enhanced intensity in the shock region, the vortex core may be squeezed below the expected size. This squeezing may be useful in nonlinear waveguiding applications.

OV's have been successfully applied to improve "optical tweezers" setups,[12,147] where small objects are trapped and moved with focused laser beams. Potential applications include biotechnology, e.g. optical tweezer techniques have been shown to provide precise, minimally invasive and sterile means of manipulating bacteria in vivo.[148] The radiation pressure and angular momentum from OV's have already been used to trap and move small particles and atoms.[10–12,14,149–153] In addition the angular momentum of OV's has been used to rotate trapped particles[154] in an "optical spanner" experiment. 3-dimensional gradient-force optical tweezers without the use of OV's have been reported earlier,[155] however this type of trap can only capture particles having an index of refraction which is *higher* than that of the surrounding medium (unless a rotating beam setup is used[156]). In addition, biological objects manipulated by the trap are prone to thermal damage, since the trapped particle is located near the region of the highest intensity in the focused beam. On the other hand, the use of an OV at the center of the trapping beam leads a region of low intensity at the center of the beam. What is more, Gahagan[12,147] reported that the efficiency of the gradient-force OV trap is higher, compared to the "conventional" gradient-force trap. Another advantage of the OV trap is that it allows the trapping of *low-index* particles[157] and even simultaneous trapping of low- and high-index particles in the same trap.[153]

Fundamental studies of angular momentum in propagating OV beams[158] lead to theoretical and experimental investigation of angular momentum conservation in the following processes: sum-frequency generation (SFG), second-harmonic generation (SHG), optical parametric amplification (OPA) and down-conversion (DC). Dholakia *et al.*[159] have showed SHG for Laguerre-Gaussian beams, demonstrated the doubling of topological charge in the second-harmonic beam and proposed the conservation of the topological charge in the SHG process.

A year later, Beržanskis *et al.*[160] reported the conservation of angular momentum in the SFG process. In this experiment two Nd:YAG input beams ($\lambda = 1064[\text{nm}]$) with initial vorticity were directed through a KDP crystal under co-linear type-II phase-matching condition. The output SFG beam contained a vortex charge equal to the sum of input beam vortex charges. Ref. 160 also reported using optical OPA in a KDP crystal with the pump beam of zero vorticity. The latter case resulted in the idler and signal beams having opposite topological charges. The aforementioned SFG and OPA experiments by Beržanskis *et al.* may be considered to be the proof-of-principal demonstrations for the optical implementation of mathematical addition and multiplication by (-1), respectively. Recently, another experimental paper reported observations of OV's and Bessel beams in an OPA process, seeded by quantum noise.[161]

At the time of the writing of this dissertation, the question is still open whether the topological charge is conserved in a down-conversion (DC) process. In a recent paper Soskin *et al.*[162] suggested the conservation of the topological charge in a DC process. However, an experiment by Maleev *et al.*[163] has not showed any evidence of charge conservation. In this case, a CW Argon ion laser UV pump beam ($\lambda = 350\,[\mathrm{nm}]$) with charge $m = 1$ vortex was sent to a BBO crystal (under type-II phase-matching condition) and the DC process was seeded with quantum noise. The output ($\lambda = 700\,[\mathrm{nm}]$) beams did not appear to contain any vorticity. It is possible that the phase information of the pump beam was either lost in the down conversion process or distributed randomly between the signal and the idler beams.

An experimental observation of rotational Doppler-like effect owing to the properties of angular momentum in the vortex beams was reported by Courtial.[164] This paper describes an observation of a frequency shift in a beam containing angular momentum when the beam is rotated around its optical axis. A beam with topological charge m is sent into a Mach-Zehnder interferometer. After passing through a Dove prism rotating with angular velocity Ω, the signal beam is interfered with a stationary reference beam. Since the Dove prism had to be aligned to a fraction of a wavelength, an *optical* experiment using $\lambda = 3.2\,[\mathrm{mm}]$ (microwave) wavelength beam was designed with lenses and prisms manufactured from polyethylene. The output intensity of the two beam interference clearly displayed a dynamic beating, owing to the frequency shift, $m\Omega$, imparted onto the signal beam by the rotating prism.

3. GENERATION OF OPTICAL VORTEX FILAMENTS

3.1 Introduction

Optical vortices occuring in physical systems often have either random locations (as in laser speckle) or a rigidly defined position (as in a doughnut mode). Furthermore, the core size in such systems is not a free parameter. For experimental investigations of OV's, however, we need to control the position, charge, and size of an arbitrary number of vortices. Nanolithography may be used to create diffractive optical elements having sub-micrometer features; however, such masks are formidably expensive and are not readily available. Contact lithography may also be used, but this approach is labor intensive because many well-aligned master masks are needed to achieve adequate phase resolution. Fortunately, the advent of computer-generated holography (CGH) and the availability of high quality laser printers allows a fast, inexpensive means of producing vortex holograms.[16, 48, 51, 52] In fact, the degree of control afforded by optical means, combined with non-invasive measurement techniques, is unprecedented compared to other areas of physics where fluid vortices occur (e.g., superfluids and other Bose condensates).

As in fluids, vortices with various types of core functions may occur in optics (see Eqs. (2.2) and (2.3)) and thus, one may expect analogous differences in the propagation dynamics of, say, large-core and small-core OV's. Whereas large core

OV's have been previously studied,[56,57] we were the first to pioneer the dynamics of vortex filaments.[85,90] The propagation dynamics of OV's depends on the initial phase and amplitude structure. For example, although the phase profiles of the large-core OV and the vortex filament may be identical, the difference in amplitude functions give rise to distinctly different propagation dynamics,[85,90] as described in Chapters 4 and 5.

The objective of this chapter is to describe a method to achieve vortex filament sizes at least two orders of magnitude smaller than the overall beam size (for comparison, the ratio of the beam size to the vortex core size for a conventional "doughnut" mode of a laser is only ≈ 3). As described in Section 3.5, we succeeded in obtaining a ratio of ≈ 175. This chapter is organized as follows. We describe the phase and intensity profiles of an optical vortex in Section 3.2. In Section 3.3 we discuss the holographic representation of a point vortex on a digitized black and white amplitude hologram. We explain in Section 3.4 how spatial filtering affects the vortex core size. Since an amplitude CGH may not be suitable for nonlinear applications owing to poor efficiency and low damage threshold, one may use it to create a high efficiency hologram in a photopolymer, as discussed in Section 3.5. We present our measurements of the vortex core in Section 3.6. An alternative way of generating optical vortices using Diffractive Optical Elements (DOE) is briefly described in Section 3.7. Finally, we summarize our results in Section 3.8.

3.2 Optical Vortex

A monochromatic beam propagating in the z-direction and containing a single vortex transversely centered at the origin ($r = 0$) may be expressed by the scalar envelope function:

$$u(r, \theta, z) = A_m(r, z) \exp(im\theta) \exp\left[i\Phi_m(r, z)\right] \tag{3.1}$$

where (r, θ, z) are cylindrical coordinates with the optical axis aligned along the z-axis, m is a signed integer called the topological charge, Φ_m is the phase, and the field is assumed to oscillate as $\exp(i\omega t - ikz)$, where $k = 2\pi/\lambda$ is the wavenumber and λ is the wavelength. The equiphase surface of the propagating electric field, $m\theta - kz + \Phi_m = \text{const}$, defines a helix circling the z-axis with a pitch of $m\lambda$. For notational convenience, we shall assume $m > 0$ and $\Phi_m(z = 0) = 0$. The amplitude, A_m, is a real function which vanishes both asymptotically (for physical beams) and at the center of the vortex core: $A_m(r = 0, z) = A_m(r \to \infty, z) = 0$ for all z. The center of the vortex core is at the crossing of real and imaginary zero lines of the electric field ($\Re(u) = 0$ and $\Im(u) = 0$). The initial amplitude and phase profiles are depicted in Fig. 3.1. We denote the radial beam and vortex sizes w_0 and w_{V}, respectively. One can define a ratio of the beam size to vortex size, $\beta = w_0/w_{\text{V}}$, which significantly affects the vortex propagation dynamics, as described in Chapter 4. Large-core vortices correspond to $\beta \sim 1$. Although strictly non-physical, a "point vortex" is a conceptually useful construct whose core size is vanishingly small, at least in the initial plane, $z = 0$, such that the beam to core size ratio, $\beta = w_0/w_{\text{V}}$, approaches infinity (or at least w_0/λ).

An important attribute of the vortex is that its core remains dark as the beam propagates. This may be understood from the point of view of destructive interference between rays diffracted into the core. Let us consider a circle of infinitesimal radius centered on the vortex core. For each (arbitrary) point on this circle having a phase Φ there is a point with phase $\Phi + \pi$, symmetrically located with respect to the

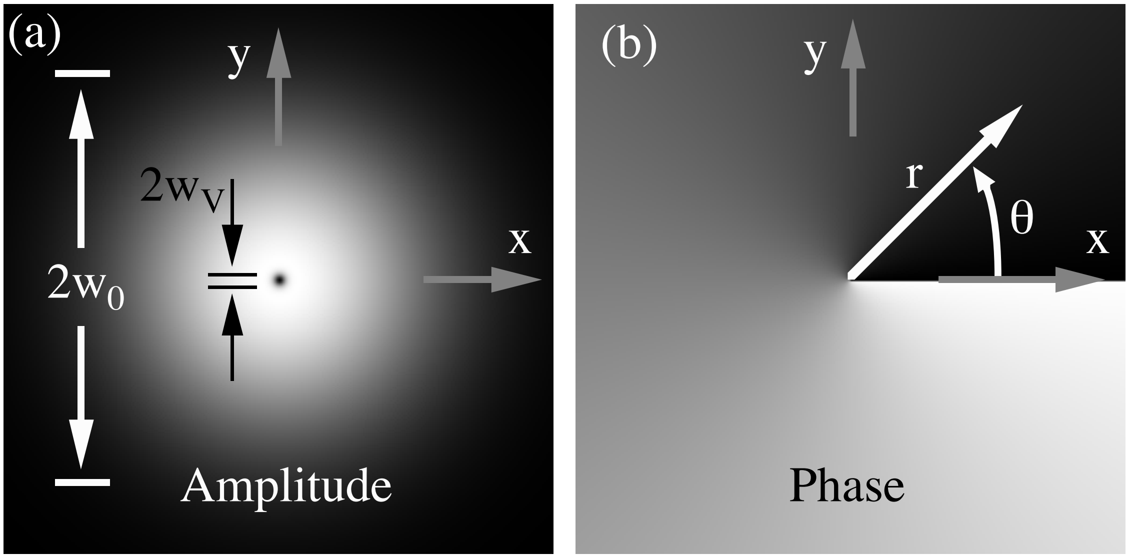

Fig. 3.1: Transverse profiles of an initial beam ($z = 0$) containing a vortex filament of topological charge, $m = 1$. (a) Intensity profile showing a dark core of diameter, $2w_\mathrm{V}$, on a Gaussian background field of radial size w_0. (b) Phase profile where black and white correspond to a vortex phase of zero and 2π, respectively. Logarithmic and linear gray-scale palettes are used to render (a) and (b), respectively.

center of the vortex. According to Huygens' principle[165] all points of the circle will radiate, giving rise to destructive interference owing to the π phase difference between symmetric points.

3.3 Computer Generated Holography

To construct a CGH of a vortex, we follow the approach of Bazhenov *et al.*,[16] and we numerically compute the interferogram of two waves: a planar "reference wave" and an "object wave" containing the desired holographic image. Here we choose the object wave to be a point vortex of unit charge on an infinite background field of amplitude C_1:

$$E_{\text{obj}} = C_1 \exp(i\theta), \tag{3.2}$$

and a reference wave of amplitude C_0, whose wavevector lies in the (x, z) plane, subtending the optical axis, z, at the angle ψ_1:

$$E_{\text{ref}} = C_0 \exp(-i2\pi x/\Lambda), \tag{3.3}$$

where $\Lambda = \lambda/\sin\psi_1$ is the spatial period of the plane wave in the transverse plane. The interferogram is given by the intensity of the interfering waves:

$$I_{z=0}(x, \theta) = |E_{\text{obj}} + E_{\text{ref}}|^2_{z=0} = 2C_0^2[1 + \cos(2\pi x/\Lambda + \theta)], \tag{3.4}$$

where we set $C_1 = C_0$ to achieve unity contrast $((I_{max} - I_{min})/I_{max} = 1)$. The resulting interferogram, depicted in Fig. 3.2, resembles a sinusoidal intensity diffraction grating. The pattern contains almost parallel lines with a bifurcation at the vortex core.

Note that Eq. (3.4) may be viewed as the power spectrum of the series

$$f(x, \theta) = \sum_{m=-\infty}^{\infty} C_m \exp(im\theta) \exp\left(\frac{i2\pi mx}{\Lambda}\right) \tag{3.5}$$

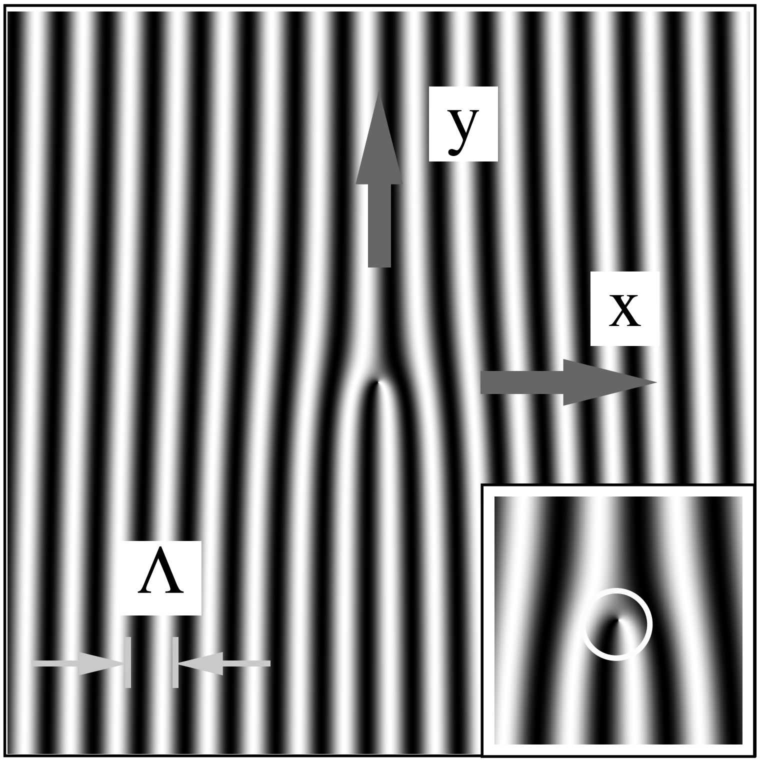

Fig. 3.2: Interferogram of a single point vortex of charge $m = 1$. The vortex core is located at the fork of the equiphase lines. Far from the core, the lines are separated by the grating period, Λ.

with $C_0 = C_1$ being the only nonzero coefficients.

A beam directed through an amplitude hologram of the form given in Eq. (3.4) will contain an infinite number of diffraction orders. In general, any interferogram represented by the function $|f(x,\theta)|^2$ in Eq. (3.5) will have a vortex of charge, m, diffracted into each of the m^{th}-order beams whose diffraction angle is given by the grating formula:

$$\psi_m = \arcsin(m\lambda/\Lambda), \tag{3.6}$$

where λ is the wavelength of light. The desired vortex image is contained in the $m = 1^{\text{st}}$ diffraction order beam.

Once Eq. (3.4) is numerically calculated and represented as a gray-scale image on a computer, it may be either photographed, or transferred to acetate film using a laser printer. The latter approach is favorable because commercial laser printers allow large format sizes without the need for high quality laboratory lens systems. Like photographic film, however, true gray-scale images are not possible with a laser printer; rather, the finest features appear as either black or white spots. To achieve high spatial resolution a binary hologram is used (see Fig. 3.3).

The algorithms used in this gray-scale to binary conversion were developed in our group by Zachary S. Sacks, and are described at the end of this section. High quality laser printers have a typical resolution of $N_p = 5080$ dots per inch (dpi), or $N_p = 0.2\ [\mu\text{m}]^{-1}$, which is small compared to holographic photographic film with $N_p > 1\ [\mu\text{m}]^{-1}$. In either case, the holographic image will suffer distortions from limited gray-scale and spatial resolution. A useful parameter in the study of these artifacts of CGH's is the unitless period of the hologram, as measured in units of

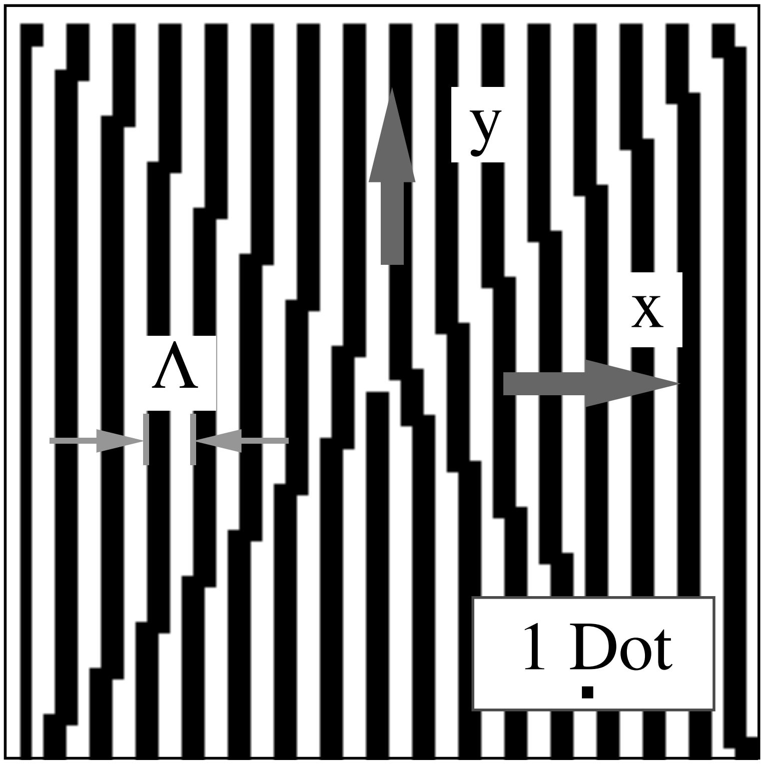

Fig. 3.3: Binary gray-scale rendering of Fig. 3.2, showing grating lines of width, $\Lambda/2$. The interference fringes are composed of line segments, resulting in $\eta = \Lambda N_p$ ($\eta = 4$ in this example) distinct phase domains whose boundaries radiate from the core, where N_p is the resolution of the laser printer (typically measured in "dots per inch").

resolvable "dots":

$$\eta = \Lambda N_p. \tag{3.7}$$

Let us first address the effects of the one-bit gray scale. A thresholding operation applied to Eq. (3.4) will result in a function that may be expressed as the modulus squared of the series Eq. (3.5). When the printed CGH is illuminated at normal incidence, a holographic image and its conjugate image may be found at the angles, ψ_1

and $-\psi_1$, respectively, with both subtending the z-axis in the xz-plane. In addition, multiple diffraction orders will also emerge at angles given in Eq. (3.6). That is, at each angle, ψ_m, one finds a beam containing vortex of charge m. Although this effect is quite remarkable to observe, the diffraction of light into multiple orders produces an undesirable effect: the efficiency of the first order is low ($\approx 10\%$)*, and spatial filtering is required to retrieve the desired holographic image. In the latter case, a large collection lens is used to focus the diffraction orders into separate spots in the focal plane, and an aperture is used to selectively transmit only the desired order. Spatial filtering is discussed in greater detail in Section 3.4.

Next we address the spatial resolution problem. Sampling theory dictates that $\Lambda > 2/N_p$, and experience suggests $\Lambda > 8/N_p$ for the printer used in our investigations: a Linotronic Hercules printer with $N_p^{-1} = 5$ [μm].† An examination of the printed lines and dots revealed 5 [μm] "dots" with a placement accuracy of 1 dot, as well as a minimum consistent line width of 20 [μm] (10 [μm] lines were randomly broken).[51, 52] We also found that lines drawn in the direction of the laser scan were straight, while perpendicular lines were wavy. This latter observation indicates that interferograms having nearly parallel lines, such as sparse vortex distributions, are well-suited for laser-printed holograms.

Small spatial periods are favorable for achieving a small vortex core size. That

---

[*] We define the diffraction efficiency as the ratio of the intensity of the $m = 1^{\text{st}}$ diffraction order with the total intensity of the incoming light. Assuming that the number of lines is high, the influence of the vortex will be negligible and we can use a well-known result for multiple-slit interference.[165] The efficiencies of the $m = 0, 1, 2, 3$ and 4 orders are approximately equal to 25%, 10%, 0%, 1% and 0%, respectively.

[†] Comp Associates. 80 Webster St., Worcester, MA 01603. Contact: Joe Cloutier.

is, large values of beam-to-core size ratio, β, require small values of hologram period Λ or η. This may be understood by considering that the resolving power of a grating is equal to the number of illuminated lines. If the vortex core is the smallest resolvable feature, as desired, then, in the diffraction limit, we may assume that the vortex diameter at the hologram is equal to the hologram period, $2w_{\rm V} \approx \Lambda$, and thus,

$$\beta = w_0/w_{\rm V} \approx 2w_0 N_p/\eta \gg 1, \tag{3.8}$$

where the beam diameter, $2w_0$, is assumed to be the effective diameter of the hologram. Although this ratio can be increased by simply increasing the effective size of the hologram, in practice this approach is limited by the size and quality of the lenses in the optical system. For example, our setup uses 3.15 [in] (8 [cm]) diameter achromatic lenses.

On the other hand, large values of Λ or η, as used in Refs. 16, 48, are required to achieve satisfactory phase resolution in the reconstructed electric field. This may be understood by considering that neighboring grating lines represent a 2π phase difference. Digitization of the space between these lines results in a digitized phase, with as many as η distinct phases over 2π radians (recall that η is also the number of printer dots per grating period). The phase resolution is therefore $N_\theta = \eta/(2\pi)$. Small values of η will yield a hologram whose ideally curved interference fringes appear instead as abruptly displaced line segments, as can be easily seen in Fig. 3.3 for the case $\eta = 4$. A vortex is essentially a phase object, and limiting the phase resolution will significantly affect the image quality. An appropriate value of η can be obtained from Eq. (3.8) once N_p and w_0 are known from experimental constraints, and once a desired value β has been selected. For example, if $N_p^{-1} = 5$ [μm], $w_0 = 25$ [mm], and $\beta = 200$, then $\eta = 50$. This will produce a core size of roughly $w_{\rm V} \approx \Lambda/2 =$

$\eta/(2N_p) = 125$ [μm] on a 50 [mm] diameter beam. Although to decrease the vortex size the holographic image may be optically reduced, β will not change significantly, since both the beam and the vortex will shrink.

Whereas spatial digitization and intensity thresholding are unavoidable artifacts which constrain the rendering of a laser-printed hologram, various techniques may be employed to draw the one-bit representation of the interferogram. For an accurate rendering, the CGH should be written as a command sequence which the printer can interpret. For many laser printers, the command language is PostScript[‡]. The CGH PostScript-encoded data files are frequently 10-100 times larger than its binary image file, although significant compression may be achieved by coding frequently used instruction sequences into a single instruction which can be defined in a PostScript dictionary in the file header. Further reduction may be achieved by drawing lines, rather than a sequence of dots, since the former has a smaller instruction set.

Various algorithms[51] may be used to convert the interferogram to a series of black and white line segments. We used a *thresholding* algorithm to calculate the intensity at every point in a grid and assign either a 0 or 1, depending on the value of a thresholding parameter (typically, this was set to one-half the peak intensity so that the black and white fringes have equal width). For a 1 [in^2] (6.45 [cm^2]) grid and $N_p^{-1} = 5$ [μm], this corresponds to $5080^2 = 2.6 \cdot 10^7$ data points, and is therefore computationally intensive. To accelerate the computation speed a *line-walking* algorithm was used in regions having no vortices. This code was designed to sweep in the x-direction along the edge of the grid, looking for a relative maximum; once found, it draws a single line of width $\Lambda/2 = \eta/(2N_p)$ in mostly the y-direction

---

[‡] PostScript is a trademark of the Adobe Corporation

along the relative maximum until reaching the other edge of the grid. This method allows a significant reduction in both the computational time and the size of the image file, although it may not be used in the vicinity of the vortex, since the interference fringes fork there. The speed of this algorithm can be improved by using a binary search method to find the end of a straight line segment, rather than following the relative maximum point by point along a line. In the vicinity of a vortex a *hybrid* algorithm was used: "thresholding" near the vortex and *line-walking* everywhere else.

3.4 Spatial Filtering

The effects of a finite spatial and gray-scale resolution in the CGH often require one to use spatial filtering techniques to (1) smooth out some distortion, and (2) select the desired diffraction order. Let us first examine the effects of phase distortion. We performed a numerical study by spatially filtering the CGH images in Fourier domain. We consider the $m = 1$ vortex field shown in Fig. 3.4(a). It is generated by a Gaussian beam passed through a binary hologram with a phase resolution of $\eta = 12$. The integer number η of distinct phases in the CGH will form phase domains, as discussed above, whose boundaries appear to radiate from the vortex core (see Fig. 3.3 and Fig. 3.4 (a)). In the near-field region, destructive interference along each domain boundary reduces the intensity by a factor of roughly $\cos^2(\pi/\eta)$. This has the effect of diffracting light into a star-burst pattern in the far field region, shown in Fig. 3.4 (b), with each arm separating neighboring phase domains. A circular aperture placed in the focal plane of a lens, as depicted in Fig. 3.4 (b), may be used to truncate the strongly diffracted components of this pattern. The filtered beam may then be re-imaged and recollimated using a second lens (see L_2 in Fig. 3.5). Numerical

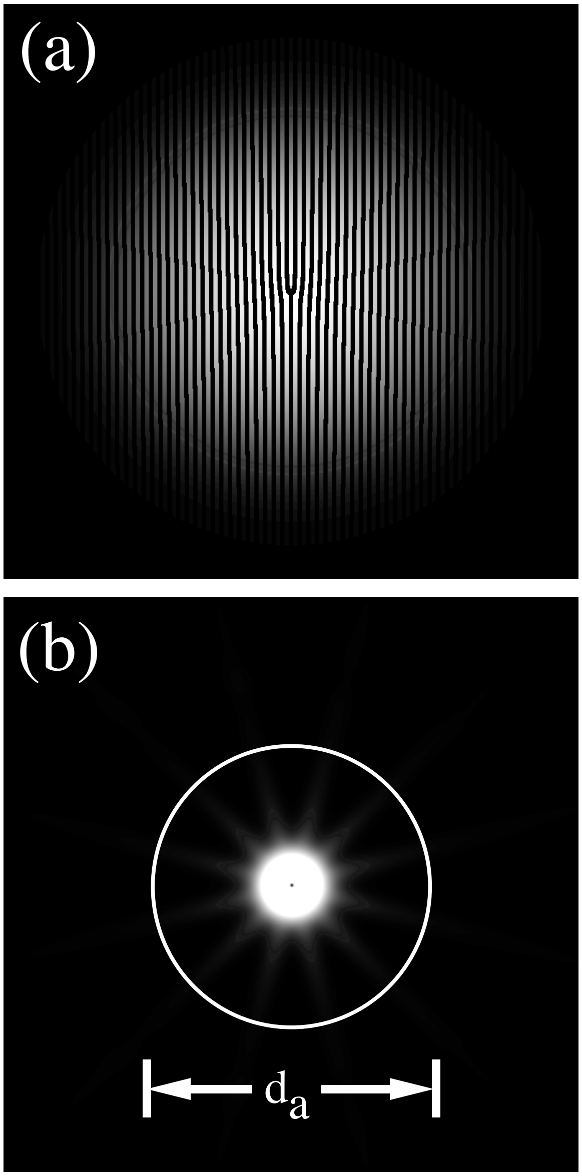

Fig. 3.4: (a) Intensity of the initial field used in our numerical study to explore the effects of spatial filtering. The field is created by passing a Gaussian beam through a CGH with $\eta = 12$. (b) Finite phase resolution in the CGH shown in (a) produces $\eta = 12$ arms radiating from the vortex core in the focal plane of a lens. An aperture of diameter, d_a, may be used to spatially filter the holographic image.

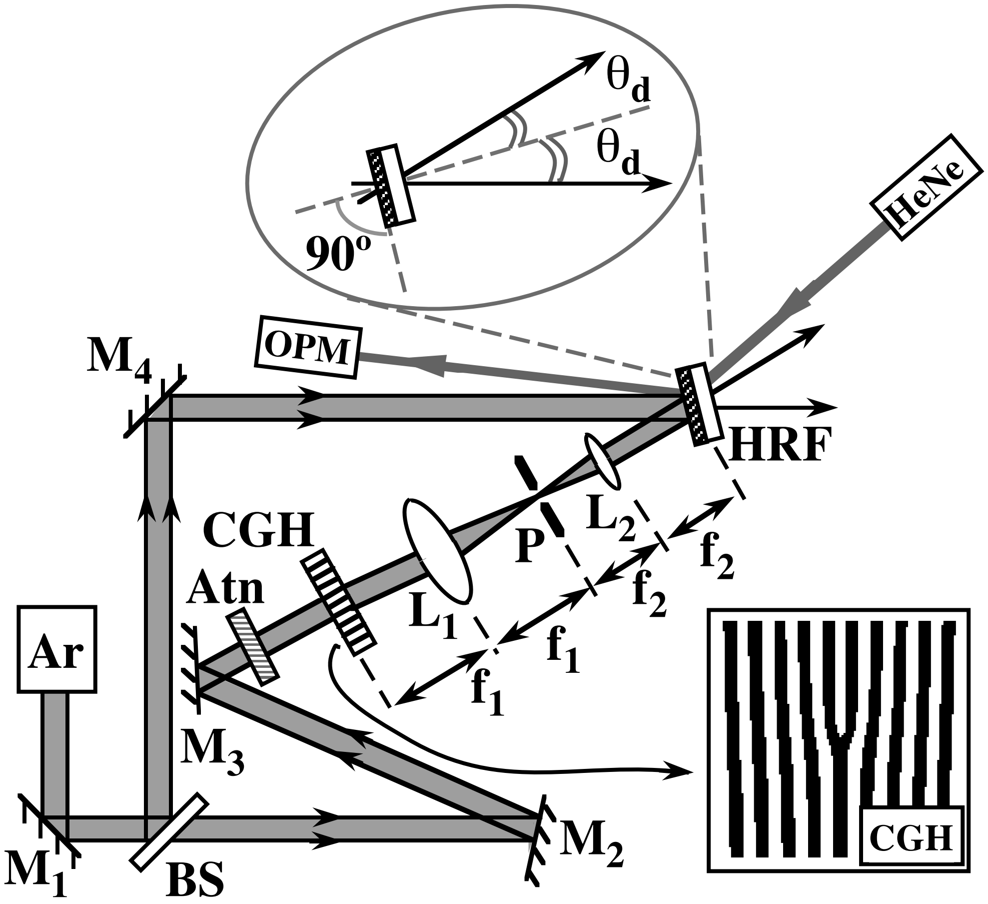

Fig. 3.5: Schematic of the optical system for converting the CGH into a thick phase hologram. A beam from a Spectra-Physics frequency stabilized argon ion laser (Ar) is directed through a glass wedge beam splitter (BS). The Object Beam is transmitted through the computer- generated hologram (CGH), and the first-order diffracted beam is allowed through a pinhole (P) in a spatial filter assembly. The Object and Reference Beams are balanced with the aid of an attenuator (Atn) and made to interfere at equal angles, θ_d, with respect to the normal of the holographic recording film attached to a glass window (HRF). A Helium-Neon laser (HeNe) and an optical power meter (OPM) are used to monitor the efficiency of the hologram in real time.

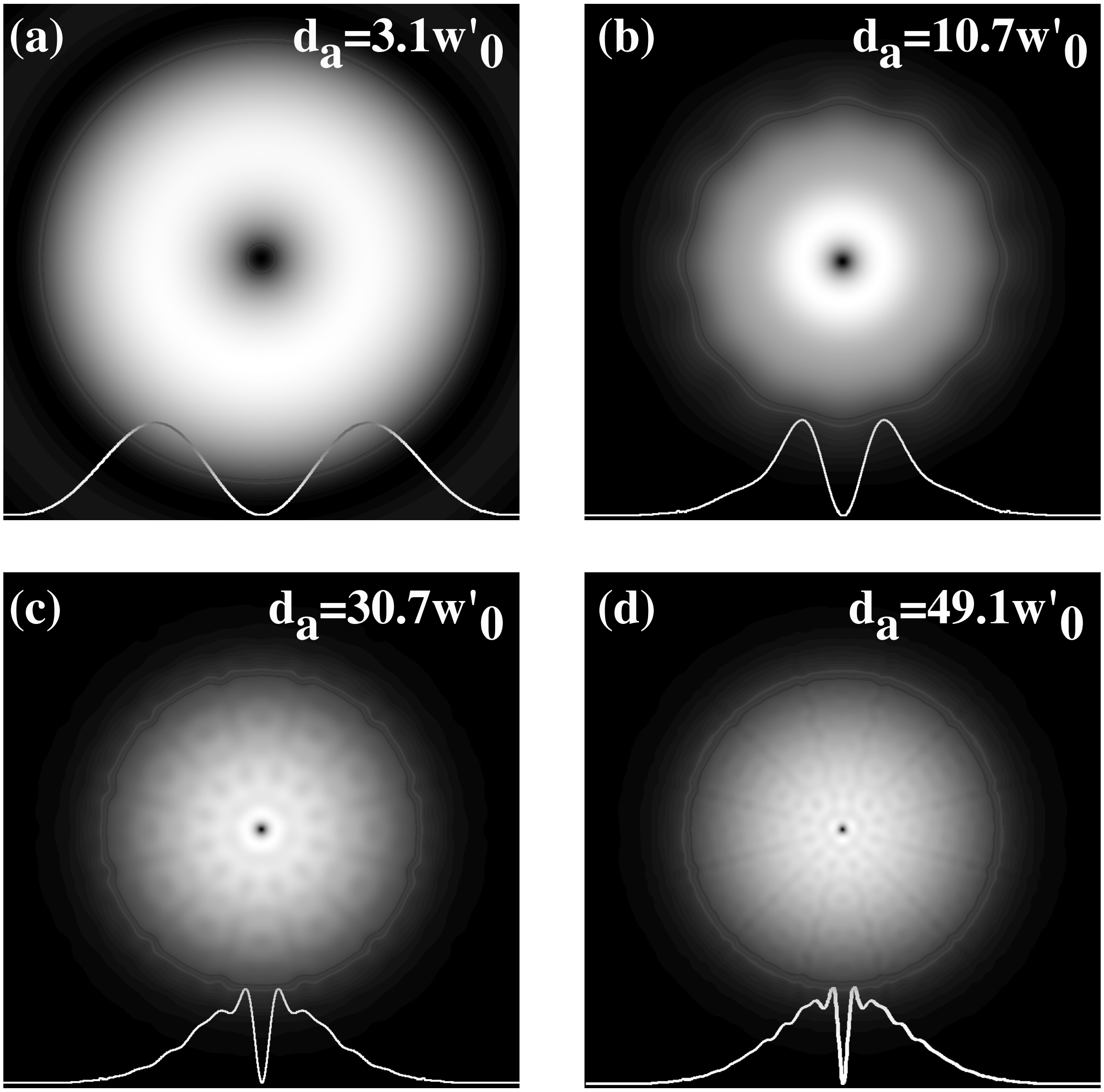

Fig. 3.6: The intensity of the field after spatial filtering of the CGH shown in Fig. 3.4 for 4 values of focal aperture, d_a, in units of w_0': (a) 3.1, (b) 10.7, (c) 30.7, (d) 49.1. Note that as the aperture size increases, the vortex size is reduced, however, the artifacts due to the binary nature of the CGH become visible.

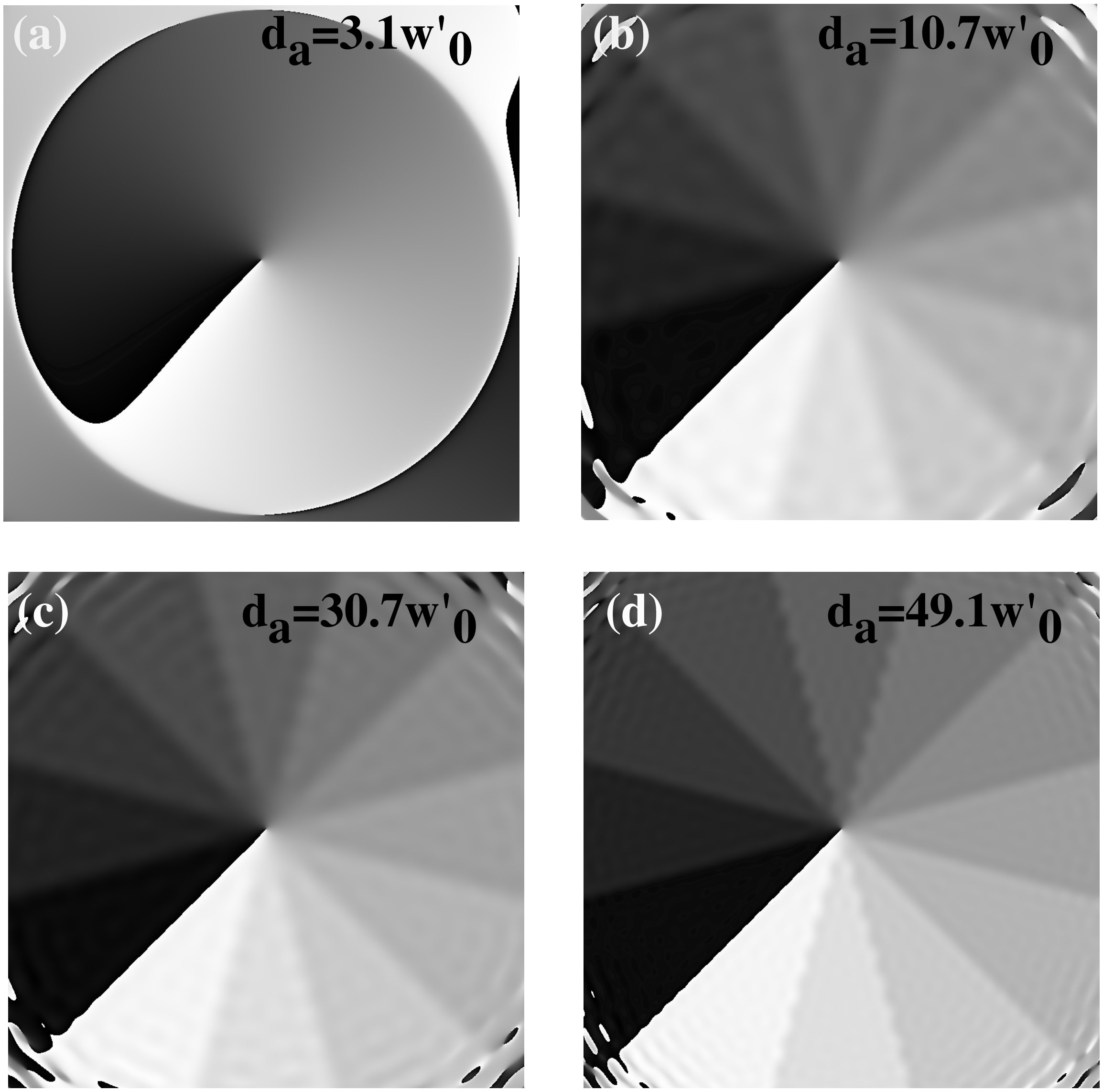

Fig. 3.7: The phase of the field after spatial filtering of the CGH shown in Fig. 3.4 for 4 values of focal aperture,d_a, in units of w_0': (a) 3.1, (b) 10.7, (c) 30.7, (d) 49.1. As the aperture size increases, the $\eta = 12$ phase steps and phase distortions become more pronounced. In (a) the limited phase resolution of the CGH is virtually eliminated owing to the small aperture size.

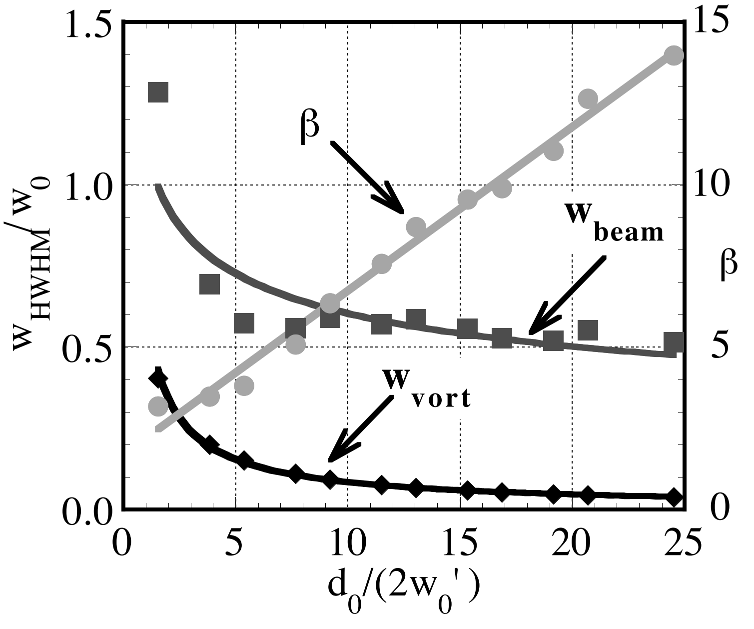

Fig. 3.8: The effect of aperture size on the beam to core size ratio, β_{HWHM}. The data points represent numerical experiments. The line fits are depicted by smooth curves.

results, demonstrating the effect of filtering, are shown in Fig. 3.6 and Fig. 3.7 for the field intensity and phase, respectively. The diameter of the filtering aperture is measured in units of the size of the Gaussian beam with no vorticity in the focal plane, $w_0' = \lambda f / \pi w_0$, where f is the focal length of the lens. A large diameter aperture allows the transmission of high spatial frequencies, and thus, a small vortex core is produced, although the beam exhibits faint stripes radiating from the core, as shown in Fig. 3.6 (c,d). On the other hand, the stripes disappear when a small aperture is used (see Fig. 3.6 (a,b)); however, both the vortex core and the beam size are now larger than in Fig. 3.6 (c,d). Also, in Fig. 3.7 (a) one can see the smoothing out of the phase steps owing to a small aperture. Numerically determined measurements, plotted in Fig. 3.8, indicate that the vortex core size is inversely proportional to the aperture size. This result is expected, owing to the convolution of the vortex beam with the Fourier transform of the aperture function (the latter being an Airy disk). For example, an ideal point vortex would have a diffraction limited size of order $w_{\text{lim}} = 1.22\lambda f/d_a$. Furthermore, we find that the numerically measured beam-to-core-size ratio, β_{HWHM}, increases linearly with the aperture diameter. The reason for this is that the high frequencies transmitted by a large aperture contribute to sharp features, namely the vortex core, but have little effect on smooth features such as the size of the beam. Not surprisingly, we see that large apertures are preferable to achieve large values of β. Fortunately, we find no fundamental upper limit to the value of β, and the only practical limit is dictated by the size of the optics and the hologram itself.

In practice, one may establish upper and lower bounds for the diameter of the spatial filter aperture, d_a, based on a vortex having infinite phase resolution. A lower limit may be set to the diffraction limited spot size in the focal plane:

$$d_{a,\text{min}} = c_b \lambda f / w_0, \tag{3.9}$$

where c_b is a constant that depends on the initial beam shape. Gaussian and pillbox beams are the typical beam profiles used for experiments with point-like vortices. c_b equals $1/\pi$ for a Gaussian beam, 0.61 for a pillbox beam (of radial size, $R = w_0$). Such a small pinhole will, however, significantly apodize the beam in the focal plane, and broaden the core (and the beam) in the image plane. The vortex beam intensity profiles in the focal plane are shown in Fig. 3.9 for Gaussian and pillbox background beams. An optimal minimum size for the focal pinhole may be estimated by qualitatively examining Fig. 3.9. For the Gaussian case (with $m = 1$), the tail in the focal plane is considerably extended, with the intensity falling to 1% of its maximum at roughly $r_f/w_0' = 3.5$. As a benchmark, one may desire $d_a \geq 7w_0'$.

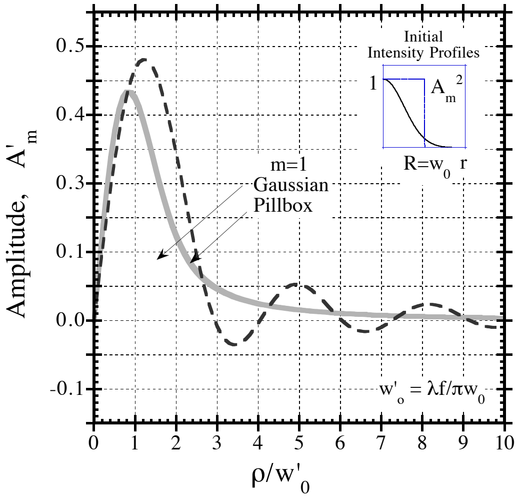

Fig. 3.9: Radial intensity distributions in the focal plane for an initial point vortex ($m = 1$) on Gaussian and pillbox beams, with characteristic sizes, w_0 and $R = w_0$, respectively. The radial coordinate is scaled by the diffraction limited spot size, $w_0' = \lambda f/\pi w_0$, and the amplitude is scaled by the optical gain factor, w_0/w_0'.

For the pillbox case, the intensity has its first zeros at roughly r_f/w_0', equal to 3, 4, and 6, and the intensity ringing subsides to $< 1\%$ of its maximum at roughly $r_f/w_0' = 5.4$. Thus, for pillbox background fields, one may wish to choose apertures having $d_a \geq 12w_0'$. The aperture should not be made too large, however, if one wishes to filter out unwanted diffraction orders. An upper limit of the aperture size may be set to the distance between neighboring diffraction orders:

$$d_{a,\max} = f \tan\psi_1 \approx f\lambda/\Lambda. \tag{3.10}$$

Unfortunately, even this maximum aperture will affect the vortex core size by filtering out the high spatial frequencies. This may be understood by the following argument. The diffraction limited vortex core size produced by the CGH is $w_{\mathrm{V}} \approx \Lambda/2$. The effect of the spatial filter in the image plane is to perform a convolution of the holographic object with an Airy disk. If the radial size of the Airy disk, $1.22\lambda f/d_a$, is much smaller than the features in the holographic object, then the image and the object will be nearly identical. To meet this condition, we desire $\Lambda/2 > 1.22\lambda f/d_a$. However, this inequality can not be satisfied for $d_a = d_{a,\max}$. At best, the Airy disk will be 2.44 times larger than $\Lambda/2$. We note that the vortex core will not only broaden, owing to spatial filtering, but it will also exhibit an overshoot, seen in Fig. 3.6 (c,d), attributed to the Gibbs phenomenon.

Let us again consider a hologram having a finite phase resolution. If we select $d_a = d_{a,\max}$, then the image will contain lines of phase and amplitude distortion. If we select a smaller aperture, the beam to core size ratio will become smaller. One must therefore make a qualitative judgment. After experimentally observing the effects of several apertures, we found that a 35 [μm] diameter pinhole ($d_a \approx 18w_0$) was most suitable for our optical system, which comprised a pillbox beam of radius, $R = 25$ [mm], a wavelength, $\lambda = 0.514$ [μm], and a lens of focal length, $f = 310$ [mm] and a CGH with $\eta = 16$ and $\Lambda = 80$ [μm].

3.5 Phase Hologram Conversion

Although the CGH is relatively simple to produce, it is not suitable for experiments requiring an intense laser beam. The CGH absorbs roughly half the beam power, and is therefore prone to damage. Furthermore, only 10% of the input power goes into the desired 1^{st} diffraction order. Increased efficiency and higher damage thresholds may be achieved using a thick phase, rather than a thin amplitude hologram. Here we describe a method of recording the CGH image onto a photopolymer medium.[51]

The experimental arrangement is shown in Fig. 3.5. The beam from Ar ion laser is divided into a “signal” and “reference” beams by a beamsplitter (BS). The signal beam is directed through a CGH at normal incidence. After spatial filtering the 1^{st} diffraction order of the CGH image, we interfere the signal vortex beam with the reference wave to create fringes to be recorded onto holographic photopolymer film (HRF).

Special care was taken to eliminate factors which may deteriorate the quality of the holographic recording: we used an optical table with tuned damping to reduce vibrations and isolated the experimental setup by a plastic enclosure to eliminate air currents. The reference beam was oriented to obtain a finer grating period, Λ', than could be achieved with the CGH.

The goal of our holographic recording setup (see Fig. 3.5) is to obtain a thick, Bragg type hologram. For this hologram nearly all the light may be diffracted into the first diffraction order, which occurs at the angle, θ_d, given by the diffraction equation, $\lambda = \Lambda'(\sin\theta_d - \sin\theta_i)$, where θ_i is the angle of the incidence of both the object and reference waves with respect to the normal of the film, and $\theta_d = -\theta_i$ (see Fig. 3.10). Thus, θ_d and Λ' are related by $\sin\theta_d = \lambda/(2\Lambda')$. The angle used in our experiment was $\theta_d = 13.3^\circ$, which provided a grating period of $\Lambda' = 1.12$ [μm].

The criterion used to judge whether the hologram is a high-efficiency thick Bragg type or a low-efficiency thin Raman-Nath type hologram is given by the quality factor:[166]

$$Q = \frac{4\pi D\theta_d}{\Lambda'} \approx \frac{2\pi\lambda D}{n(\Lambda')^2}. \tag{3.11}$$

The manufacturer reports a film thickness of $D = 38$ [μm], and a nominal refractive index of $n \approx 1.5$. Holograms having, $Q \gg 1$, have high diffraction efficiencies. Using the parameters of our investigation, we calculate $Q \approx 65$, and thus a high

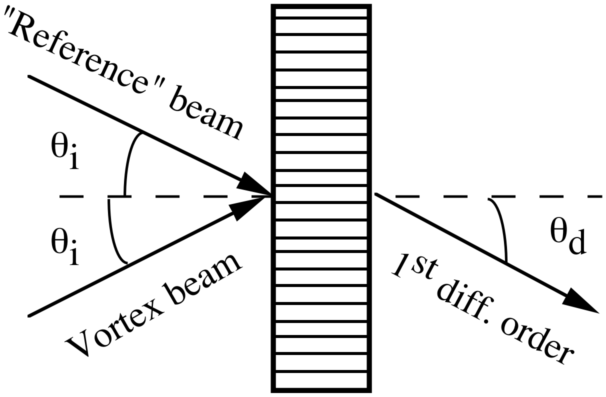

Fig. 3.10: The geometry of recording a hologram onto a photopolymer film. During recording exposure the “reference” and “signal” (vortex) beams are incident on the film. The equality of angles of incidence results in holographic fringes perpendicular to film surface. To reconstruct the recorded image a single reference wave is sent at the same incident angle, producing the desired image in the 1$^{\text{st}}$ diffracted order.

diffraction efficiency may be expected. The efficiency of a Bragg hologram, η_B, may be estimated from the well-known result for a thick sinusoidal phase grating, obtained by Kogelnik:[166]

$$\eta_B = \sin^2\left(\frac{\pi D\Delta n}{\lambda\cos\theta_d}\right), \tag{3.12}$$

where Δn may be as large as 9×10^{-2} in the photopolymer film.[167] The efficiency may theoretically reach unity when the exposure induces an index change of $\Delta n \approx 7\times10^{-3}$.

For the DuPont$^{\text{TM}}$ HRF-150X001-38 film we used the manufacturer suggests an exposure fluence of $F \approx 80$ [mJ/cm^2] and they claim to have achieved a diffraction efficiency of 99%. If the intensities of the vortex and reference beams are balanced and the average intensity at the film is $I_{\text{ave}} = 5$ [mW/cm^2], then the maximum index modulation should develop in a time $T_{\text{exp}} \approx 16$ [s]. We found that at that intensity, much higher exposure times, $T_{\text{exp}} \approx 140-190$ [s] were required (this may be attributed to the age of the holographic film which has a shelf life of 6 months). We obtained diffraction efficiencies as high as 70% for film that was more than 4.5 years old.

The Holographic Recording Film HRF-150X001-38 is comprised of a polymer layer coated onto to a mylar base sheet.[167,168] According to DuPont, the polymer coat is formed by drying a solution of monomers, photoinitiators, polymeric and polymerizable binders and a sensitizing dye. When illuminated with $\lambda = 514$ [nm] light the monomers polymerize in the regions of high intensity. Also, monomers from dark regions diffuse into the nearby high-intensity regions. This diffusion length places an upper limit on the holographic fringe spacing. The manufacturer suggests setting the fringe spacing $\Lambda' \leq 5[\mu\mathrm{m}]$ to insure that monomers diffuse into the exposed regions to enhance the density of the refractive index grating. As the exposure continues, the polymer gradually hardens arresting further diffusion. We used the standard after-exposure treatment, consisting of an incoherent UV-radiation curing and a 2-hr baking at 100°C.

To achieve a high diffraction efficiency, it is advantageous to calibrate the exposure process by monitoring the diffracted power as a function of time while a hologram is being exposed. For this purpose, we used a weak He-Ne probe laser with a wavelength of 0.6328 [μm] and diffraction angle of 16.7°. To monitor the diffraction efficiency we used National Instruments LabView$^{\mathrm{TM}}$ software package with a Model-835 Newport$^{\mathrm{TM}}$ Optical Power Meter (OPM) connected to a Macintosh$^{\mathrm{TM}}$ IIfx computer through a GPIB data acquisition board. The following calibration procedure was used. A calibration hologram was recorded and the He-Ne diffraction efficiency was plotted as a function of the exposure time. A typical plot, shown in Fig. 3.11, indicates that the highest diffraction efficiency requires an exposure of ≈ 70 [s]. From the

Eq. (3.12), which gives the inverse relation between the hologram efficiency and the wavelength we can see that the peak efficiency of the Argon laser beam is expected to occur when the He-Ne efficiency is at roughly 94%. However, experimentally we often found that exposures that were twice as long would give higher diffraction efficiencies. These discrepancies may also be attributed to the age of the film. It is important to point out that the diffraction efficiency for the Ar beam was of an order of $30 - 40\%$ after the exposure and UV curing and only after baking it was enhanced to $60 - 70\%$.

Let us now discuss the spatial features of the image recorded onto the photopolymer film. In the focal plane of lens L_2 we have obtained a vortex of size $w_{\text{HWHM}} \approx 145$ [μm] ($\beta \approx 175$). However, since the size of the holographic film was smaller than the cross-section of the signal and reference beams, the ratio β of the vortex recorded onto HRF was ~ 3 times smaller than 175. This particular hologram has been used in the measurements described in the next Section. Since this study was performed, we were able to obtain OV hologram recordings with vortex sizes as low as $w_{\text{HWHM}} \approx 40$ [μm] with approximately the same values of β.

3.6 Analysis of the Holographic Image

The holographic image was analyzed by monitoring intensity profiles of the propagating image from the surface of the hologram, $z = 0$ to a distance of roughly $z \approx 1.8\,$[m]. The experimental setup is shown on Fig. 3.12. A lens (L) of focal length, $f = 50.8\,$[mm], and a CCD camera (C) were mounted on a translation stage (TS). By moving the translation stage we were able to image the transverse intensity profiles at various propagation distances, z. The imaging system was designed to provide a magnification of 1.7; hence the distance between the lens and the array was fixed

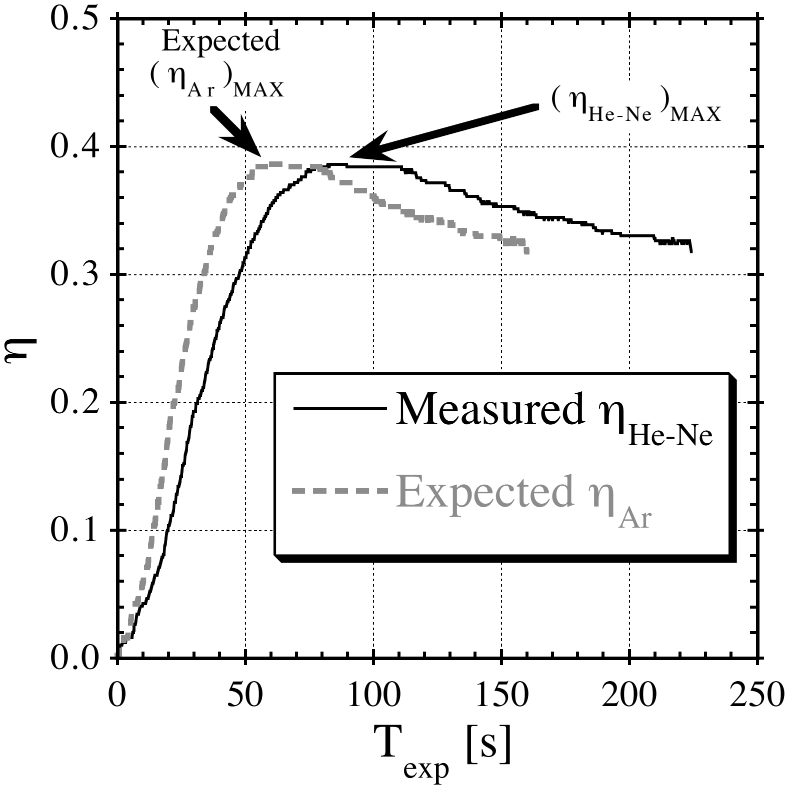

Fig. 3.11: A typical plot obtained from monitoring the He-Ne beam efficiency during the holographic recording process. Given the experimentally measured value of the maximal He-Ne efficiency $(\eta_{\mathrm{He-Ne}})_{\mathrm{MAX}}$, one may calculate the expected maximum efficiency for the Ar laser frequency, $(\eta_{\mathrm{Ar}})_{\mathrm{MAX}}$. From Eq. (3.12), $(\eta_{\mathrm{Ar}})_{\mathrm{MAX}}$ will occur at $0.94(\eta_{\mathrm{He-Ne}})_{\mathrm{MAX}}$. In practice, however, longer exposures would result in higher efficiency.

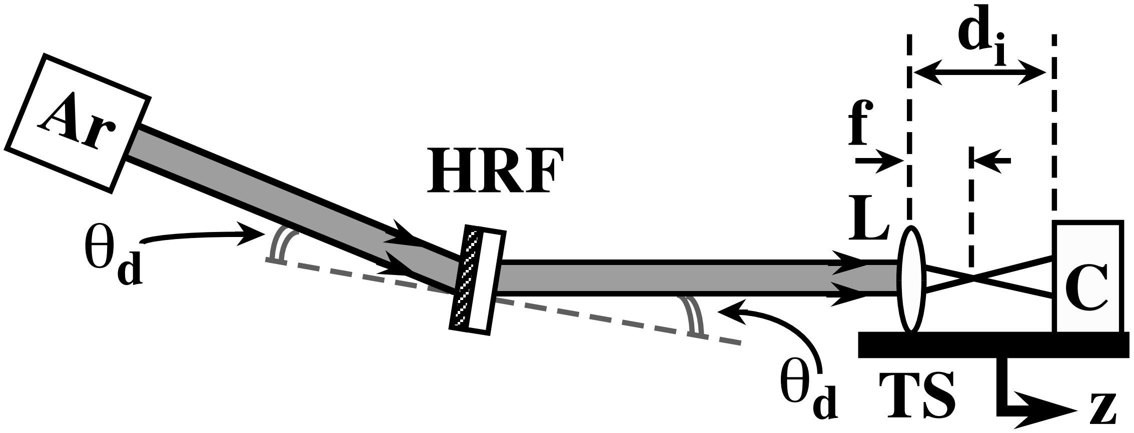

Fig. 3.12: Schematic of the optical system used to examine the vortex recorded onto a photopolymer film (HRF). Vortex beam is imaged to a CCD array (C) by means of a lens (L) with focal length $f = 50.8\,[\text{mm}]$ and imaging distance $d_i = 137\,[\text{mm}]$. Both C and L are mounted on a translation stage (TS), which can move along the optical axis, allowing us to monitor the transverse intensity profile at different propagation distances, z. The camera C is connected to a Macintosh IIfx computer with a frame grabber (not shown).

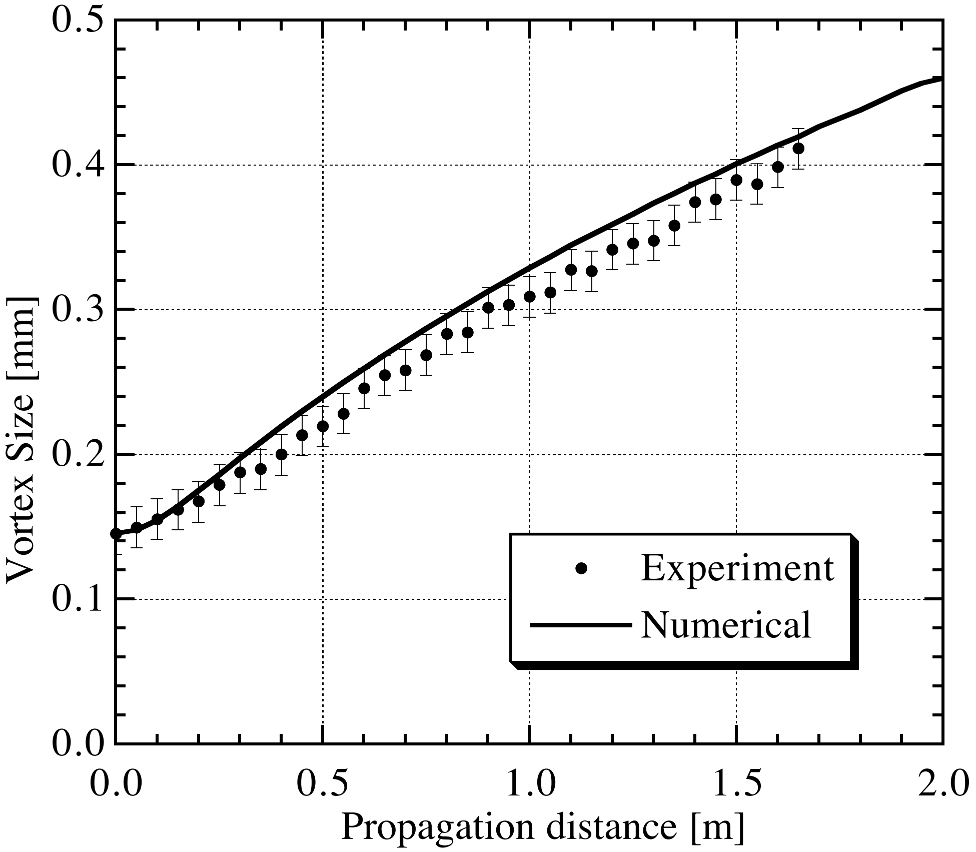

Fig. 3.13: HWHM size of a vortex plotted vs. the propagation distance, z. The discrete points are experimental results. The curve was obtained from numerical simulations, assuming a large Gaussian background beam ($w_0 = 12.8\,\mathrm{mm} \gg w_\mathrm{V}$) with a vortex of the amplitude function profile $A(r) = \tanh(r/w_\mathrm{V})$, with initial $w_\mathrm{V} = 165\,[\mu\mathrm{m}]$ (i.e., $w_\mathrm{HWHM} = 145\,[\mu\mathrm{m}]$).

at $d_i = 137\,[\text{mm}]$. The vortex core size and propagation characteristics were determined by analyzing 34 images, taken at 50 [mm] intervals along the optical axis of the holographic image. The radial intensity distribution function, $|A(r,z)|^2$ was determined by numerically averaging the intensity profile, $I(x,y)$, around the azimuth of the vortex core using the following procedure.

First we determined the location of the vortex center, $(x_c^{(i)}, y_c^{(i)})$, which is expected to coincide with the first moment of the intensity profile,

$$(x_c^{(i)}, y_c^{(i)}) = \frac{\iint\limits_S (x,y) I(x,y,z^{(i)})\,\mathrm{d}x\,\mathrm{d}y}{\iint\limits_S I(x,y,z^{(i)})\,\mathrm{d}x\,\mathrm{d}y}, \tag{3.13}$$

where S is the area of the CCD image, and $z^{(i)}$ is the location of the object plane of the imaging system, and the integrals are performed numerically over a discrete number of grid points. Next we determined the average radial vortex core function by numerically calculating the expression $|A(\tilde{r}, z^{(i)})|^2 = N^{-1}\sum_{j=1}^{N} I(\tilde{r}, j\Delta\theta, z^{(i)})$, where $\Delta\theta = 2\pi/N$ is the discrete angular step size between two grid points lying on a circle of radius $\tilde{r}$ (measured in units of grid points) from the core center, and $N = \mathrm{int}\{2\pi\tilde{r}\}$ is the length of the circle in units of grid points. Finally, we obtained the half width at half maximum values of the core size, w_{HWHM}, and compared it with the half-widths from beam propagation simulations. The results shown in Fig. 3.13 are in excellent agreement over the entire scan range.

3.7 Phase-mask Formation of Optical Vortices

An alternative technique of creating OV's uses a phase mask, or Diffractive Optical Element (DOE), to impose the characteristic helical phase ramp onto a passing laser beam. The mask usually consists of surface relief transparent material having an index of refraction n_1 higher than the index of the surrounding medium n_0. The phase resolution of the mask is limited by the number of different thickness levels, which is determined from available technology and cost considerations. The minimum number of levels required to introduce the helical vortex phase profile appears to be equal to 3, since it is impossible to record the direction of the phase flow around the center with a 2-level mask. Indeed, a 3-level mask was successfully used in the first experimental observation of the optical vortex soliton.[7]

In recent years, diffractive optical element (DOE) technology has significantly advanced[169–171] to achieve sub-micrometer transverse and sub-nanometer depth accuracy. An important factor in this improvement has been the use of high-resolution electron beam lithography,[172,173] isobathic staircase processing and dry etch micromachining techniques. These tools were originally developed for semiconductor applications and were adapted for optical devices. Advantages of using phase masks to generate optical vortices include high efficiency and high damage thresholds. For academic research purposes, the main disadvantage of the high-resolution DOE-technology is its prohibitively high manufacturing cost, owing to the use of extremely expensive lithography and etching equipment for low-volume production.

In 1995 our research group received a competitive grant to participate in Honeywell/ARPA cooperative foundry[§]. The foundry participants had an opportunity

---

[§] Principal Investigator - Grover A. Swartzlander, Jr.

to design a number of phase masks which were then manufactured by Honeywell, Inc. First, we will analytically describe the phase mask profiles. Let us consider an N-level phase mask. This mask approximates a continuous phase helical phase ramp

$$\Phi_V(\theta) = \theta \tag{3.14}$$

by a N-level function

$$\Phi_V^{(N)}(\theta) = \frac{2\pi}{N} \mathrm{floor}\left(\frac{\theta N}{2\pi}\right), \tag{3.15}$$

where θ is the cylindrical angle coordinate in the transverse plane and floor(x) is the function equal to the largest integer value less than or equal to x. From Eq. (3.14) and Eq. (3.15) we plotted the phase profiles for an ideal phase mask and an $N = 8$-level phase mask, shown in Figs. 3.14 and 3.15, respectively.

To create a vortex mask we construct the following DOE from a transparent substrate, which has an index of refraction equal to n_1, while the surrounding air has an index of refraction n_0. We require the thickness of the mask to be the following function of transverse cylindrical coordinates (r, θ)

$$D(r, \theta) = D_0 + \Phi_V^{(N)}(\theta) \frac{\lambda}{2\pi(n_1 - n_0)}, \tag{3.16}$$

where D_0 is a constant (minimum substrate thickness) and $\Phi_V^{(N)}(\theta)$ is given by Eq. (3.15). A coherent wave of wavelength λ traveling perpendicular to the (r, θ) plane will acquire the desired transverse phase profile

$$\Phi(r, \theta) = \frac{D(r, \theta)(n_1 - n_0)}{\lambda} 2\pi \equiv \Phi_0 + \Phi_V^{(N)}(\theta), \tag{3.17}$$

where $\Phi_0 = 2\pi D_0(n_1 - n_0)/\lambda$ is a constant phase shift, which will be ignored below.

We will now describe the specific DOE's designed by our research group and manufactured in Honeywell/ARPA CO-OP workshop.[174] Four 0.5 [cm] × 0.5 [cm]

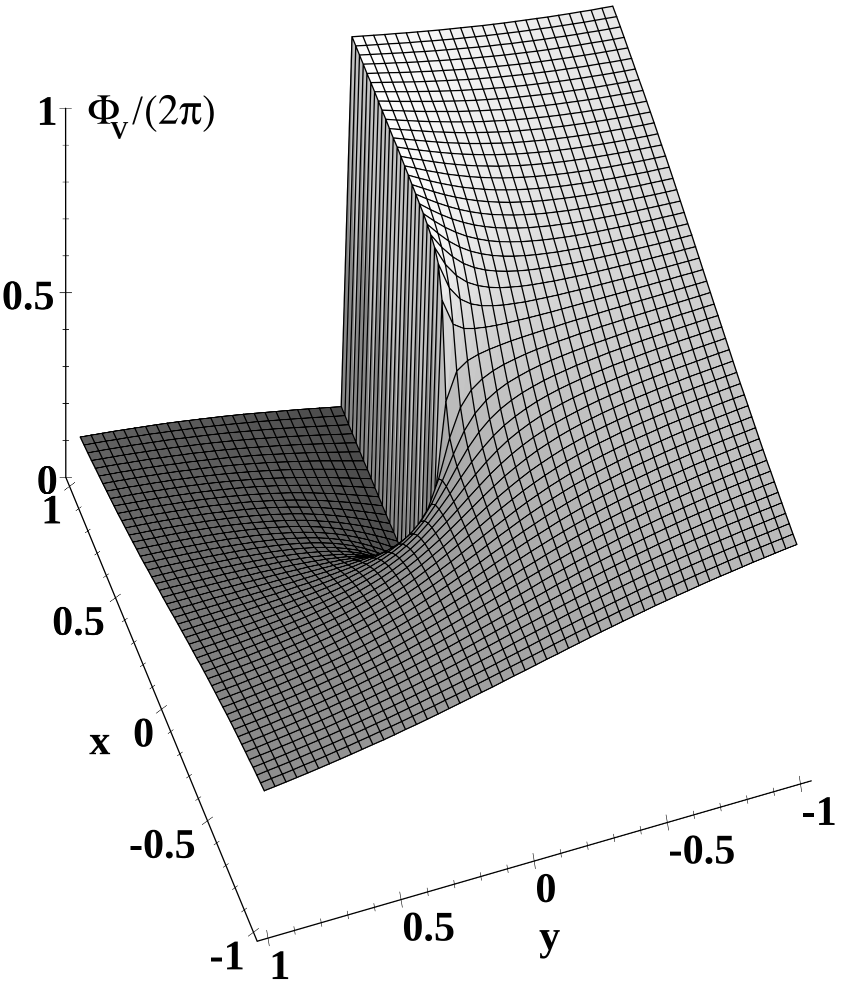

Fig. 3.14: A 3-D rendering of an ideal phase profile of a vortex, given by Eq. (3.14). The phase is plotted in units of 2π.

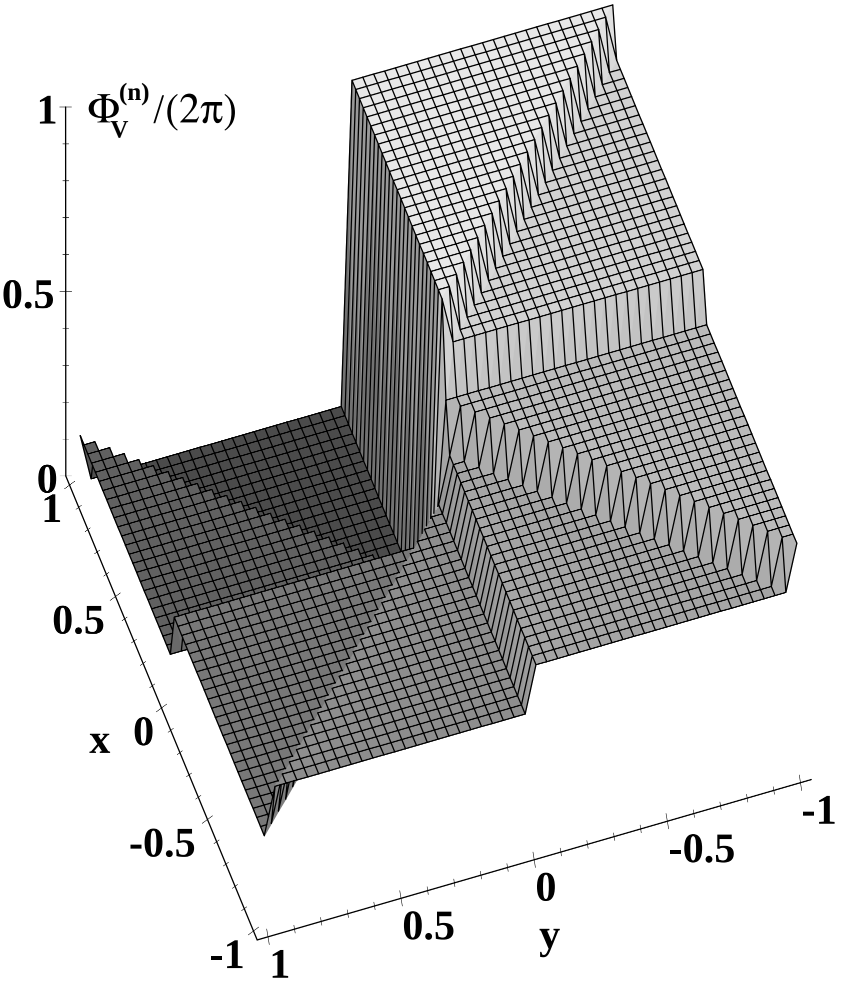

Fig. 3.15: A 3-D rendering of the 8-level representation of the vortex phase profile, given by Eq. (3.15). The phase is plotted in units of 2π.

DOE's were etched on a 1 [cm] × 1 [cm] fused quartz ($\mathrm{Si0_2}$) substrate with the index of refraction, $n_1 = 1.4525$, and the minimum thickness of $D_0 \approx 500$ [μm]. A binary method was used,[175] i.e., k micromachining sequences were applied to achieve $N = 2^n$ depth levels. Each sequence consisted of contact lithography and reactive ion etching. In this particular case, $k = 3$ micromachining sequences were used to create a DOE with operating wavelength $\lambda = 850$ [nm] and $N = 2^3 = 8$ phase levels. The three etch depths, corresponding to phase shifts of π, $\pi/2$ and $\pi/4$ were equal to $\lambda/2(n_1 - n_0) = 939.2$ [nm], $\lambda/4(n_1 - n_0) = 469.6$ [nm] and $\lambda/8(n_1 - n_0) = 234.8$ [nm], respectively. The binary etching mask designs which specified etch areas for each micromachining sequence were recorded in GDS-II stream format (a standard layout data format used in VLSI manufacturing). The transverse alignment error for the three etching masks was measured to be less than 0.28 [μm] from mask to mask.[174] According to the project specifications smallest transverse feature size allowed in the DOE design was equal to 1.5 [μm], which was conservative with respect to the actual sub-micron resolution of the technology used. The average etch depth error for π, $\pi/2$ and $\pi/4$ etches was measured to be 0.82%, 1.23% and 0.76%, respectively.

The etching mask patterns for etching depths corresponding to phase shifts of π, $\pi/2$ and $\pi/4$ and the resulting phase mask are shown in Figs. 3.16 for the DOE's representing the following vortex fields: a single vortex of charge $m = 1$ (Fig. 3.16), a pair of unit charge vortices (Fig. 3.17), ($m_1 = m_2 = 1$) separated by distance $d_\mathrm{V} = 50$ [μm], a pair of unit charge vortices ($m_1 = m_2 = 1$), separated by distance $d_\mathrm{V} = 100$[μm] (Fig. 3.18), and a pair of oppositely charged vortices ($m_1 = 1$, $m_2 = -1$) separated by $d_\mathrm{V} = 100$ [μm] (Fig. 3.19).

Let us now examine the effects of 8-level phase resolution on the spatial quality

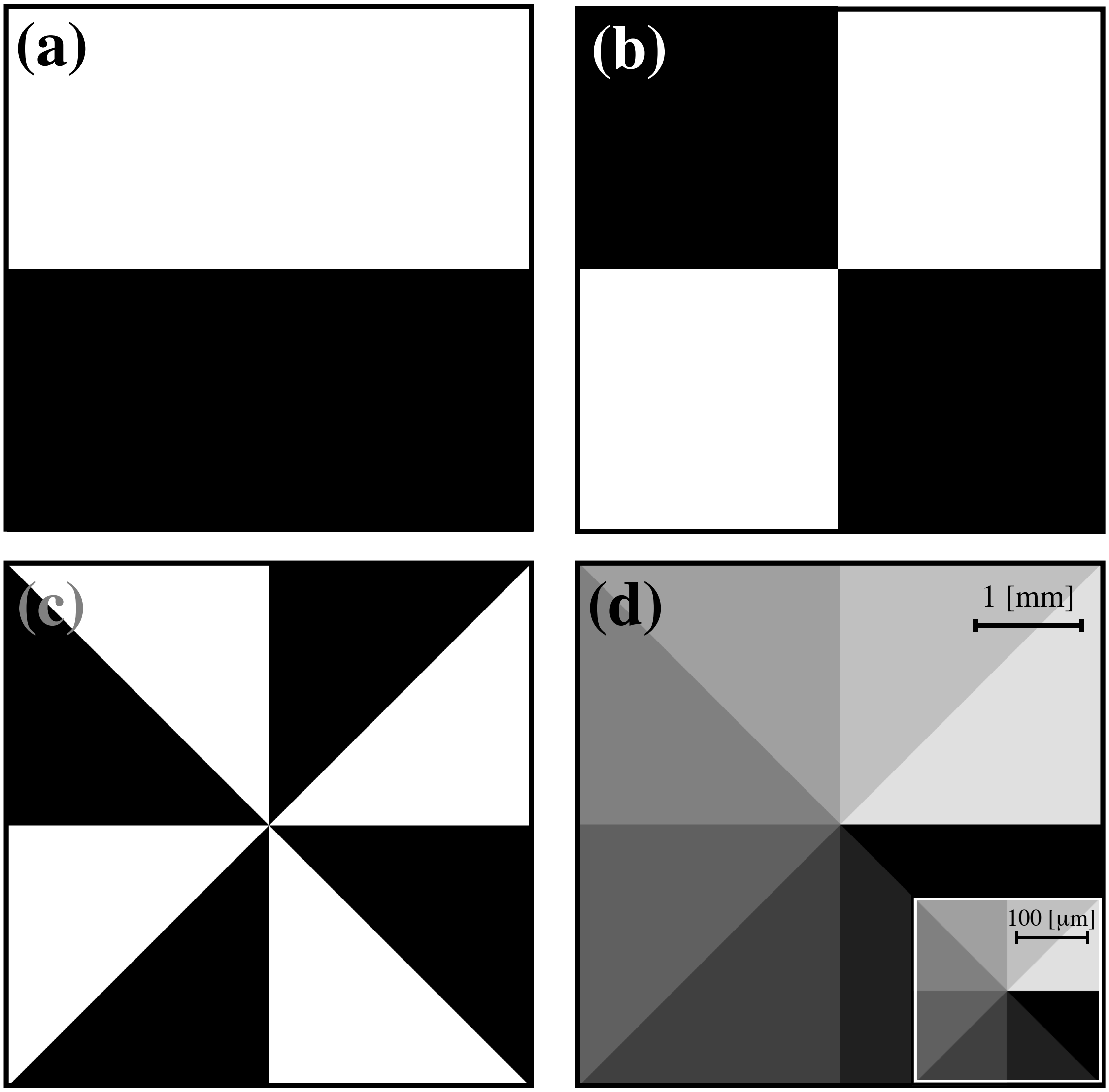

Fig. 3.16: DOE with a single unit charge vortex. We show etch mask patterns corresponding to (a) π, (b) $\pi/2$, (c) $\pi/4$ phase shifts and (d) the resulting phase mask. Inset shows the center of the mask for more detail.

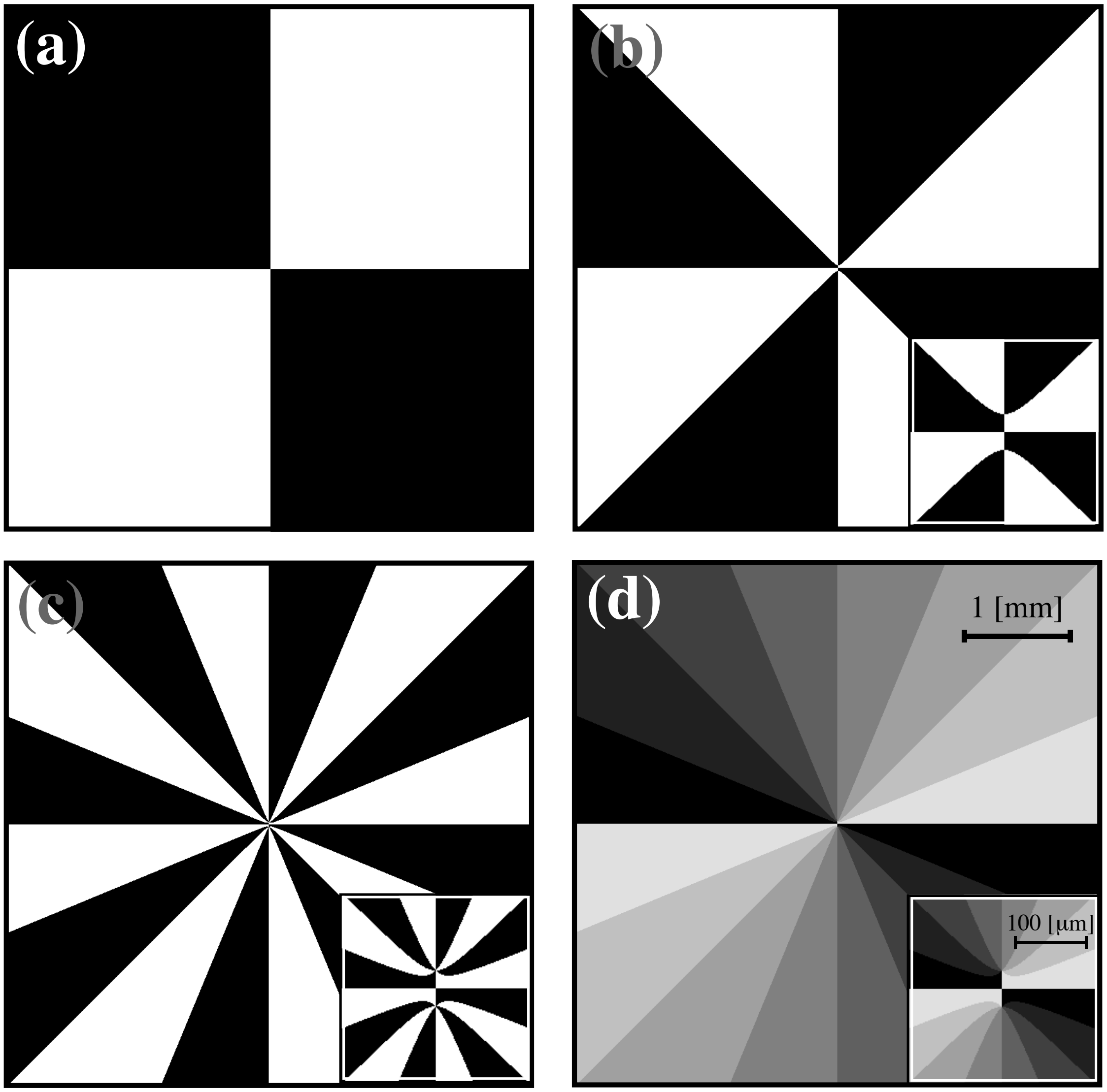

Fig. 3.17: DOE with two vortices of unit charge, separated by $d_V = 50\,[\mu\text{m}]$. We show etch mask patterns corresponding to (a) π, (b) $\pi/2$, (c) $\pi/4$ phase shifts and (d) the resulting phase mask. Insets show the center of the mask for more detail.

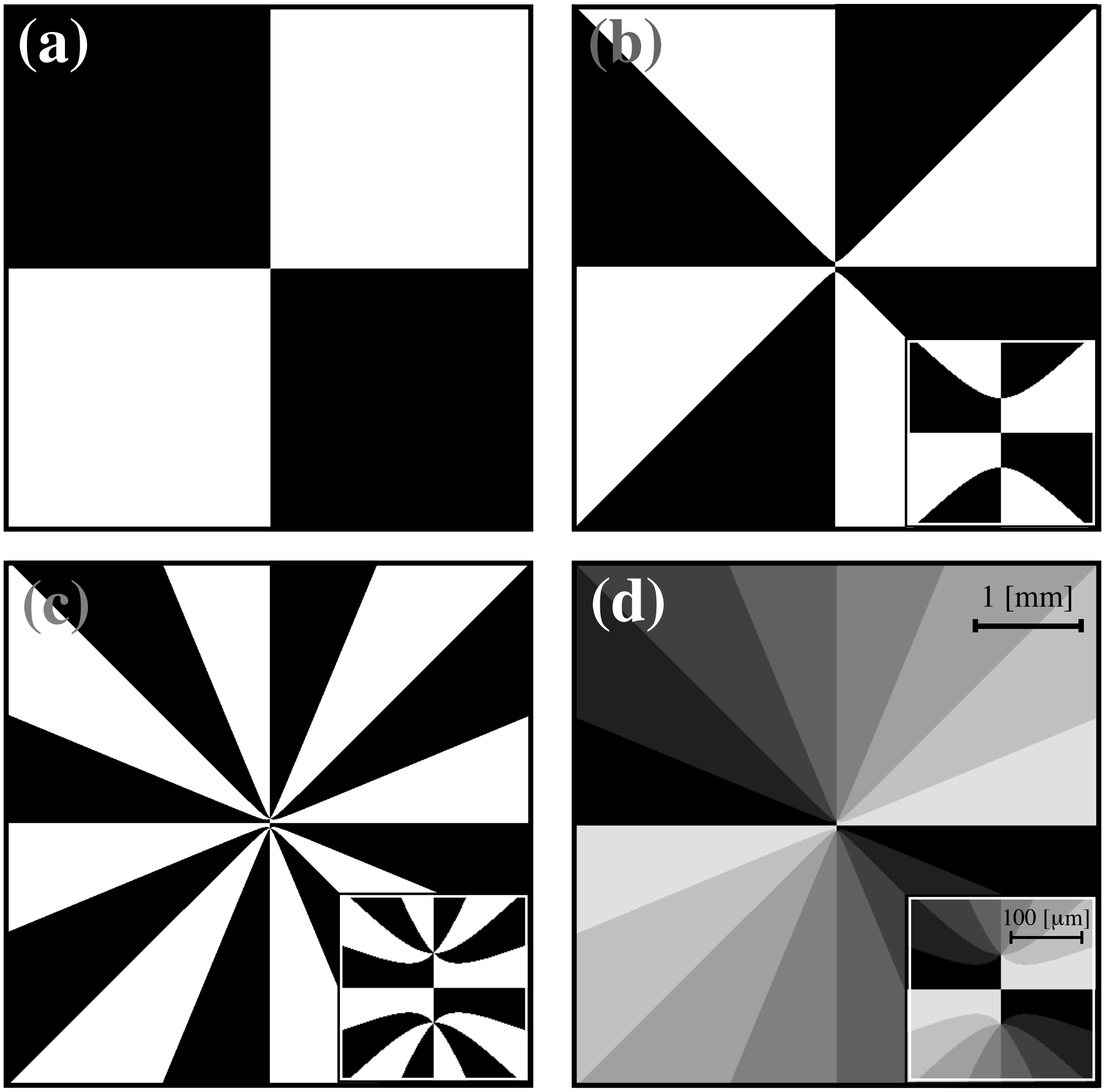

Fig. 3.18: DOE with two vortices of unit charge, separated by $d_{\mathrm{V}} = 100\,[\mu\mathrm{m}]$. We show etch mask patterns corresponding to (a) π, (b) $\pi/2$, (c) $\pi/4$ phase shifts and (d) the resulting phase mask. Insets show the center of the mask for more detail.

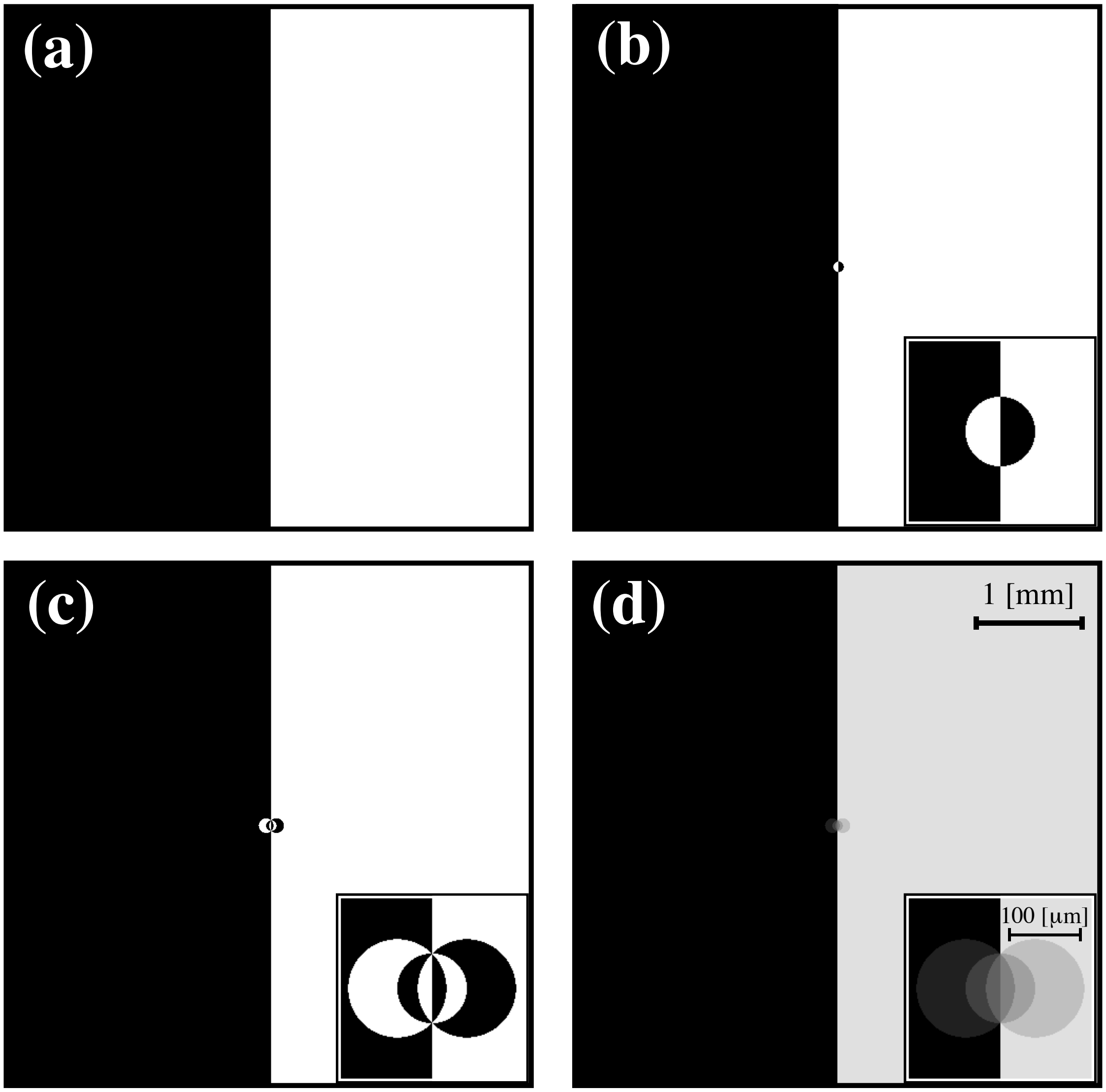

Fig. 3.19: DOE with two vortices of opposite charges, separated by $d_\mathrm{V} = 100$ [μm]. We show etch mask patterns corresponding to (a) π, (b) $\pi/2$, (c) $\pi/4$ phase shifts and (d) the resulting phase mask. Insets show the center of the mask for more detail.

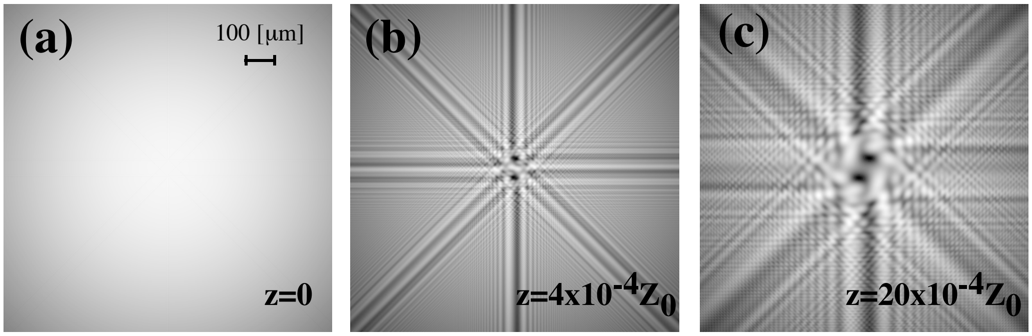

Fig. 3.20: Numerical simulations of near-field propagation of a beam with two vortices of unit charge, separated by $d_{\mathrm{V}} = 50\,[\mu\mathrm{m}]$, created by the DOE shown in Fig. 3.17. A Gaussian beam of radial size, $w_0 = 800[\mu\mathrm{m}]$, and wavelength, $\lambda = 850[\mu\mathrm{m}]$, was used. The propagation distances are normalized to Rayleigh length, $Z_0 = 2.5$ [m]. The transverse intensity profiles are rendered using logarithmic gray-scale.

of the vortex beam. In Fig. 3.20 we show numerical predictions for a propagating beam amplitude profile, corresponding to DOE shown in Fig. 3.17. The initial field is comprised of a pair of unit charge vortices, separated by $d_{\mathrm{V}} = 50\,[\mu\mathrm{m}]$. One can clearly see the radial protuberances brought about by the finite phase resolution of the DOE. As the beam propagates, the artifacts with high spatial frequencies radiate towards the periphery of the beam, while the beam profile at the center smoothes out, owing to diffraction. In practice, spatial filtering may be used to alleviate the artifacts caused by limited phase resolution, with the inherent drawback of increasing the size of the vortex cores.

The specific DOE's described in this chapter are currently being used for proof-of-principle experiments which intend to use vortex phase masks for optical limiting applications.

3.8 Conclusions

In this Chapter we have described a method of creation of optical vortices using computer-generated holography which has the advantages of low cost (unlike phase masks) and the ability to produce arbitrary distributions of OV's (unlike mode converters). We discussed how point-like vortices may be readily made using CGH's, and argued that core sizes on the order of the Nyquist limit of half the holographic grating period may be achieved. Owing to the finite gray scale and spatial resolution of the recording medium (or system), the reconstructed holographic field will be distorted, especially for small values of the grating period (as measured in the number of resolvable printed "dots"). Hence, a trade-off exists between the core size and the image fidelity. Spatial filtering allows one to remove unwanted diffraction orders (attributed to black-and-white holograms), as well as smooth out phase steps (attributed to the limited phase resolution); however, filtering also broadens the core. To achieve core sizes much smaller than the characteristic beam size, i.e., point-like vortices, one must design a system where the beam used to reconstruct the holographic image (and hence, the format size of the holographic film), has a diameter much larger than the grating period of the hologram. This is not difficult to achieve in the laboratory, and thus, one may easily produce point-like optical vortices. We found we were able to achieve a beam to core size ratio of 175. Investigations of single and multiple vortex propagation dynamics may be conducted in both linear and nonlinear optical media. In the former case, low power beams may be used, and hence, CGH's are suitable. The higher powers common to nonlinear optical experiments, however, may require one to re-record the holographic image onto a low-loss material such as a photopolymer. We have described the technique used for achieving high efficiency holograms in

DuPont Holographic Recording Film. Finally, we have measured the vortex core size as the beam propagated in the near-field regime, and found good agreement with the expected values. We also described the creation of vortices using DOE's. The latter method allows sub-micrometer spatial resolutions, however, it is not practical due to high manufacturing costs.

4. PROPAGATION DYNAMICS OF OPTICAL VORTICES

4.1 Introduction

An OV can be characterized by its phase profile and the form of the amplitude core function (Eq. (2.1)). The latter may dramatically affect the propagation dynamics of a vortex. Vortices with strongly localized cores may exhibit propagation behavior which is distinctly different from that of the vortices occuring as cavity modes. For cavity-type modes the amplitude of the electric field in the vicinity of the core varies linearly with the radial distance from the center of the vortex, and thus, we shall call it an "r-vortex" or "large-core vortex". In the case of OVS's or other localized cores, the amplitude may be modeled as $\tanh(r/w_{\mathrm{V}})$, and we shall call this a "vortex filament" or a "small-core vortex". As the size of the small-core vortex vanishes, ($w_{\mathrm{V}} \to 0$), the vortex is said to become a "point-vortex".

This chapter is intended to develop an intuitive understanding of optical vortex motion and to describe the propagation characteristics of different types of vortices in linear and nonlinear media. For example, in a linear material a single off-axis vortex of any type moves transversely across a Gaussian beam in a straight line as the beam propagates. It does not rotate as sometimes described, though its angular displacement tends toward $\pm\pi/2$ as $z \to \infty$. We also give detailed accounts of the orbital motion of identical quasi-point vortices in linear and nonlinear media, and demonstrate how the rotation can slow and reverse its direction. In Sec. 4.2 we review the definitions and properties of OV's. Analytical descriptions of the propagation dynamics are presented in Sec. 4.4, followed by numerical and revised theoretical analyses for special cases in Sec. 4.5, and conclusions in Sec. 4.6.

4.2 Description of Optical Vortices

In general, the linear vector wave equation admits cylindrical wave solutions which are characterized by a separable phase term, $\exp(im\theta)$, where θ is the azimuthal coordinate in the transverse plane, and m is a signed integer called the topological charge. We shall refer to this phase term as "the vortex term", owing to the special properties it exhibits in an optical system, such as particle-like propagation (even in linear media), conservation of topological charge, and conservation of angular momentum. We shall make the paraxial wave approximation, with the waves propagating in the $+z$ direction and oscillating as $\exp[i(\omega t - kz)]$, where ω is the frequency, $k = 2\pi n/\lambda$ is the wavenumber, λ is the vacuum wavelength and n is the index of refraction. To simplify the description of the propagation dynamics owing to diffraction, the scalar wave equation is used. It is valid for beams with the wavevector subtending a small angle with the optical axis and it accurately describes field features which are greater than λ. The propagation of vortices through nonlinear refractive media may also be described by a scalar equation, assuming that either the material exhibits no nonlinear polarizability, or that the light is circularly polarized.[129, 130] Using cylindrical coordinates, the field of a single vortex may be expressed with the ansatz,

$$\begin{aligned} E(r,\theta,z) &= E_0 G_{BG}(r,z)\exp[i\Phi(r,z)] \times A(r,z)\exp[im\theta]\exp[-ikz] \\ &= E_0 u(r,\theta,z)\exp[-ikz] \end{aligned} \tag{4.1}$$

where E_0 is a characteristic amplitude, $\Phi(\theta,r,z)$ describes the part of the phase that changes as the beam propagates, $A(r,z)$ describes the amplitude profile of the vortex core, G_{BG} describes the amplitude of the background field in which the vortex exists, and u is a normalized slowly varying complex function. The vortex described in Eq. (4.1) has an axis parallel to optical axis; a more unusual case is described in Section 6.3. The factor $\exp[i\omega t]$ was omitted, as we are considering the time-averaged field. We will refer to the "dynamics of beam propagation" to describe the changes which occur as the beam propagates through space, not time. Unless stated otherwise, we shall assume the background field has a Gaussian profile: $G_{BG}(r,z) = \exp(-r^2/w^2(z))$ where $w(z)$ characterizes the beam size.

In this chapter we will compare and contrast two characteristically different vortex core functions: a "vortex filament" (used for example to describe OVS's),

$$A(r,z=0) = \tanh\left(r/w_{\mathrm{V}}\right) \tag{4.2}$$

and an "r-vortex" or a "large-core vortex" (found, for example, in a doughnut mode of a laser)

$$A(r,z=0) = (r/w_{\mathrm{r}})^{|m|}. \tag{4.3}$$

where the vortex core size is characterized by w_{V} in Eq. (4.2), but not by w_{r} in Eq. (4.3). In the latter case, the measurable core size is not an independent parameter, but rather is characterized by the background beam; for a Gaussian background, the

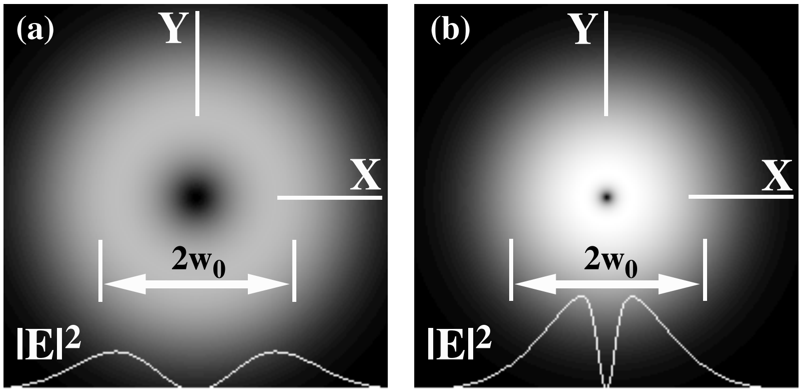

Fig. 4.1: Intensity profiles of an (a) r-vortex and (b) vortex filament on a Gaussian background beam of size w_0, showing the respective large and small vortex cores sizes. The images are shown using a logarithmic gray-scale pallet, whereas a linear scale is used for the line plots (this applies to the other figures in this chapter, unless noted).

half-width at half intensity maximum of the core is $w_{\mathrm{HWHM}} \approx 0.34 w_0$ for $|m| = 1$. The parameter w_{r} is an arbitrary length which, together with E_0 simply scales the peak intensity of the beam. The model function in Eq. (4.2) arises in various physical systems (such as nonlinear refractive media[7,8,127] and Bose-Einstein quantum fluids[176]). The intensity profiles for the fields, Eqs. (4.2) and (4.3), contain a noticeable dark vortex core whose intensity is zero at the center, as shown for an r-vortex and a vortex filament in Fig. 4.1.

First let us review the equations describing vortex (or "doughnut") modes that may emerge from a cylindrically symmetric laser cavity. These modes belong to a family of solutions described by Eq. (4.1), where $A(r, z)$ are Laguerre polynomials.[19] We are presently interested in only those solutions exhibiting at most one intensity minimum within the beam. In that case the solution at the beam waist ($z = 0$)

is given by Eq. (4.3), where $w_{\mathrm{r}} = w_0/\sqrt{2}$. It is well known that the propagation of a doughnut mode is similar to that of an $m = 0$ beam[177] (the TEM_{00} mode*). The amplitude is a self-similar function described by $A(r) = (r/w(z))^{|m|}$ and $G_{BG} = (w_0/w(z))\exp(-r^2/w^2(z))$, where $w(z) = w_0(1+(z/Z_0)^2)^{1/2}$ and $Z_0 = \pi w_0^2/\lambda$ are the beam size and characteristic diffraction length, respectively. In this case, the changing phase term in Eq. (4.1) is given by $\Phi(r,z) = (m+1)\Phi_G(z) + kr^2/2R(z)$ where

$$\Phi_G(z) = \arctan(z/Z_0) \tag{4.4}$$

is the "dynamic Gouy shift", and $R(z) = z[1+(Z_0/z)^2]$ is the radius of curvature of the wavefront. The Gouy shift[60, 61] accounts for the 180° inversion of a beam as it propagates from $z = -\infty$ to $z = +\infty$ with a focal region (the waist) at $z = 0$ (or a 90° rotation from $z = 0$ to $z = \infty$).

Next we describe the field of our model vortex filament, whose vortex core function is given by Eq. (4.2). In practice a beam with this core function may be formed using computer-generated holograms[16, 48] or a diffractive optical element having an etched surface resembling a spiral staircase.[58, 59] Fig. 4.1 shows the intensity profiles of two beams having the same size background beam and power for (a) an r-vortex, and (b) a vortex filament. The vortex filament core size may be arbitrarily small, and hence, the peak intensity may be as much as e = 2.71 times greater than that of an r-vortex beam, provided the total power and Gaussian beam size are the same.

The propagating field of a point vortex ($w_{\mathrm{V}} = 0$) may be determined analytically

---

[*] TEM_{00} mode is a Gaussian beam

by integrating the paraxial Fresnel integral.[178] We find[179]

$$G_{BG}(r,z)A_m(r,z) = \frac{\sqrt{\pi}\,r}{2w_0}\left(\frac{Z_0}{z}\right)^{1/2}\left(\frac{Z_0}{R(z)}\right)^{3/2}\left[I_{\nu^{(-)}}(\gamma) - I_{\nu^{(+)}}(\gamma)\right]\exp\left[-\frac{r^2}{2w^2(z)}\right] \tag{4.5}$$

$$\Phi(r,z) = \frac{\pi}{2}\left(\frac{3}{2} - m\right) + \frac{Z_0}{z}\left(\frac{r}{w_0}\right)^2\left[1 - \frac{1}{2}\left(\frac{w_0}{w(z)}\right)^2\right] - \frac{3}{2}\arctan\left(\frac{z}{Z_0}\right) \tag{4.6}$$

where $I_\nu(\gamma)$ is the modified Bessel function of the first kind of fractional order $\nu^{(\pm)} = (m \pm 1)/2$, $w(z)$ is described above, and the argument $\gamma = (1/2)(r/w(z))^2(1 + iZ_0/z)$. The intensity profile, $|A_m|^2$ is characterized by high spatial frequency ringing in the near field, $z/Z_0 \ll 1$, and smooth profiles for $z/Z_0 > 1$.[179] The intensity profiles are described and depicted in Sec. 4.5.

4.3 Optical Vortex Soliton

An optical vortex soliton (OVS) is a stable (2+1)-dimensional structure which occurs in the defocusing Kerr medium.[7] It comes about when the defocusing effect is balanced by diffraction of the vortex core. Remarkably, an OVS will propagate without any change in its size, assuming an infinite plane wave background. In case of finite-size background beams the soliton size will increase adiabatically owing to beam blooming. Namely, as the intensity of the blooming beam decreases, the nonlinear refractive index change decreases resulting in a larger soliton size.

While investigating a Bose gas Ginzburg and Pitaevskii[2,3] first reported stationary vortex solutions to an equation which was later called the nonlinear Schrödinger (NLS) equation. In the context of diffractive optics, this equation is written

$$-2ik\frac{\partial u}{\partial z} + \nabla_\perp^2 u + 2k^2\frac{n_2 E_0^2}{n_0}|u|^2 u = 0, \tag{4.7}$$

where $\nabla_\perp^2 u = (1/r)(\partial/\partial r(r\partial u/\partial r)) + (1/r^2)(\partial^2 u/\partial\theta^2)$ is the transverse Laplacian in cylindrical coordinates, u is the envelope defined in Eq. (4.1), n_2 is the coefficient of nonlinear refractive index ($n_2 < 0$ for self-defocusing media), and n_0 is the linear index of refraction. The NLS allows a vortex soliton solution

$$u(r,\theta,z) = A(r)\exp(im\theta)\exp(iz/z_{\mathrm{NL}}), \tag{4.8}$$

where $z_{\mathrm{NL}} = 2n_0/(k\Delta n)$ is the nonlinear longitudinal length scale, $m = \pm 1$ is the topological charge, and $\Delta n = -n_2 E_0^2$ is the characteristic nonlinear refractive index change. The amplitude function $A(r)$ may be approximated as

$$A(r) \approx \tanh(r/w_{\mathrm{OVS}}), \tag{4.9}$$

where $w_{\mathrm{OVS}} \approx 1.270 w_{\mathrm{NL}}$ is the soliton size and $w_{\mathrm{NL}} = k^{-1}(n_0/\Delta n)$ is the transverse length scale.[7] Thus, there is an direct relation between the characteristic change of the refractive index and the size of the soliton.

Numerical simulation show how well the tanh approximation describes the OVS. In Fig. 4.2 we see numerical results for initial and propagated radial intensity profiles for a size $w_{\mathrm{V}} = 100$ [μm] soliton (which corresponds to $\Delta n = 1.1 \cdot 10^{-6}$ nonlinear refraction index change). The soliton was propagated a distance equal to $10 Z_{\mathrm{V}}$, where $Z_{\mathrm{V}} = k w_{\mathrm{V}}^2/2$ is the characteristic diffraction length for this soliton size. One can see that the center of the amplitude function retains its initial size, with only negligible ringing far from the center of the soliton. In contrast, considerable radiation ringing will occur if the initial size of the vortex is greater or less than w_{OVS}. In Fig. 4.3 we see large rings emanating from the center of the vortex after propagation, as its core size shrinks to approach the soliton size in the medium.

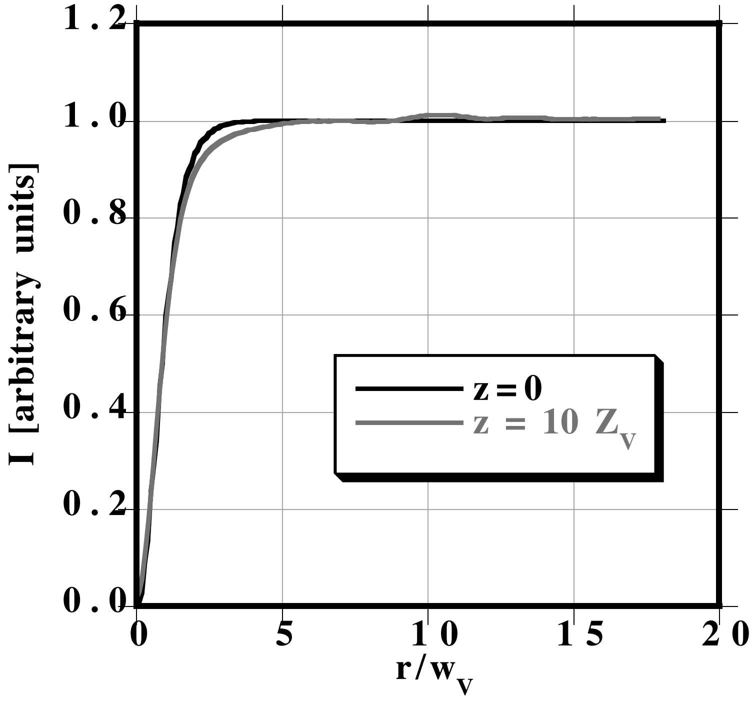

Fig. 4.2: Radial intensity profile of a $\tanh(r/w_{\rm V})$ soliton at $z = 0$ and $z = 10Z_{\rm V}$, where $w_{\rm V} = 100$ [μm] is the soliton size and $Z_{\rm V} = kw_{\rm V}^2/2$ is the characteristic soliton diffraction length. The intensity is plotted in arbitrary units.

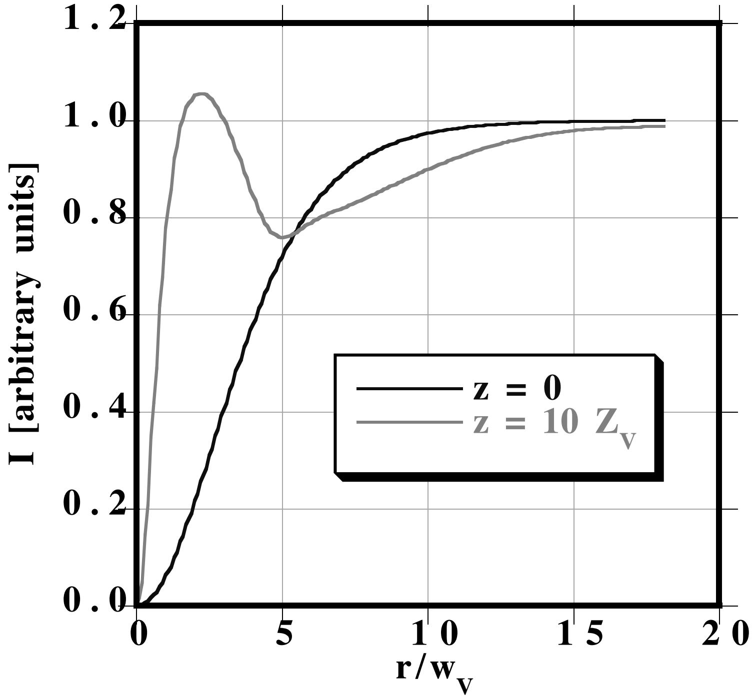

Fig. 4.3: Radial intensity profile of a tanh-vortex which is initially 4 times larger than the $w_{\rm V} = 100\,[\mu{\rm m}]$ soliton size required by nonlinearity ($\Delta n = 1.1 \cdot 10^{-6}$). The plots are shown for $z = 0$ and $z = 10 Z_{\rm V}$, where $Z_{\rm V} = k w_{\rm V}^2/2$ is the characteristic diffraction length for $w_{\rm V} = 100\,[\mu{\rm m}]$. The intensity is plotted in arbitrary units.

4.4 Vortex Propagation Dynamics

We will now describe the propagation of optical vortices using analogies of vortices in a fluid. Hydrodynamic paradigms have been used to describe electromagnetic phenomena throughout history[†]. The NLS equation follows this tradition, as it has been shown to transform into two of the principal equations in fluid mechanics: the Bernoulli and continuity equations.[111,180] These equations may be obtained by writing the complex field envelope $u = f(r,\theta,z)\exp[is(r,\theta,z)]$. Inserting this expression into Eq. (4.7), one obtains two coupled equations:

$$-\frac{\partial s}{\partial z} + \left(\vec{k}_\perp \cdot \vec{k}_\perp\right) = \frac{\nabla_\perp^2 \rho^{1/2}}{\rho^{1/2}} - \frac{P}{\rho}, \tag{4.10}$$

$$\frac{1}{2}\frac{\partial \rho}{\partial z} + \left(\vec{\nabla}_\perp \cdot (\rho \vec{k}_\perp)\right) = 0, \tag{4.11}$$

where $\vec{k}_\perp = -\vec{\nabla}_\perp s$ is the transverse wavevector or ”momentum” of the beam (it is analogous to the velocity field of a fluid), and, $\rho = f^2 = |u|^2$ is the intensity or “density” and $P = 2\rho^2$ is the “pressure” of a fluid, respectively. The term P/ρ in Eq. (4.10) vanishes in linear media ($n_2 = 0$).

From Eq. (4.1), we write $s = m\theta + \Phi(r,z)$ and $f = G_{BG}(r,z)A(r,z)$. It is clear from Eqs. (4.10) and (4.11) that two of the important terms driving the propagation dynamics in both linear and nonlinear media are the phase gradient, $\vec{k}_\perp$ and the intensity gradient, $\vec{\nabla}_\perp \rho$. At all points, except the singularity, we find

$$\vec{k}_\perp = -\vec{\nabla}_\perp s = -\hat{\theta} r^{-1}\partial s/\partial\theta - \hat{r}\partial s/\partial r. \tag{4.12}$$

However, we are most interested in the motion of the singularity, where special attention is required.

[†] See Appendix A for a more detailed description of vortex filament motion in a fluid.

In a fluid, one finds that the velocity field at the center of the vortex is unaffected by the vortex itself; rather, the vortex may be viewed as being attached to a particle that moves with the local flow field. The latter statement holds true for a vortex filament without kinks and torsion, which may cause self-action of a filament.[181] In a similar fashion, we may surmise that the transverse wavevector at the center of an optical vortex is unaffected by the vortex itself, for a vortex whose axis is aligned with z. The trajectory of a given vortex is affected by all other sources of $\vec{k}_\perp$ and $\vec{\nabla}_\perp \rho$, such as diffracting waves or other vortices. The fluid paradigm suggests the following hypothesis for an optical vortex: *In a linear medium, the vortex trajectory is affected by the factors in the field at the singularity which exclude the singularity being examined*, i.e., the field $u/[A(r,z)\exp(im\theta)]$ and its derivatives, evaluated at the vortex core. Thus, at the center of the vortex core the transverse momentum is $\vec{k}_\perp = -\vec{\nabla}_\perp \Phi$ (this may also be viewed as the local average value of $\vec{k}_\perp$ in the vicinity of the core). To develop an understanding of the effects of amplitude and phase gradients on vortex motion, let us consider these two interactions separately.

It may be demonstrated that a vortex moves perpendicular to the gradient of the amplitude of the background field in a linear medium, by considering a singly charged ($m = \pm 1$) r-vortex placed at the origin, and a background field whose amplitude varies linearly in the x-direction:

$$E(r, \theta, z = 0) = E_0 \exp(im\theta) \left\{1 + (r/L)\cos\theta\right\} r/w_{\mathrm{r}} \equiv E_0 u(r, \theta, z = 0), \qquad (4.13)$$

where L and w_{r} characterize the slope of the background field and vortex core, respectively. (Note that $|L^{-1}| = |G_{BG}^{-1} \vec{\nabla}_\perp G_{BG}|_{r=0}$, where $G_{BG} = E_0 \left\{1 + (r/L)\cos\theta\right\}$.) As the beam propagates, the initial direction of motion of the vortex can be easily determined by expressing the field (or intensity) as a Taylor series expansion:

$u(r, \theta, \delta z) = u(r, \theta, 0) + (\partial u/\partial z)\delta z$, where $\partial u/\partial z$ can be found from Eq. (4.7). The coordinates of the vortex must satisfy the condition, $|u| = 0$, whence we find the vortex displacement vector:

$$\vec{r}(\delta z) = \mathrm{Sgn}(m)(\delta z/k^2)\vec{k} \times (G_{BG}^{-1}\vec{\nabla}_\perp G_{BG})_{r=0} \tag{4.14}$$

where $\mathrm{Sgn}(m) = m/|m|$. Thus, the vortex moves not in the direction of the sloping field, but rather perpendicular to it. If the topological charge is positive (negative), the vortex moves in the positive (negative) y-direction. This demonstration suggests that a vortex having an arbitrary core function may experience a displacement whenever the intensity of the background field is nonuniform, although we have not proven it for an arbitrary core function.

Let us now examine the motion of a vortex in the presence of a nonuniform phase. In particular, we will consider the fundamental interaction between two identical vortices, separated by a distance, d_V, shown schematically in Fig. 4.4. To obtain a purely phase-dependent interaction, with no amplitude-dependent effects as previously described, we will assume point-vortices ($w_\mathrm{V} \to 0$) on an infinite, uniform background field ($w_0 \to \infty$). We note that the vortex cores will diffract over some distance of order, $Z_\mathrm{V} = \pi d_\mathrm{V}^2/\lambda$, and thus, the background field experienced by each vortex will appear nonuniform for $|z| \geq Z_\mathrm{V}$. However, over the range $|z| \ll Z_\mathrm{V}$, the background field may be considered uniform and approximated by:

$$E(r, \theta, z) = \exp[i(m_1\theta_1 + m_2\theta_2) - ikz] \tag{4.15}$$

where θ_j is the azimuthal coordinate measured about the j^{th} vortex which has a topological charge, m_j (see Fig. 4.5). We wish to find the angular displacement ϕ_V

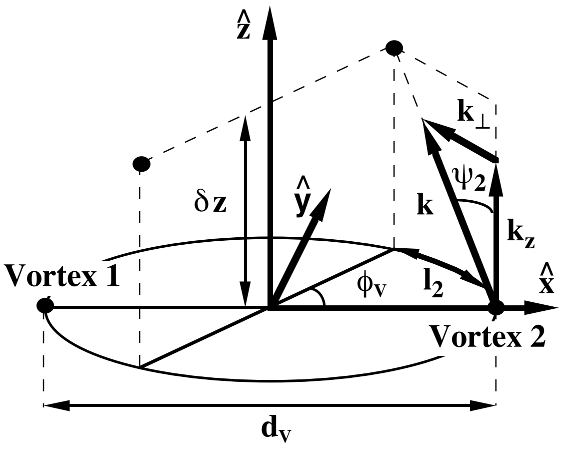

Fig. 4.4: Three-dimensional sketch of the position of the vortex in the transverse x-y plane, propagating in the z-direction with wavevector $\vec{k} \approx k_z \hat{z}$. The wavevector at the center of the vortex 2 has a transverse component, $k_\perp \ll k_z$.

of a propagating vortex from its initial position, $\Theta_j(z = 0)$:

$$\phi_{\mathrm{V}}(z) \equiv \Theta_j(z) - \Theta_j(z = 0) \tag{4.16}$$

For simplicity, let us assume $m_1 = m_2 = -1$. In this case, the transverse wavevector at all non-singular points is determined from Eq. (4.12):

$$\vec{k}_\perp = \hat{\theta}_1/r_1 + \hat{\theta}_2/r_2, \tag{4.17}$$

where $\hat{\theta}_j$ is the unit vector along the azimuth of the j^{th} vortex and r_j is the distance from its center. However, at the center of vortex 1, the effective wavevector is $\vec{k}_\perp(r_1 = 0) = \hat{\theta}_2/d_{\mathrm{V}}$. Likewise, at the center of vortex 2, $\vec{k}_\perp(r_2 = 0) = \hat{\theta}_1/d_{\mathrm{V}}$. The transverse wavevector at the singularities indicates the direction of motion of the vortices in the transverse plane. Combining the transverse and longitudinal motion, one may expect the two vortices to trace a double-helical trajectory, analogous to the orbital motion in time of two vortices in a fluid.[87] This trajectory can be determined with the aid of

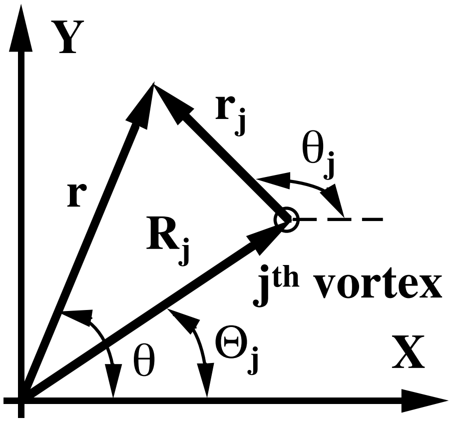

Fig. 4.5: Transverse coordinates of the j^{th} vortex, located at the point (R_j, Θ_j), with respect to the origin (assumed to be at the center of the background beam). The amplitude and phase of the vortex are expressed in terms of the coordinates (r_j, θ_j).

Fig. 4.4. The angle ψ_2 between the transverse wavevector at vortex 2 and the optical axis $\hat{z}$ can be determined from trigonometry:

$$\tan\psi_2 = k_\perp(r_2 = 0)/k = \lambda/(2\pi d_\text{V}), \tag{4.18}$$

where the paraxial wave approximation, $k_\perp \ll k_z \approx k$, has been assumed. While propagating a distance, z, in the $\hat{z}$ direction, vortex 2 moves an arclength, $l_2 = z\tan\psi_2$, in the transverse plane around the point at the center of the pair (the origin), which is is located a distance $d_\text{V}/2$ from each vortex. The angle of rotation is then

$$\phi_\text{V} = 2l_2/d_\text{V} = (2/d_\text{V})z\tan\psi_2. \tag{4.19}$$

We may now find the angular rate of rotation using Eqs. (4.18) and (4.19):

$$\Omega_d \equiv \Delta\phi_\text{V}/\Delta z = \lambda/(\pi d_\text{V}^2) = 1/Z_\text{V}. \tag{4.20}$$

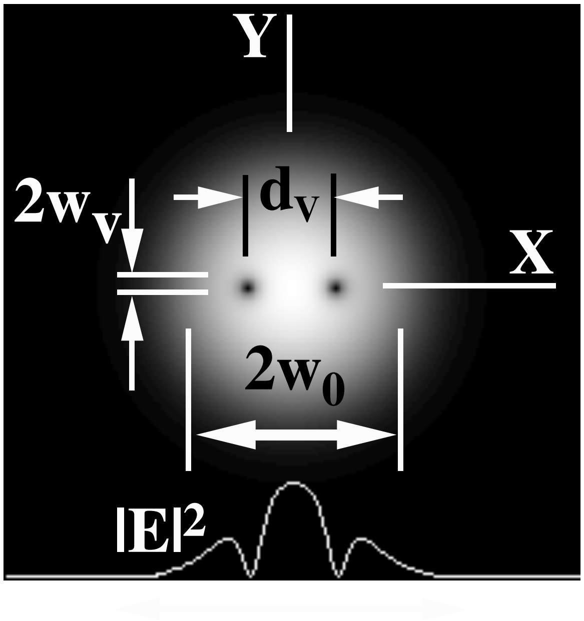

Fig. 4.6: Two vortex filaments of size, w_V, and separation, d_V, are placed symmetrically about the center of a Gaussian background beam of size, w_0.

This result was obtained after assuming vortex charges $m_1 = m_2 = -1$. For a vortex pair with *positive* unit charges, the rotation is reversed, i.e. in the general case of $m_1 = m_2 \equiv m$

$$\Omega_d = -m/Z_\mathrm{V}. \tag{4.21}$$

An equivalent result was obtained by Roux.[84] Our numerical calculations, described below, indicate that Eq. (4.20) is valid until the vortex core functions overlap, which occurs at a distance of roughly $Z_\mathrm{V}/4$. Thereafter, the vortex motion is found to be characteristically different from the initial rotation regime, i.e. the angular velocity decreases owing to the additional effects of amplitude gradients. Corrections to Eq. (4.20) for vortex filaments, rather than point-vortices, are described in Sec. 4.5.

Having these examples of amplitude- and phase-driven vortex motion as conceptual guides, we now explore the more realistic case of vortex motion within a finite size Gaussian beam. In particular, we are interested in the trajectory of a pair of identical singly charged vortices placed symmetrically about the center of the beam in the initial plane $z = 0$. The field describing M vortices embedded in a Gaussian beam may be written

$$E(r, \theta, z = 0) = E_0 \exp\left(-r^2/w_0^2\right) \prod_{j=1}^{M} A_j(r_j, z = 0) \exp(i m_j \theta_j), \tag{4.22}$$

where $A_j(r_j, z = 0)$ is the initial core function of the j^{th} vortex, and (r_j, θ_j) are the polar coordinates measured with respect to the center of the j^{th} vortex (see Fig. 4.5). We shall assume $M = 2$ and $m_1 = m_2 = -1$. The intensity profiles for vortex filament and r-vortex core functions are shown respectively in Figs. 4.6 and Fig. 4.7[‡] In both cases the vortices are separated by a distance, d_{V}, and the initial phase profiles (at $z = 0$), shown in Fig. 4.8, are identical. Note that the phase increases from 0 to 2π in a clockwise sense for both vortices. The unavoidable overlap of the r-vortex cores is clearly evident in Fig. 4.7.

The motion of r-vortices, as shown in Fig. 4.7, in a single beam has been treated by Indebetouw,[57] and we will review his results which, surprisingly, find that r-vortices exhibit no fluid-like motion (unlike point-vortices). In fact, Indebetouw showed that any number of identical r-vortices within a Gaussian beam will propagate independently of the others. For a single pair, as described in Eq. (4.22) with $A_j = r_j/w_{\mathrm{r}}$, the trajectory is given, in cylindrical coordinates measured about the center of the

---

[‡] In this Chapter, a logarithmic gray-scale pallet was used to render all intensity images, unless noted otherwise.

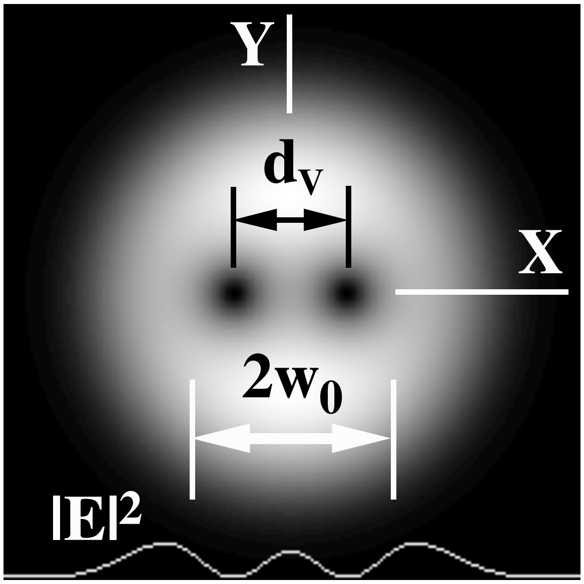

Fig. 4.7: Two r-vortices of separation, d_{V}, are placed symmetrically about the center of a Gaussian background beam of size, w_0.

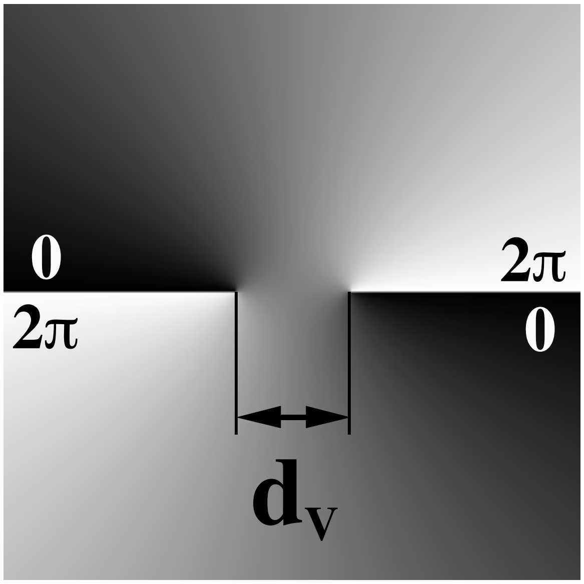

Fig. 4.8: Phase profile of two charge $m = -1$ vortices in the initial transverse plane, $z = 0$, separated by a distance, d_{V}. A linear gray-scale pallet was used in this case, where black (white) corresponds to a phase of 0 (2π).

beam (see Fig. 4.5), by the expressions

$$\begin{aligned} R_j(z) &= R_j(0)\sqrt{1+z^2/Z_0^2}, && (4.23)\\ \Theta_j(z) &= \Theta_j(0) - \mathrm{Sgn}(m)\Phi_G(z), && (4.24) \end{aligned}$$

where $R_j(0)$, $\Theta_j(0)$ are the initial coordinates of the j^{th} vortex. We find that the vortices do not actually rotate, as one may expect from Eq. (4.24); rather the projection of the trajectories onto the transverse plane are straight parallel lines given by parametric equations:

$$y_j(z) = x_j(z)\tan[\Theta_j(0) - \mathrm{Sgn}(m)\Phi_G(z)], \qquad (4.25)$$

where $R_j^2(0) = x_j^2(0) + y_j^2(0)$ is the initial displacement of the j^{th} vortex from the center of the beam. Although the vortices do not circle the optical axis, it is useful to calculate the angular rate of rotation for an r-vortex using Eqs. (4.24) and (4.16):

$$\Omega_{\mathrm{r}} = \Delta\phi_{\mathrm{V}}/\Delta z = -\mathrm{Sgn}(m)Z_0^{-1}(w_0/w(z))^2 = -\mathrm{Sgn}(m)Z_0^{-1}(1+(z/Z_0)^2)^{-1}. \qquad (4.26)$$

For linear media, analytical solutions exist only for r-vortices in a Gaussian beam. To examine the motion of vortex filaments in a Gaussian beam, numerical techniques are helpful. These techniques are also useful to model propagation in nonlinear media. In the next Section we present numerical results which show that *whereas vortex filaments exhibit distance-dependent rotation rates, those with overlapping core functions tend to be independent of the vortex separation distance.*

4.5 Numerical Investigation

Numerical investigations may not only provide considerable insight into the physics of optical vortex propagation dynamics, they may also help identify physically realizable experiments. In this section, we examine four different vortex propagation phenomena that occur within a Gaussian background field.

Case 1 examines the linear propagation of a single r-vortex or vortex filament in the center of a Gaussian beam. *Case 2* explores the vortex-beam interaction that occurs when a vortex is displaced from the optical axis. Vortex-vortex interactions in a linear medium are investigated in *Case 3*, showing distinct differences between the r-vortices and vortex filaments. *Case 4* examines the interaction between OVS's in nonlinear media.

The so-called "Split-Step" or "Beam Propagation" numerical method[182] is used to determine the field of the propagating beam. The data was computed on a DEC-Alpha 3000-800, and a Macintosh II-fx computer was used to process the images. The transverse numerical grid size was 1024x1024 (or 2048x2048 for some cases), with each element corresponding to a size $\Delta x = 4.88\,[\mu\text{m}]$. Unless stated otherwise, a beam size of $w_0 = 488$ [μm], and a wavelength of $\lambda = 800$ [nm] is used. For the vortex filament cases, we assume $w_{\text{OVS}} = 57\,[\mu\text{m}]$, which corresponds to a soliton with induced index change of $\Delta n = 8.0 \times 10^{-6}$. Note that we render gray-scale intensity profiles using a logarithmic palette to depict a visual image, whereas linear scales are used for line plots and phase profiles.

Case 1. The linear propagation of a vortex placed in the center of a Gaussian beam (see Eq. (4.1)) has been described in Sec. 4.2 for an r- and point-vortex. The self-similar intensity profile of a propagating r-vortex is shown in Fig. 4.1(a). The solution for a propagating vortex filament is intractable, unless the core size vanishes (see Eqs. (4.5), (4.6)), whereas numerical solutions provide easily interpreted results. The discussion of Eq. (4.5) suggests that diffractive ringing may occur in the near-field region, even when $w_{\mathrm{V}} \neq 0$. This ringing is depicted in Fig. 4.9 for (a) $w_{\mathrm{V}}/w_0 = 0.12$ and (b) $w_{\mathrm{V}}/w_0 = 0$, showing that intensity ringing is negligible unless $w_{\mathrm{V}}/w_0 \ll 1$. For any ratio, $w_{\mathrm{V}}/w_0 \ll 1$, the rings diffract out of the vortex region for $z > Z_0$, and the optical quality of the beam remains smooth.

Case 2. Let us now displace the vortex from the center of the beam, to a point where the background intensity gradient is non-zero, and examine the position of the propagating vortex. As discussed in Sec. 4.4, the projection of the vortex trajectory in the transverse plane is expected to initially move in the direction of $m\vec{k} \times \vec{\nabla}_\perp G_{BG}$. Let us first consider an r-vortex of charge $m = +1$, placed at the point $(x_0, y_0) = (r_0, 0)$ or equivalently, at $(R(0), \Theta(0)) = (r_0, 0)$, where $r_0 = w_0/2 = 244$ [μm]. The initial field is given by Eqs. (4.3) and (4.22), with $M = 1$, $\theta_1 = \arctan[(y - y_0)/(x - x_0)]$ and $r_1 = ((x - x_0)^2 + (y - y_0)^2)^{1/2}$. As expected from Eq. (4.25), we see in Fig. 4.10 that the vortex indeed moves in a straight line, with the angular position moving clockwise with respect to the center of the Gaussian beam. The vortex positions in the transverse plane after propagating distances $z = 0, Z_0, 2Z_0, 3Z_0$ are depicted with white squares.

We suggested a hypothesis in Sec. 4.4 that vortex motion is unaffected by its own amplitude and phase. Thus, a single vortex filament on a Gaussian beam is expected to also move in a straight line. (The field of an off-axis vortex filament may be written as in the previous example, except with the core function given by Eq. (4.2).) The numerically computed position of the vortex filament, shown in Fig. 4.11, is indeed identical to that of the r-vortex in Fig. 4.10. Only the diffraction of the vortex core distinguishes these two examples (the size and position of the vortex core are depicted with white circles). This result supports the validity of the optical vortex

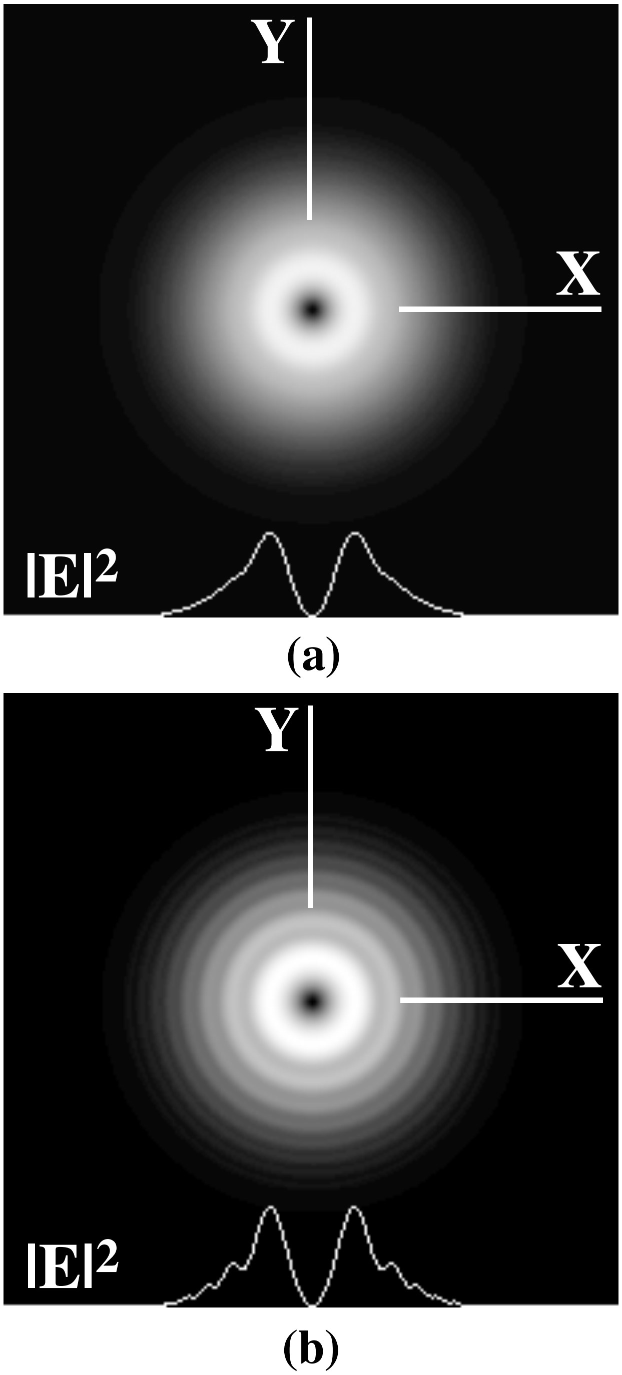

Fig. 4.9: Near-field intensity profiles at a propagation distance, $z/Z_0 = 0.05$ showing negligible ringing when (a) $w_\mathrm{V} = 57\,[\mu\mathrm{m}]$, and significant vortex radiation when (b) $w_\mathrm{V} = 0$. The size of the initial background Gaussian field is $w_0 = 488\,[\mu\mathrm{m}]$.

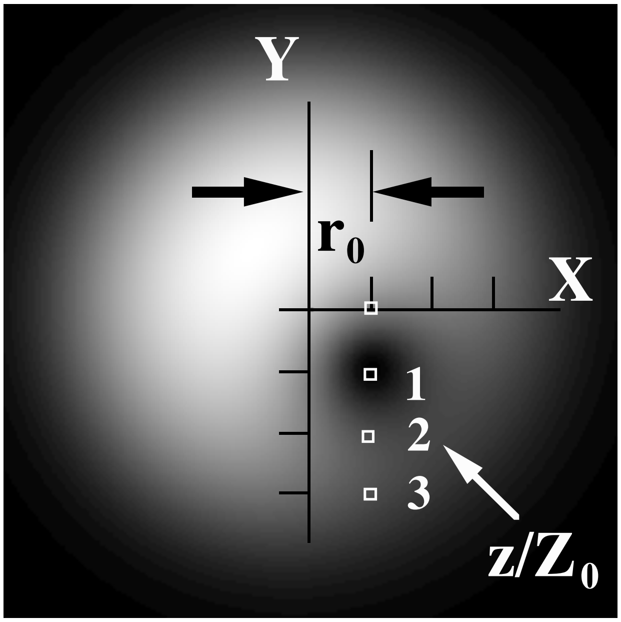

Fig. 4.10: An off-axis r-vortex of charge $m = +1$ in a Gaussian beam ($w_0 = 488$ [μm]) is initially place at the point $(x_0, y_0) = (r_0, 0)$, where $r_0 = 244$ [μm]. The beam is shown at the distance $z = Z_0$. The projection of the vortex trajectory in the transverse plane, shown by the white squares, is a straight line. The vortex advances at a uniform rate, given by r_0/Z_0.

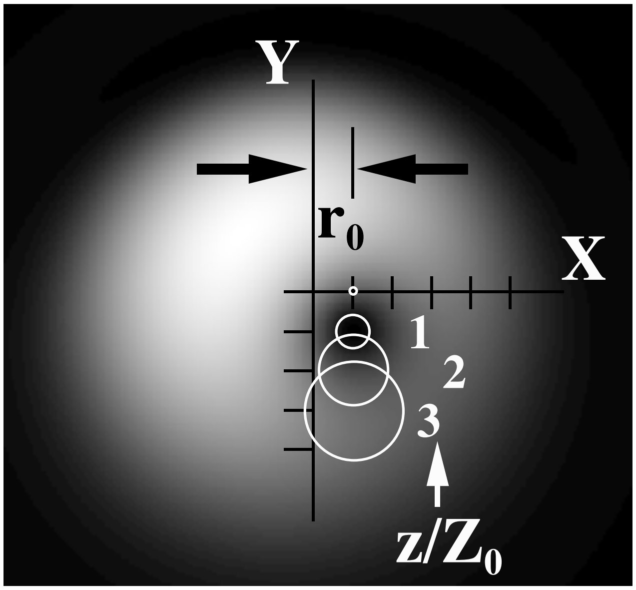

Fig. 4.11: An off-axis vortex filament of charge $m = +1$ in a Gaussian beam ($w_0 = 488\,[\mu\text{m}]$) is initially place at the point $(x_0, y_0) = (r_0, 0)$, where $r_0 = 244\,[\mu\text{m}]$. The beam is shown at the distance $z = Z_0$. The projection of the vortex trajectory in the transverse plane, shown by the white circles (whose radius depicts the size of the advancing vortex), is a straight line. As for an r-vortex, the vortex filament advances at a uniform rate, given by r_0/Z_0.

hypothesis in a linear medium.

Case 3. Let us now introduce a second vortex into the beam so that the trajectory of a vortex is affected by not only the Gaussian background field, but also by the field of the other vortex. We examine the case where the vortices, separated by a distance, d_V, and having topological charge, $m_1 = m_2 = +1$, are placed symmetrically about the center of the beam, as shown in Fig. 4.6 for vortex filaments, and Fig. 4.7 for r-vortices.

The field is described by Eq. (4.22) with $M = 2$, $r_1 = ((x - x_{1,0})^2 + (y -$

$y_{1,0})^2)^{1/2}$, $r_2 = ((x - x_{2,0})^2 + (y - y_{2,0})^2)^{1/2}$, $\theta_1 = \arctan[(y - y_{1,0})/(x - x_{1,0})]$, and $\theta_2 = \arctan[(y - y_{2,0})/(x - x_{2,0})]$, where the initial position of the vortices (at $z = 0$) are given by the coordinates $(x_{1,0}, y_{1,0}) = (r_0, 0)$, and $(x_{2,0}, y_{2,0}) = (-r_0, 0)$ or equivalently, $(R_1(0), \Theta_1(0)) = (r_0, 0)$ and $(R_2(0), \Theta_2(0)) = (r_0, \pi)$. The vortices are initially separated by a distance $d_\mathrm{V} = 2r_0$.

Let us first we examine the trajectories for a pair of r-vortices, which, according to the theory reviewed in Sec. 4.4, are not expected to exhibit vortex-vortex (i.e., d_V-dependent) interactions. The trajectories demarked by white squares on the intensity profile in Fig. 4.12 confirm this fact. The trajectory of the vortex at the right hand side is exactly the same as that observed for the single r-vortex shown in Fig. 4.10. On the other hand, a pair of vortex filaments is expected to exhibit strikingly different propagation dynamics, depending on the separation distance d_V. Indeed, Fig. 4.13(a) shows that a significant rotation, 25°, is achieved over a short distance ($z/Z_0 = 0.1$). In comparison, the Gouy shift (Eq. (4.4)) over this distance is only 5.7°. As the vortex trajectory shows in Fig. 4.13(b), the rotation angles continue to increase over longer propagation distances; however, the radial positions also change, possibly owing to nonlinear beam blooming. The vortices experience an initially rapid orbital motion, followed by a slower nearly-rectilinear motion, driven by the background beam (analogous to motion of r-vortices). This trajectory is consistent with the discussion in Sec. 4.4, where it was argued that the vortex filaments initially propagate like point-vortices in a fluid until the vortex cores begin to overlap. An experimental verification of this phenomenon89, 90 is described in more detail in Section 5.2.

Since vortex propagation is affected not only by other vortices but also by the amplitude and phase gradients of the Gaussian beam, we will now investigate

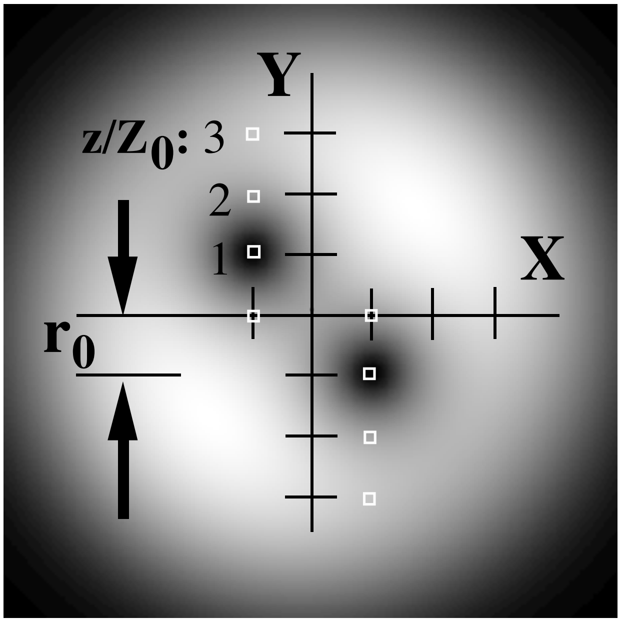

Fig. 4.12: Two r-vortices of topological charge, $m = +1$, and separation, $d_{\mathrm{V}} = 2r_0 = w_0 = 488$ [μm], are initially placed at the points $(\pm r_0, 0)$. The beam, shown at the distance $z = Z_0$, shows the vortex trajectories (see Eq. (4.25)), as described by the dynamic Gouy phase. The white squares mark the positions of the vortices at propagation distances $z = 0, Z_0, 2Z_0, 3Z_0$. The trajectories are straight lines, as in Fig. 4.10.

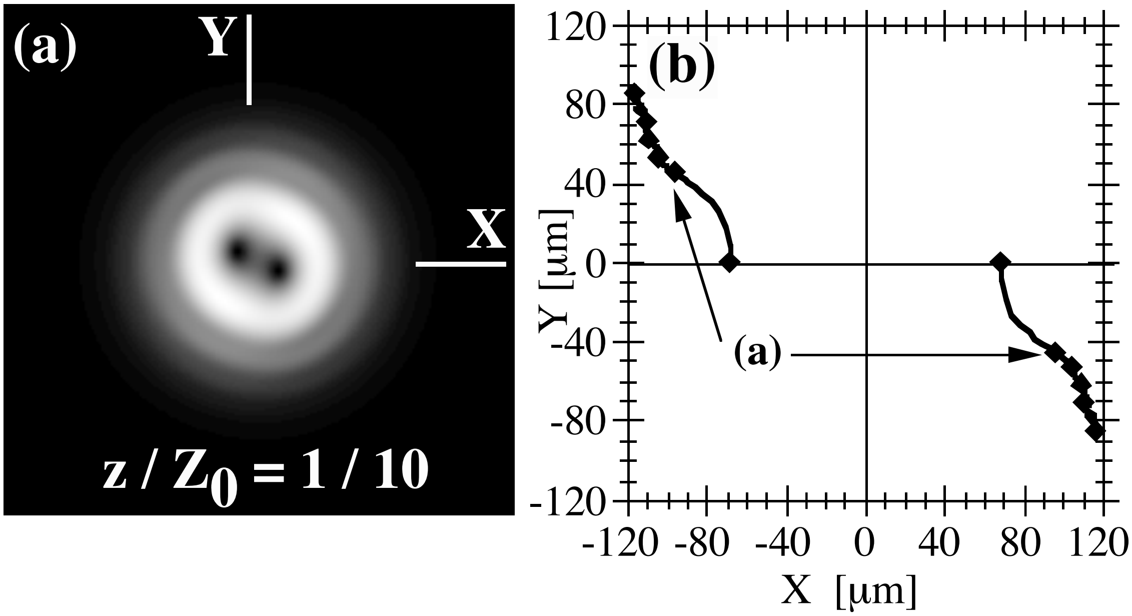

Fig. 4.13: Two vortex filaments of topological charge, $m = +1$, and separation, $d_{\mathrm{V}} = 2r_0 = 137$ [μm] are initially placed at the points $(\pm r_0, 0)$ on a Gaussian background beam of size $w_0 = 488$ [μm]. The beam, shown at the distance $z = 0.10 \times Z_0$, shows the vortex rotation effect. The projection of the vortex trajectories onto the transverse plane is depicted in (b), where diamonds mark propagation intervals of $\Delta z = Z_0/10$.

how the vortex dynamics is affected by both the beam size, w_0, and the separation, d_{V}. In Figs. 4.14(a-c) we have plotted numerically determined rotation angles as a function of distance for both linear and nonlinear propagation. (The nonlinear case is discussed in *Case 4* below). We show angle plots for more values of initial vortex separation in Fig. 4.15. In all three Figs. 4.14(a-c) plots, we find large initial rates of rotation (compared to the Gouy rate in Eq. (4.26)), as expected. However, we find a surprising result for the linear case in Fig. 4.14(a), where we consider two closely spaced vortices in a large background field ($w_0 = 1464[\mu\mathrm{m}]$, $d_{\mathrm{V}}/w_{\mathrm{V}} = 2.40$, and $w_{\mathrm{V}} = 57[\mu\mathrm{m}]$): the rotation angle, $\phi_{\mathrm{V}}(z)$, indicates that the rotation reverses direction after some distance! This retrograde motion may occur owing to two competing sources of amplitude gradients: the background Gaussian beam and the diffracting neighboring vortex. According to the vortex hypothesis, the effective "background" field determining the motion of vortex 1 is given by the field of both vortex 2 and the Gaussian beam. The gradient of the amplitude of the Gaussian beam is directed radially outward from the center of the beam, as usual; however, at some distance, z, it may be relatively weak compared to the amplitude gradient of the overlapping vortex. Thus, the resultant direction of the amplitude gradient may switch directions as the diffracting envelope from one vortex begins to overlap the other, i. e., the background gradient may switch from being radially outward (with respect to the center of the beam) to radially inward. Therefore, the direction of rotation, $m\vec{k} \times \vec{\nabla}_{\perp} G_{BG}$ (where G_{BG} is the effective background field), may reverse as the beam propagates.

By increasing the vortex separation distance, the vortices may rotate as quasi-point vortices for longer propagation distances, and thus, larger rotation angles may be achieved. This is verified in Fig. 4.14(b) for the case $d_{\mathrm{V}}/w_{\mathrm{V}} = 6.8$, where we also

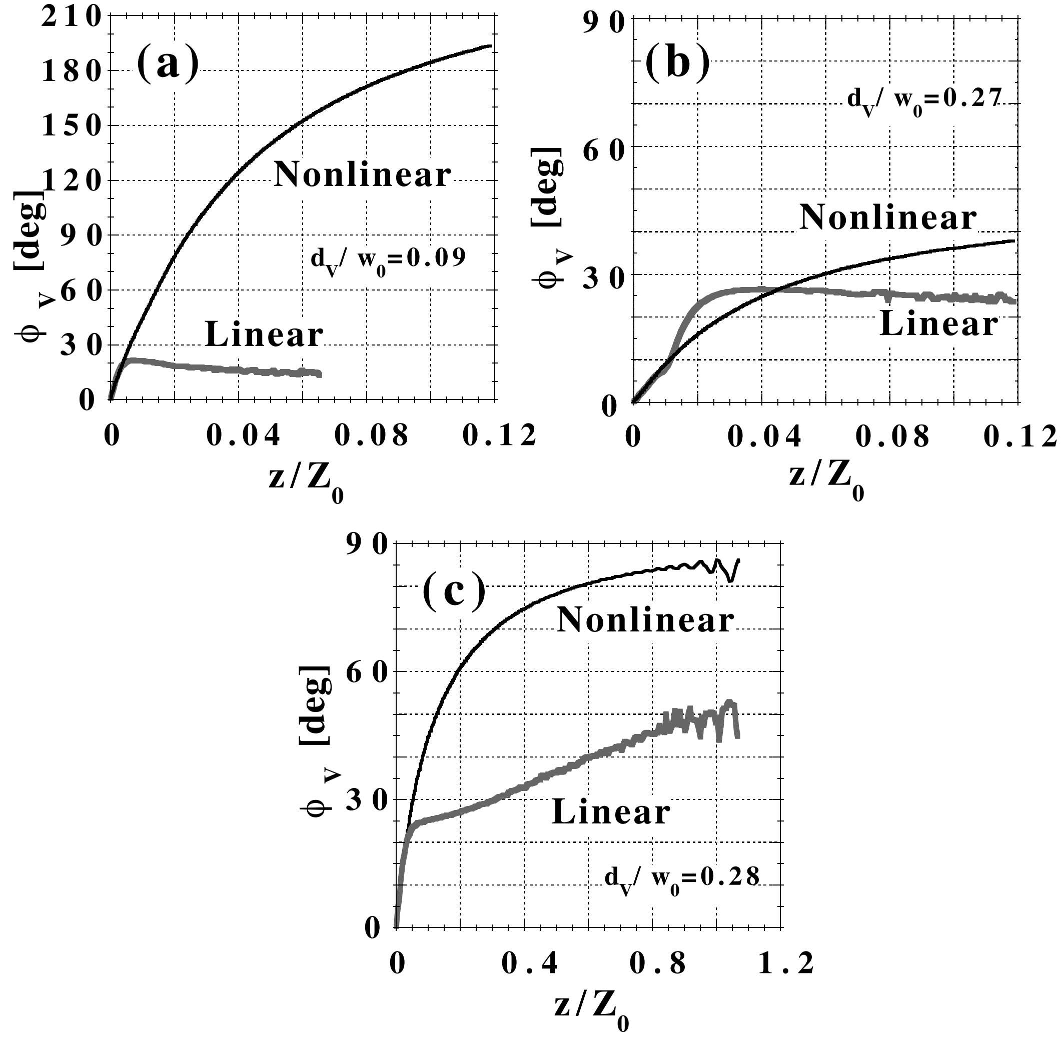

Fig. 4.14: Angle of rotation, ϕ_V, versus the propagation distance, z, in linear and nonlinear media for a pair of vortex filaments of size, $w_V = 57$ [μm], and separation, d_V, on a Gaussian background beam of size, w_0: (a) $d_V = 137$ [μm], $w_0 = 1464$ [μm] ($Z_0 = 8.4m$); (b) same as (a) except $d_V = 390$ [μm]; (c) same as (a) except $w_0 = 488$ [μm] ($Z_0 = 0.94m$).

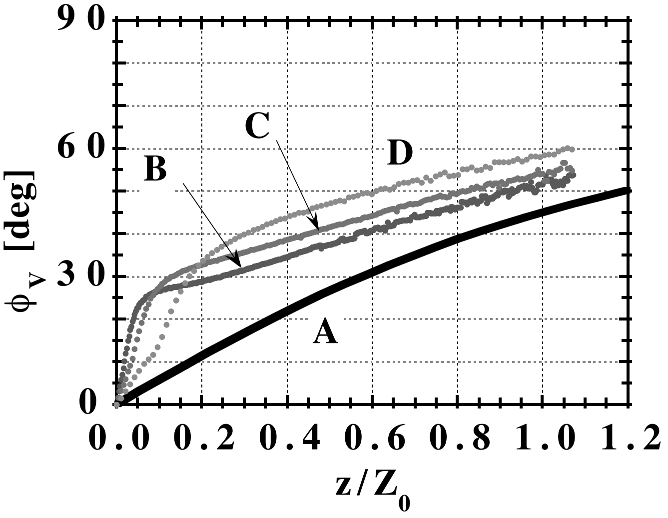

Fig. 4.15: Propagation of a pair of vortex filaments in linear media for different values of vortex separation, d_V. **A**: $\arctan(z/Z_0)$ (shown for comparison), **B**: d_V = 185 [μm], **C**: d_V = 244 [μm], **C**: d_V = 390 [μm]. w_0 = 488 [μm], Z_0 = 0.936.

find retrograde motion. On the other hand, if the background beam size, rather than d_V, is reduced, the amplitude gradient of the the background beam may dominate the amplitude gradient of the neighboring vortex, resulting in no backward rotation effect. Indeed this suggested effect is observed in Fig. 4.14(c) for the case w_0 = 488 [μm], $d_V/w_V = 2.40$, and w_V = 57 [μm]. Note that Figs. 4.14(a-c) show actual data points, not smoothed curves. The noise in the data for large values of z is a numerical artifact attributed to the uncertainty of the vortex position.

In each of the cases shown in Figs. 4.14(a-c), the initial rate of vortex filament rotation, $\Omega(z = 0)$, exceeds that occurring for r-vortices (Eq. 4.21), e.g. by two orders of magnitude in (a). We performed numerical simulations for OV pair propagation with varying values of the beam size, w_0, initial vortex pair separation, d_V, and initial vortex size, w_V. We measured the initial rate of rotation, $\Omega(z = 0)$, for each of those

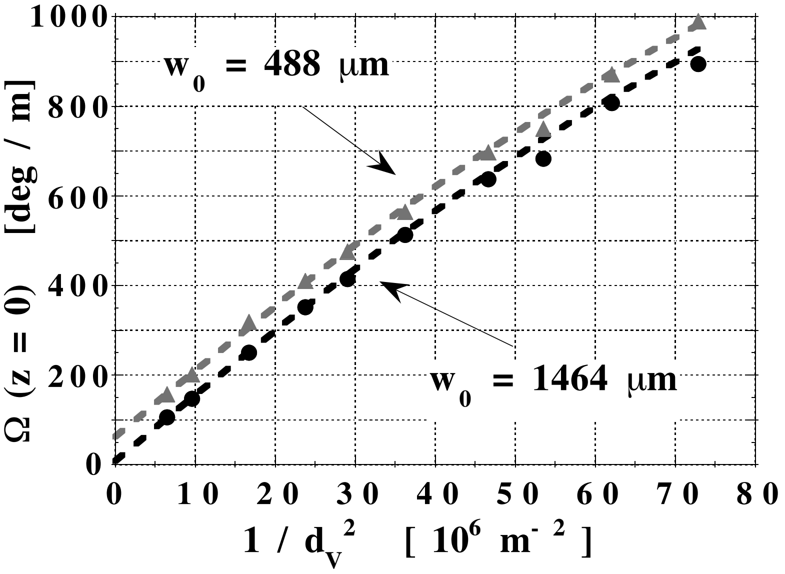

Fig. 4.16: Initial rate of vortex filament pair rotation $\Omega(z = 0)$ is plotted for different separation distances, d_{V}, and background beam sizes, w_0. Dashed lines show theoretical curves from Eq. (4.28) with no adjustable parameters. Note: Fig. 4.14 indicates that $\Omega(z = 0)$ is the same for both linear and nonlinear propagation.

simulations. This data, plotted in Fig. 4.16, suggests that this rate is not simply determined by the phase the neighboring vortex, as expressed in Eq. (4.20), but that it also depends on the beam and vortex sizes, w_0 and w_{V}. (Note that the initial Gouy rates correspond to the values on the ordinate in Fig. 4.16.) If the rotation rate were independent of w_{V} these graphs would be linear. In Fig. 4.16 we can see how the initial overlap of vortex cores causes the departure from linear dependence for smaller values of d_{V} (on the right hand side of the graph). The rightmost point on the graph corresponds to the case where $d_{\mathrm{V}} \sim 2w_{\mathrm{V}}$.

We suggest corrections owing to amplitude gradients of both the background Gaussian beam and the neighboring vortex filament, which we evaluate at a vortex core:

$$\begin{aligned} &\left|\vec{\nabla}_{\perp}\left(A(r,z=0)G_{BG}(r,z=0)\right)\right|_{r=d_{\mathrm{V}}/2} = \\ &\left|2A(r,z=0)G_{BG}(r,z=0)\left[\frac{r}{w_0^2}+\frac{1}{w_{\mathrm{V}}\sinh\left(\dfrac{r+d_{\mathrm{V}}/2}{w_{\mathrm{V}}}\right)}\right]\right|_{r=d_{\mathrm{V}}/2}. \end{aligned} \tag{4.27}$$

Applying the same method used to obtain Eq. (4.14), we determine a correction to Eq. (4.20), $\Omega'(z=0)$, such that the initial rotation rate for vortex filaments may be written:

$$\Omega_{\tanh}(z=0) = \Omega_d + \Omega'(z=0) = \frac{\lambda}{\pi}\left[\frac{1}{d_{\mathrm{V}}^2}+\frac{1}{w_0^2}-\frac{2}{d_{\mathrm{V}}w_{\mathrm{V}}\sinh\dfrac{2d_{\mathrm{V}}}{w_{\mathrm{V}}}}\right] \tag{4.28}$$

The dashed lines in Fig. 4.16 show that the theoretical curves from Eq. (4.28) agree remarkably well with the numerical data (no adjustable parameters have been used).

Case 4. In self-defocusing nonlinear media, vortices may propagate as solitons, and hence, the problems with diffracting vortex filaments (discussed in *Case 3*), may be avoided, thereby allowing anomalously large vortex rotation angles. The core size of an optical vortex soliton is approximately given by[7,78]

$$w_{\mathrm{OVS}} = 1.270\, k^{-1}(n_0/\Delta n_{NL})^{-1/2}, \tag{4.29}$$

where $\Delta n_{NL} = -n_2 E_0^2/2$ is a characteristic change of refractive index, n_2 is the coefficient of nonlinearity ($n_2 < 0$), and n_0 is the linear refractive index. For an OVS with $w_{\mathrm{OVS}} = 57$ [μm], the intensity of the beam must be adjusted to obtain a nonlinear index change of $\Delta n = 8.0 \times 10^{-6}$ (assuming $\lambda = 800$ [nm] and $n_0 = 1$). Although this value can be achieved in some materials, the propagation distances required to observe the rotations can be large (by optical material standards): on the order of $4\pi w_{\mathrm{OVS}}^2/\lambda$, or at least 5 [cm]. Shorter optical path lengths require not only larger values of Δn, but also a precise means of creating closely spaced vortices having small cores. Fortunately, numerical simulations do not suffer from these restrictions, and we can investigate a variety of configurations to determine which may be most suitable for experiments.

Let us now examine the nonlinear propagation dynamics of OVS's, assuming the same initial field used in *Case 3* for vortex filaments. The resulting intensity profiles are shown in Figs. 4.17(a-c) for three different near-field propagation distances for the case $w_0 = 1464$ [μm], $d_{\mathrm{V}}/w_{\mathrm{V}} = 2.40$, and $w_{\mathrm{V}} = 57$ [μm]. The intensity profile after propagating a distance $z/Z_0 = 0.01$ into the self-defocusing material is depicted in Fig. 4.17(b), showing a rotation angle roughly two orders of magnitude larger than the Gouy phase at this distance. What is more, Figs. 4.17(c) and (d) demonstrate that rotation angles of 180° and more are possible. This result significantly exceeds the 90° limit of the Gouy phase described by Eq. (4.4). The vortices not only rotate, but also move radially outward as the beam propagates. This apparent repulsion is

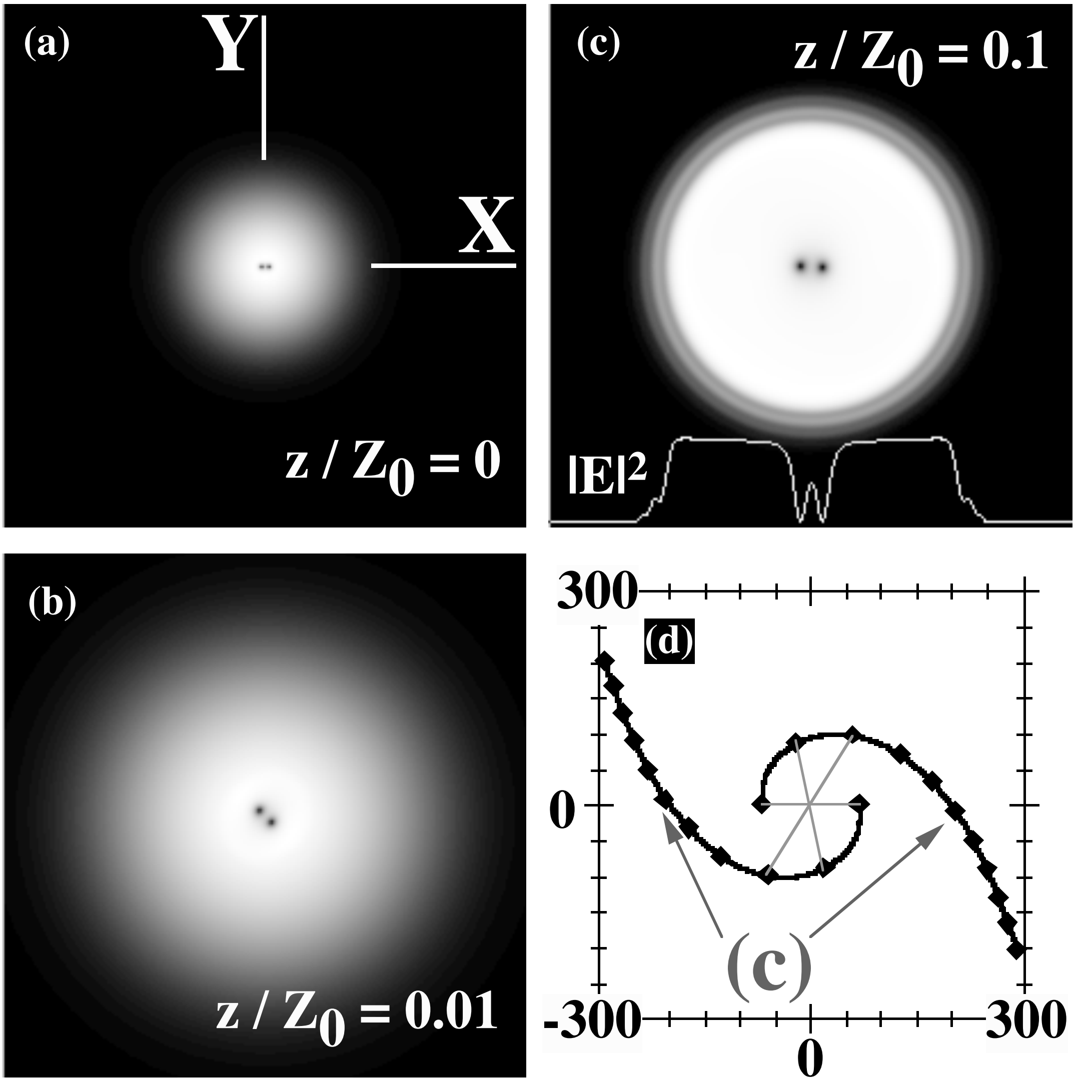

Fig. 4.17: Propagation of a pair optical vortex solitons of charge $m = +1$, with initial conditions (a): $d_V = 137\,[\mu\text{m}]$, $w_V = 57\,[\mu\text{m}]$, $w_0 = 1464\,[\mu\text{m}]$. A large clockwise rotation is evident over a short distance in (b), with a rotation angle exceeding 180° demonstrated in (c). The projections of vortex trajectories onto the transverse plane are shown in (d), where diamonds mark propagation intervals of $\Delta z = Z_0/50$. Logarithmic gray-scale palettes are normalized to maximum intensities of each image.

driven by the amplitude and phase profiles of the background beam, which expands due to the self-defocusing and diffraction. The resulting trajectory is a spiral shape, shown in Figs. 4.17(d). Rotation angle plots for different values of initial soliton separation, d_{V}, and Gaussian beam size, w_0 are given in Figs. reffig:dall and 4.19, respectively.

We note that in Fig. 4.17(c) the amplitude profile of the background beam appears relatively uniform, which is characteristic of "optical blooming" of a Gaussian laser beam in self-defocusing media. However, the intensity in the region near the vortices is non-uniform, and hence, in a nonlinear medium, the nonlinear component of the phase, $n_2 Ikz$, will also be non-uniform. Let us examine how this nonlinear phase component affects the motion of a vortex. Let us assume the vortex on the right-hand side of Fig. 4.17(c) resides in a non-uniform background field, G. The amplitude gradient may not only oppose the rotation in the $m\vec{k} \times \vec{\nabla}_{\perp} G$ direction, as discussed in Sec. 4.4, but also contribute to a translation, owing to the nonlinear term in the phase: $m\theta + \Phi - kz(1 + (n_2/n_0)|G|^2)$, i.e., $\Phi_{NL} = -(n_2/n_0)|G|^2 kz$. Based on the fluid paradigm (see Sec. 4.4) the nonlinear contribution to the transverse momentum of the vortex should be given by

$$\vec{k}_{\perp}^{(NL)} = -\vec{\nabla}_{\perp}\Phi_{NL} = +(kzn_2/n_0)\vec{\nabla}_{\perp}|G|^2, \tag{4.30}$$

when evaluated at the vortex core. In self-defocusing media, $n_2 < 0$, and thus, the right-hand vortex in Fig. 4.17(c) (which experiences a positive gradient owing to the vortex on the left) should be attracted to the neighboring vortex. Thus, in a nonlinear medium, vortices (of any sign or charge) experience attraction, in addition to motions governed by the linear part of the system. Owing to the rotational motion of the vortices, and the nonlinear attraction, stable orbits may be possible. Numerical

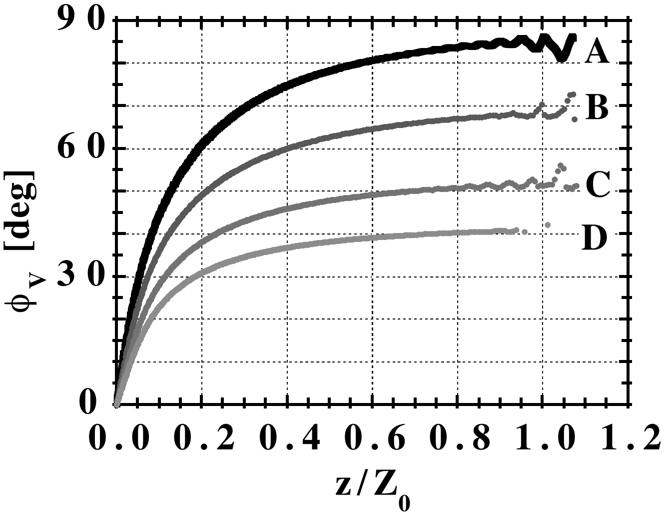

Fig. 4.18: Propagation of a pair of OVS's in a Gaussian beam through self-defocusing nonlinear media for different values of initial separation, $d_{\rm V}$. **A**: $d_{\rm V} = 137\,[\mu{\rm m}]$, **B**: $d_{\rm V} = 166\,[\mu{\rm m}]$, **C**: $d_{\rm V} = 205\,[\mu{\rm m}]$, **D**: $d_{\rm V} = 244\,[\mu{\rm m}]$. $w_0 = 488\,[\mu{\rm m}]$, $Z_0 = 0.936$, $w_{\rm V} = 57\,[\mu{\rm m}]$.

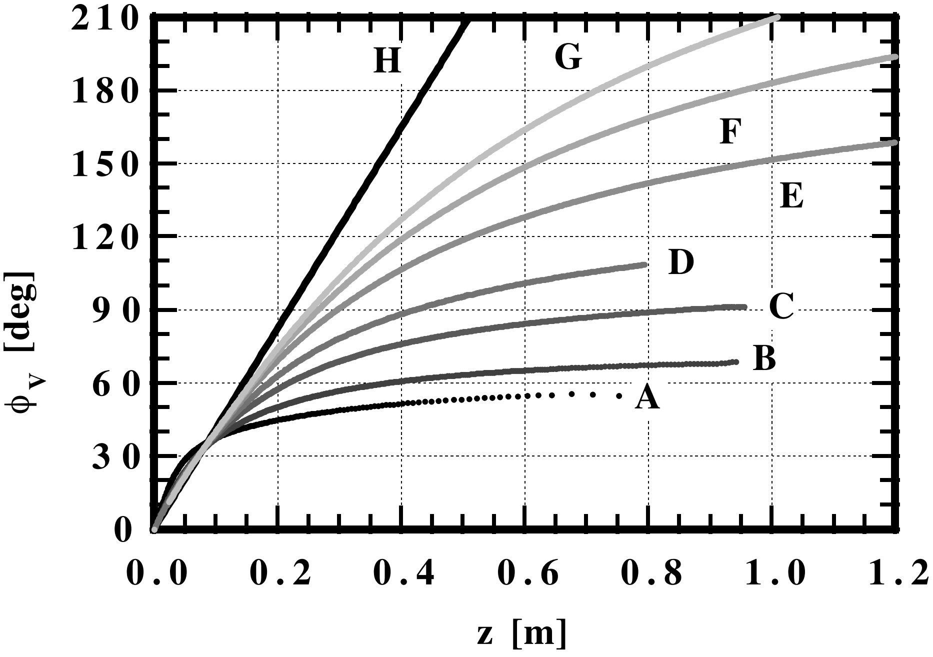

Fig. 4.19: Propagation of a pair of OVS's in a Gaussian beam through self-defocusing nonlinear media for different sizes of the background Gaussian beam, w_0. $w_V = 57\,[\mu\text{m}]$. Initial separation $d_V = 166\mu m$. **A:** $w_0 = 244$ [μm], **B:** $w_0 = 488$ [μm], **C:** $w_0 = 732$ [μm], **D:** $w_0 = 976$ [μm], **E:** $w_0 = 1464$ [μm], **F:** $w_0 = 1952$ [μm], **G:** $w_0 = 2440$ [μm], **H:** plane wave ($w_0 \to \infty$).

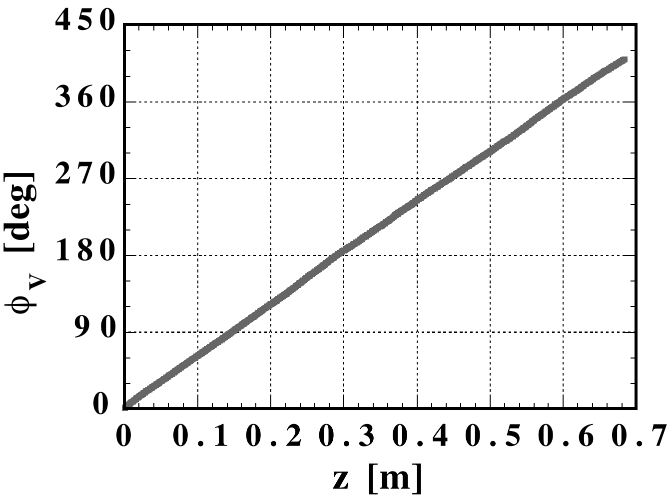

Fig. 4.20: Propagation of a pair of OVS's on a plane wave background. In this simulation, $w_{\mathrm{OVS}} = 35$ [μm], $\Delta n = 2.1 \cdot 10^{-5}$, $d_{\mathrm{V}} = 140$ [μm].

investigations confirm such orbital motion. In Fig. 4.20 we show the angle of rotation, ϕ_{V}, for a pair of OVS's on a plane wave background. This plot shows rotation over more than 360°.

Though nonlinear effects complicate the description of OVS rotation, we propose that an experiment could achieve results similar to the numerical results shown in Fig. 4.14(a), achieving rotation angles in excess of the Gouy limit of 90° (see the curved marked "Nonlinear"). It is also possible to observed the opposite effect, namely less rotation in the nonlinear case compared to the linear case, as numerical calculations indicate in Fig. 4.14(b). This somewhat anomalous effect may have already been observed in by Luther-Davies *et al.*;[142] however, in that case OVS's were probably not achieved, owing to the use of a short focal length lens in front of the nonlinear cell (also, the focusing of the beam results in the observation of the far-field profiles at the output face of the cell, while most of the dynamics discussed above happen in the near-field). In the far-field, angle of rotation is expected to be greater in the linear case (compared to the nonlinear case) when the vortex separation, d_{V} is comparable to the diameter of the Gaussian beam, $2w_0$. In this situation the fluid-like behavior is not prevalent and the vortex rotation will be driven by the amplitude gradient of the background beam, which is reduced in the nonlinear case owing to self-defocusing blooming.

Another effect that may be experimentally confirmed occurs when the beam size is made small. In this case we expect from our numerical results, in Fig. 4.14(c), that it is possible to enhance the rotation angle (by a factor of two in this case) in a nonlinear medium, but still not exceed 90° in the near-field region. An experimental observation of this phenomenon is presented in Section 5.3.

4.6 Conclusions

We have examined three factors affecting the motion of optical vortices: an amplitude gradient, a phase gradient, and a nonlinear factor depending on the intensity gradient. We found how the former two factors qualitatively and quantitatively describe the initial rotation rates observed in our numerical investigations. We found contrasting differences between the trajectories for r-vortices having globally distributed core functions, and vortex filaments having localized core functions when the beam propagates through a linear medium. In particular, identical localized vortices with non-overlapping cores were found to orbit each other at a rate that depends inversely on the squared vortex separation distance. This latter phenomenon is analogous to the rotation of point vortices in fluid dynamics. In a linear medium vortices diffract, becoming non-localized, and hence, the maximum rotation angle of the vortex pair is limited. However, in a self-defocusing medium, the vortices may propagate as non-diffracting optical vortex solitons, and thus, anomalously large rotation angles may be achieved. What is more, stable orbits may be possible, owing to an attractive nonlinear interaction between overlapping optical vortex solitons.

5. EXPERIMENTAL RESULTS

5.1 Introduction

Earlier in Chapter 4 we described the fluid-like behavior of small-core optical vortices.[85] In particular, two experimentally verifyable phenomena were emphasized. Pairs of small-core OV's are expected to exhibit initial rotation rates proportional to the inverse square of vortex separation, d_{V}. These rates may be orders of magnitude higher than those previously measured for large-core vortices. We report the first experimental observation of this effect in Section 5.2 of this Chapter. In linear media the initial fluid-like behavior is not sustained upon propagation owing to diffractin of vortex cores. However, in self-defocusing nonlinear media we expect the high initial rotation rates to be sustained for longer propagation distances. This may result in the enhancement of the net rotation angle of the vortex pair in nonlinear media, compared to linear. We report the first experimental observation of this phenomena in Section 5.3.

5.2 Experimental Observation of Fluid-like Motion of Optical Vortices in Linear Media

It is well known that two identical vortex filaments in an incompressible inviscid fluid orbit each other at a rate inversely proportional to the orbital area[86–88, 183] owing to an effective interaction manifested in the flow field (see Appendix A). On the other hand, it has been shown analytically[57] and experimentally[56] that optical vortices (OV's) in a propagating beam having a Gaussian intensity profile exhibit rotation rates that are independent of the separation distance. This contrast seems to suggest that fluid-like effective interactions between OV's do not occur. However, both the fluid flow and the diffraction of light may be described using potential theory, and one may expect similar phenomena to occur in both systems, as explained above in Section 4.4. Here we describe the first experimental observation of an effective interaction between identical OV filaments, showing that over short propagation distances (i.e., before the vortices diffract and overlap), the rotation rate indeed varies inversely with the squared distance of separation.

We consider an initial field of the form given in Eq. (4.22) with $M = 2$, $m_1 = m_2 = 1$ and the vortices having initially small-core profiles, i.e. $A_j(r_j, z = 0) = \tanh(r_j/w_{\rm V})$. The vortex pair is placed so that its center coincides with the center of the Gaussian beam. The intensity and phase profiles of this field are depicted in Fig. 5.1 (a) and (b), respectively. We are primarily interested in so-called vortex filaments (or quasi-point vortices) which are characterized by a vanishing core size in the initial plane. Point vortices exist in the theoretical limit as $w_{\rm V} \to 0$, although the are not physical because the beam would contain infinite transverse momentum.

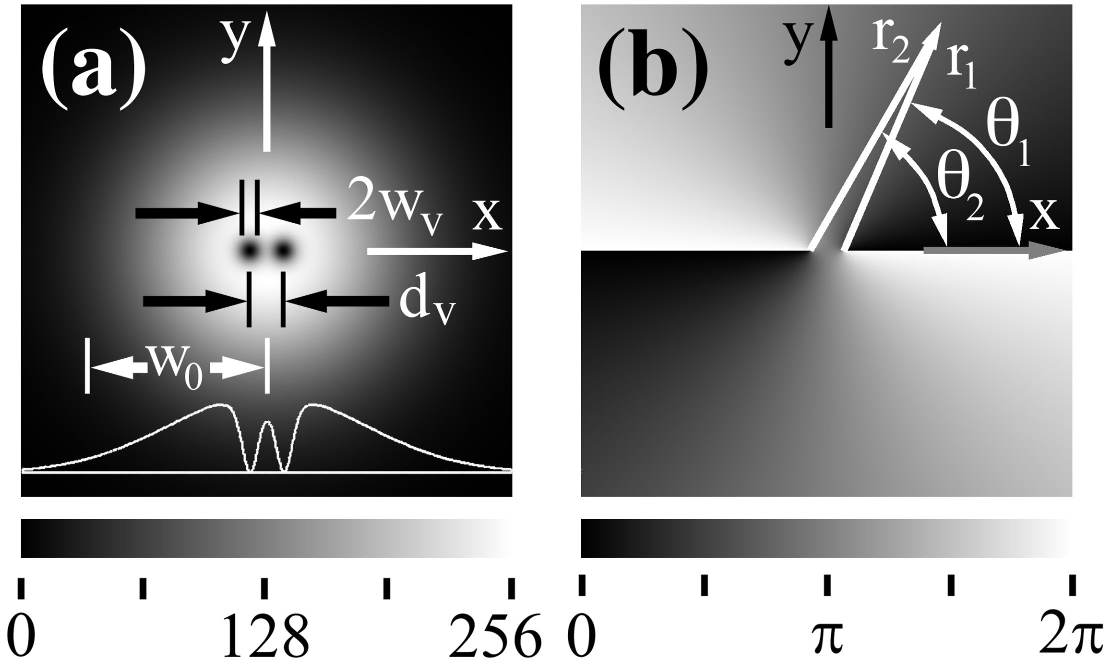

Fig. 5.1: (a) Intensity (log gray-scale) and (b) phase (linear gray-scale) profiles depicting two vortices of radial size w_V and separation d_V in the cross-section of a Gaussian beam of size w_0. The topological charge for each vortex is $m = 1$, resulting in a counter-clockwise phase circulation (b). A line plot of the intensity along the x-axis is shown in (a).

The paraxial approximation is assumed, i.e. $w_0 \gg w_{\rm V} \gg \lambda$.

Let us consider the propagation dynamics of the initial beam describe above as it evolves along the optical axis in the laboratory reference frame. A fluid-like description of the "flow" of photons may be heuristically understood using a ray optics model. (This approach is justified for the initial propagation of point vortices on a uniform background field, because the beam contains only phase information[85]). By using this method in Section 4.4, we found that the initial rate of rotation of the vortex pair shown in Fig. 5.1 is given by the following (see Eq. (4.21)):

$$\Omega_{\rm V} = \Delta\phi_{\rm V}/\Delta z = -\lambda/\pi d_{\rm V}^2 = -1/Z_{\rm V}, \tag{5.1}$$

where $De\phi_{\rm V}$ is the angular displacement of the vortices from their initial position, $d_{\rm V}$ is the initial vortex separation distance and $Z_{\rm V} = \pi d_{\rm V}^2/\lambda$ is the characteristic diffraction distance for the pair. Diffraction may be expected to significantly affect this rate after a propagation distance $\Delta z \approx Z_{\rm V}$, and thus, Eq. (5.1) accounts for rotation angles up to roughly one radian. Thus, we believe the analogy between optical and hydrodynamic vortex filaments is justified over short propagation distances.

In contrast, "conventional" optical vortices[46,184] have a core function, $A_j(r_j) = r_j/w_{\rm r}$, where $w_{\rm r}$ is a parameter characterizing the slope of the vortex core, but not the size; rather, the size is on the order of the background beam size. The propagation dynamics for such a large core function is significantly different from that of a quasi-point vortex. For an arbitrary number and placement of identical conventional vortices on a Gaussian background field, the rotation rate depends only on the size of the background beam:

$$\Omega_{\rm G} = -{\rm d}\phi_{\rm G}/{\rm d}z = -\left[1 + (z/Z_0)^2\right]^{-1} Z_0^{-1}, \tag{5.2}$$

where $Z_0 = \pi w_0^2/\lambda$ is the characteristic diffraction length of the Gaussian background beam, and $\phi_{\mathrm{G}}(z) = \arctan(z/Z_0)$. On the other hand, the angular velocity for a point vortex pair may initially be many orders of magnitude larger than Eq. (5.2) - by a factor of $\phi_{\mathrm{V}}/\phi_{\mathrm{G}} = Z_0/Z_{\mathrm{V}} = (w_0/d_{\mathrm{V}})^2$, assuming $d_{\mathrm{V}} \ll w_0$. What is more, we point out that conventional vortices do not exhibit circular motion, but rather parallel rectilinear motion,[85] owing to a z-dependence of the separation distance. By induction, we conclude that only small core OV's exhibit fluid-like propagation dynamics.

To investigate the spiral trajectory of optical vortex filaments, we produced computer-generated holograms[16, 52] of two small-core vortices. Holograms having a grating period of 120 [μm] were recorded onto acetate sheets using a Linotronic laser printer with a 5080 dot/inch resolution. The holographic image of the vortex pair was initially reconstructed with a 34 [mm] diameter collimated single frequency Argon ion laser beam of wavelength 514 [μm]. The first order diffracted beam containing the vortex pair was spatially filtered with a 310 [mm] focal length achromatic lens, L_1, and a 400 [μm] diameter pinhole, P, as shown in Fig. 5.2. A second lens, L_2, of focal length 63 [mm], was used to re-collimate and reduce the beam to a size $w_0 = 3.5$ [mm]. In the image plane (where we set $z = 0$), we measured the vortex size to be $w_{\mathrm{V}} = 60$ [μm]. The vortex separation distance was measured to range from $d_{\mathrm{V}} \approx 100$ to 250 [μm] for different holograms. For the cases $d_{\mathrm{V}} > 120$ [μm], the pair of vortex cores did not significantly overlap, i.e., they satisfied the quasi-point vortex condition: $2w_{\mathrm{V}} < d_{\mathrm{V}} \ll w_0$.

Cross-sectional intensity profiles were recorded at various propagation distances (see for example Fig. 5.3(a-c)) by translating an assembly containing a microscope

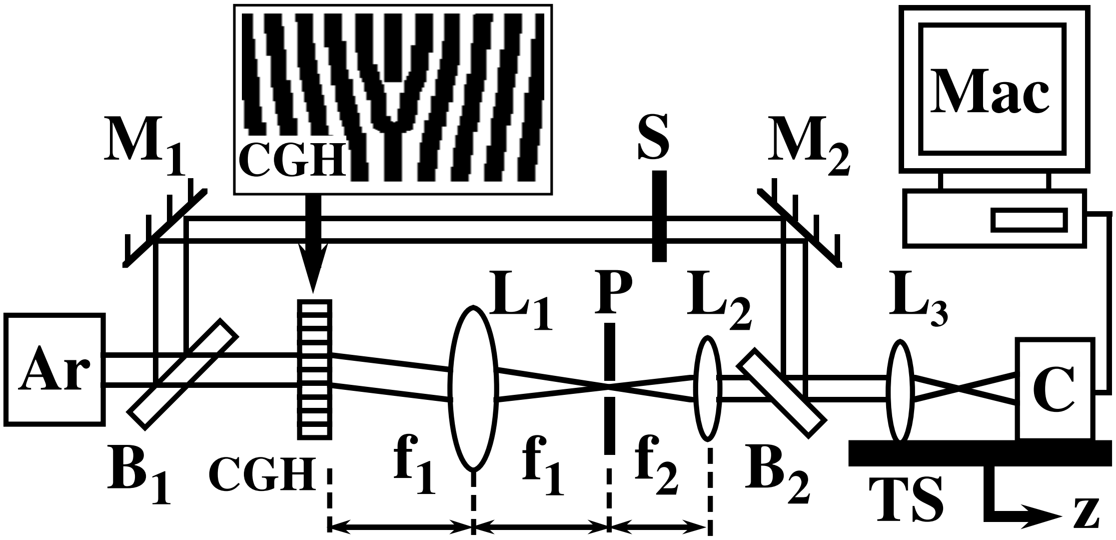

Fig. 5.2: Experimental setup: (Ar) - single frequency Argon ion laser $\lambda = 514\,[\mathrm{nm}]$; $\mathrm{B_1, B_2}$ - beam splitters; (C) - CCD camera; (CGH) - computer generated hologram (inset shows central region) with incident collimated beam of diameter 34 [mm]; $(\mathrm{L_1, L_2})$ - lenses with focal lengths, $\mathrm{f_1} = 310$ [mm], $\mathrm{f_2} = 63$ [mm], respectively; $(\mathrm{L_3})$ - microscope objective (N.A. = 0.25); $(\mathrm{M_1, M_2})$ - mirrors; (Mac) - Macintosh IIfx computer and framegrabber; (P) - diameter pinhole; (S) - shutter; (TS) - translation stage aligned with the optical axis, z.

objective (L_3) and a CCD camera. The corresponding interferograms, shown in Fig. 5.3(d-f) and displaying the unique forking pattern of two singly charged vortices, were obtained by opening a shutter (S) along the reference arm of a Mach-Zehnder interferometer. Relative positions of the vortices were obtained from the recorded profiles, which allowed us to determine the angular position, ϕ_{V}, and the separation distance at various propagation distances, z, from the image plane. By roughly aligning the axis of the translation stage with the optical axis of the beam, the vortices appeared to move about a common axis; although measurements of the absolute positions of the vortices would be needed to verify this.

Initial rotation rates at $z = 0$, shown in Fig. 5.4, are in good agreement with the values predicted by Eq. (5.1) for $d_{\mathrm{V}} > 2w_{\mathrm{V}}$, as expected. An example of the varying rotation angle for the case $d_{\mathrm{V}} = 105 \pm 9\,[\mu\mathrm{m}]$ is plotted in Fig. 5.5, which shows a peak rotation at $z \approx Z_{\mathrm{V}} = 6.7\,[\mathrm{cm}]$, and rotation angles spanning 40° over a range of $11\,[\mathrm{cm}]$. In Fig. 5.6 we show the evolution of the separation distance, d_{V}, for the same case (initial $d_{\mathrm{V}} = 105 \pm 9\,[\mu\mathrm{m}]$). From these two graphs we were able to determine the relative vortex trajectories shown in Fig. 5.7, assuming a stationary axis of motion for the vortices. The trajectories for three different values of d_{V}, indicate that the initial orbital motion of the vortex cores is followed by a repulsion from the center. The peak rotation angles experienced in these cases were two orders of magnitude larger than the angular position, ϕ_{G}, for conventional vortices, and thus, the observed effect may be solely attributed to the effective vortex-vortex interaction.

The departure from circular motion seen in Fig. 5.7, and the decelerated rotation rate seen in Fig. 5.5, is attributed to radiation from the diffracting vortex cores for $|z| > Z_{\mathrm{V}}$. The surprising decrease in the value of $|\phi_{\mathrm{V}}|$ after reaching a peak value, as

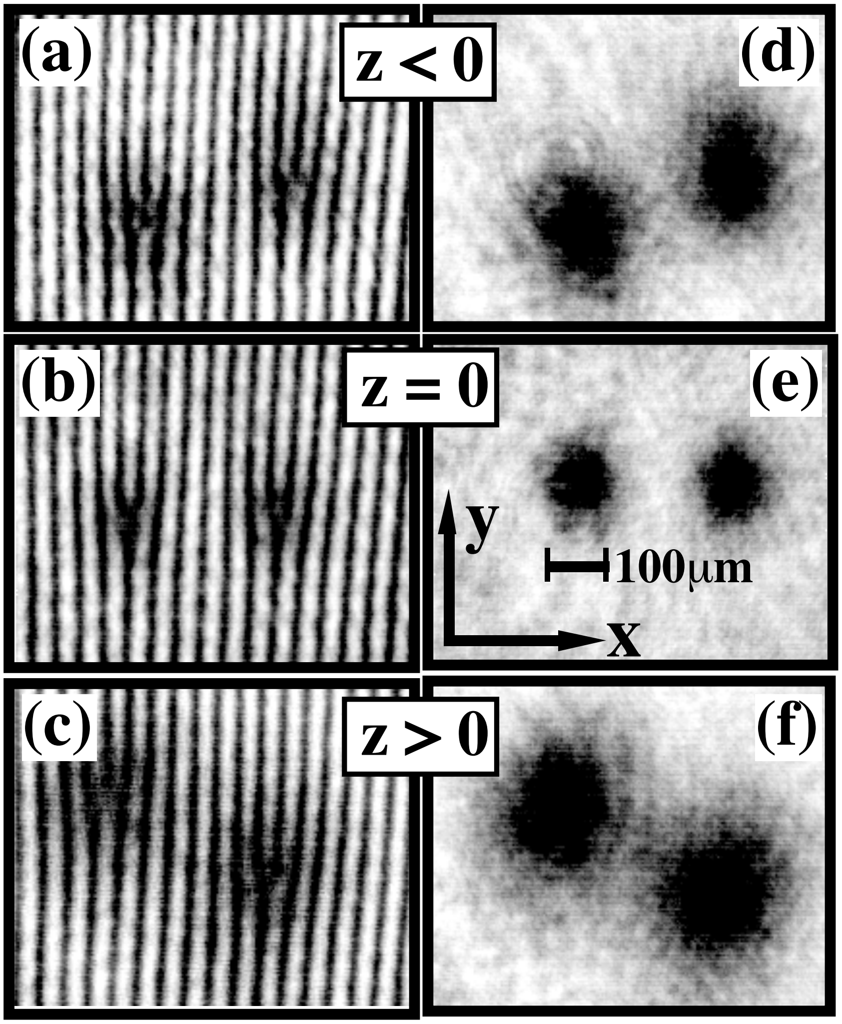

Fig. 5.3: Intensity (a)-(c) and interference (d)-(f) profiles of vortices of initial size, $w_{\mathrm{V}} \approx 60$ [μm], at different propagation distances (camera view). The vortices rotate clockwise for increasing values of z, as expected for positive topological charges.

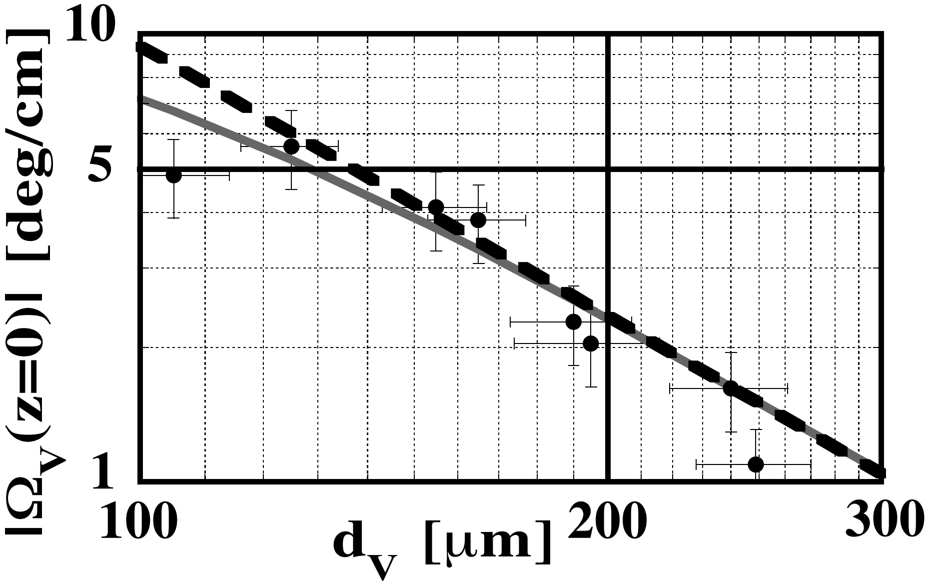

Fig. 5.4: Experimental (points) and theoretical (curves) initial rotation rates, $|\Omega(z=0)| = |\mathrm{d}\phi_\mathrm{V}/\mathrm{d}z|_{z=0}$, as a function of separation distance, d_V. The dashed line represents the rate for point vortices (from Eq. (5.1)), while the gray curve is predicted from Eq. (5.3), assuming $w_\mathrm{V} = 60$ [μm].

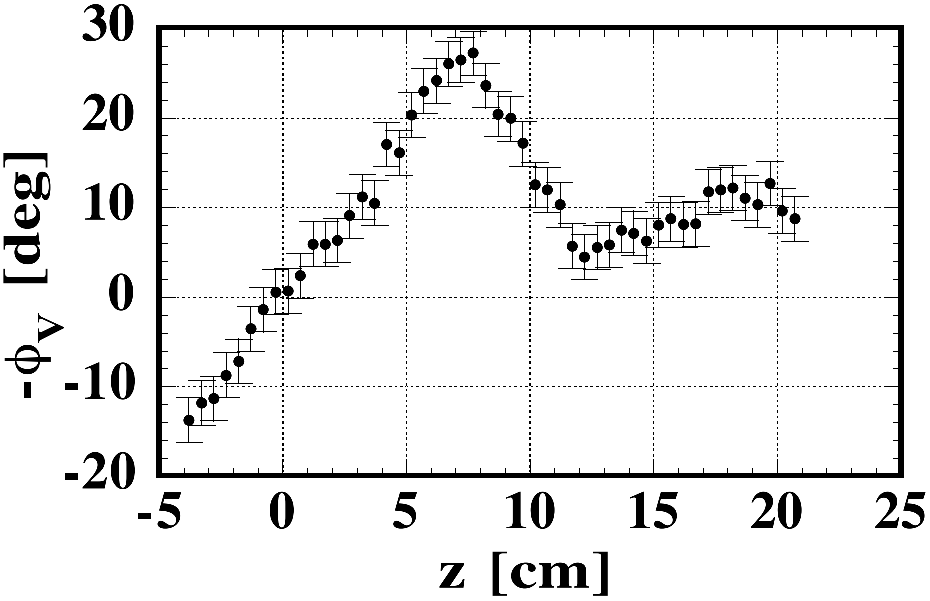

Fig. 5.5: Angular position of a vortex undergoing pair-wise rotation as a function of propagation distance, z, for an initial vortex separation distance, $d_{\mathrm{V}} = 105 \pm 9$ [μm] ($Z_{\mathrm{V}} = 67$ [mm]). The orbit is initially clockwise ($\Omega_{\mathrm{V}}(z = 0) < 0$).

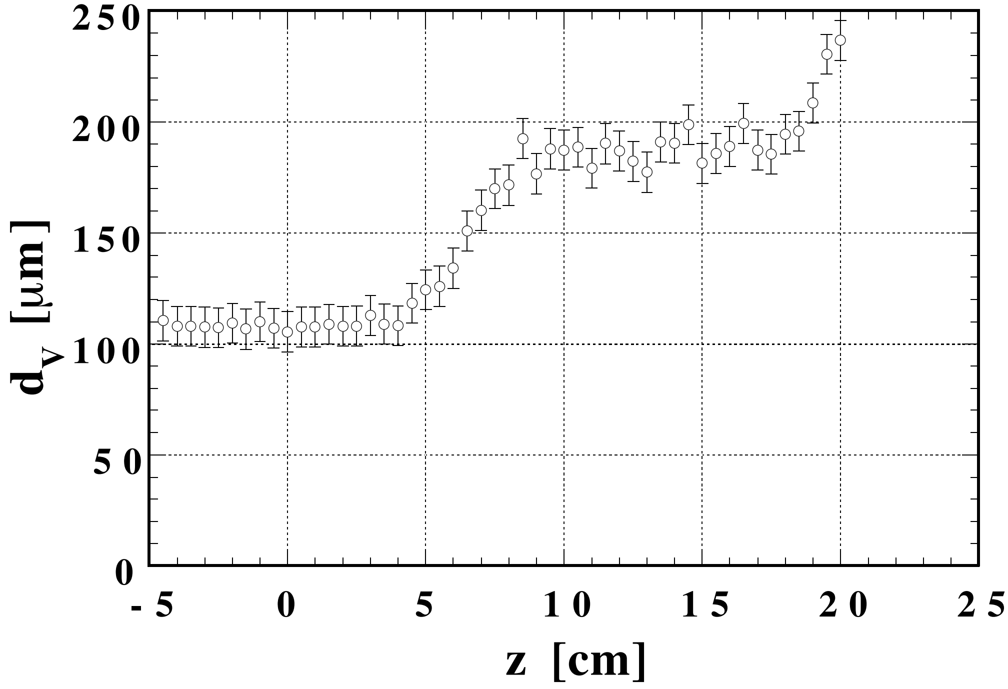

Fig. 5.6: Vortex pair separation, d_{V}, as a function of propagation distance, z, for a pair of vortices initially separated by $d_{\mathrm{V}} = 105 \pm 9\,[\mu\mathrm{m}]$ ($Z_{\mathrm{V}} = 67\,[\mathrm{mm}]$).

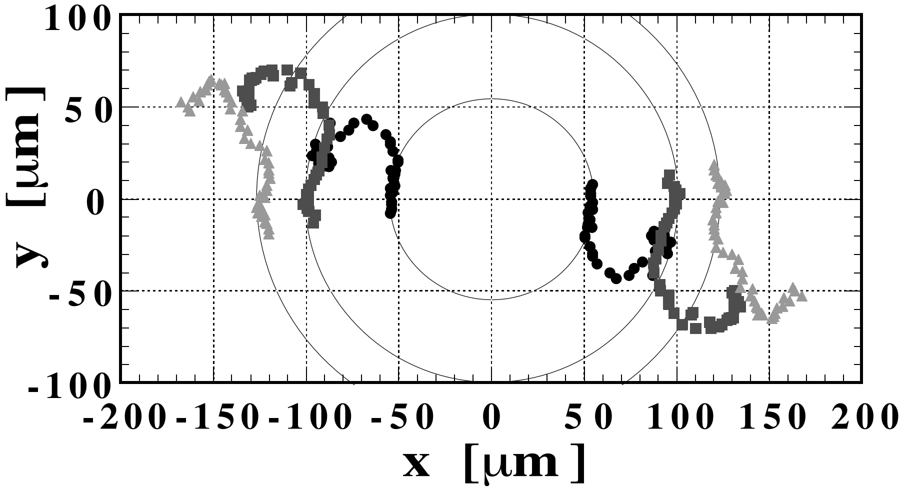

Fig. 5.7: Trajectories of vortex pairs in the transverse plane for initial separation distances, d_{V}, of 105 ± 9 [μm] (circles), 195 ± 17 [μm] (squares), 249 ± 21 [μm] (triangles). A common axis of motion has been assumed for the data.

seen in Fig. 5.5, may be understood by considering the effect of the amplitude gradient on the vortex trajectory. Once the vortex cores begin to overlap,[85] the non-uniform background field affects the vortex motion, and the rotation rate is estimated by

$$|\Omega_{\tanh}(z=0)| = (\lambda/\pi)[d_{\mathrm{V}}^{-2} + w_0^{-2} - 2/\{d_{\mathrm{V}} w_{\mathrm{V}} \sinh(2d_{\mathrm{V}}/w_{\mathrm{V}})\}] \tag{5.3}$$

The vortex size, w_{V}, increases with propagation distance owing to diffraction, and thus, Eq. (5.3) accounts for a decrease in the rotation rate in the vicinity of $|z| \approx Z_{\mathrm{V}}$. To obtain accurate results, however, numerical solutions of the scalar diffraction equation are necessary. On the other hand, the effects of diffraction may be avoided by propagating the beam through a self-defocusing nonlinear refractive medium, where the vortices propagate as optical vortex solitons.[7] In the latter case, numerical solutions[85] demonstrate that rotation angles exceeding 2π may be achieved.

5.3 Experimental Observation of Enhanced Rotation of Optical Vortex Solitons

In the previous Section we observed the fluid-like rotation of small-core optical vortices in linear media.[85, 90] The high initial rotation rates were not sustained upon propagation owing to the diffraction and overlap of vortex cores. In Chapter 4 we showed that in self-defocusing media these rotation rates are expected to be sustained for longer propagation distances[85] resulting in the enhancement of the net rotation angle, ϕ_V. This Section describes the first experimental observation of this nonlinear enhancement effect.[91, 92]

We consider the initial situation identical to the one treated in Section 5.2 and depicted in Fig. 5.1 - two unit-charge small-core vortices placed symmetrically with respect to the center of the background Gaussian beam

$$E(r, \theta, z = 0) = E_0 \exp\left(-r^2/w_0^2\right) \prod_{j=1}^{2} A_j(r_j, z = 0) \exp(i\theta_j), \tag{5.4}$$

where $A_j(r_j, z = 0)$ is the initial amplitude function of the vortex core. The vortices are initially located at (R_1, Θ_1) and (R_2, Θ_2), where $R_1 = R_2 = d_V/2$ and $\Theta_1 = \Theta_2$. In a self-defocusing Kerr material having a nonlinear coefficient, $n_2 < 0$, OVS's may form[7] (see Chapter 4). In the ideal case of plane-wave background $(w_0) \to \infty$ the cores do not radiate upon propagation and are stationary:

$$A_j(r_j, z) = \tanh(r_j/w_V), \tag{5.5}$$

where, $w_V \approx 1.270k^{-1}(n_0/\Delta n)^{1/2}$, is the soliton size, $\Delta n = -n_2 E_0^2$, is the characteristic nonlinear refractive index change, n_0 is the linear refractive index, and $k = 2\pi n_0/\lambda$ is the wavenumber. In practice, the finite Gaussian background field experiences optical blooming, and thus, the vortex cores may adiabatically expand as the beam propagates. If the initial core size is greater (smaller) than the soliton size, it may contract (expand) until a quasi-steady-state, i. e. adiabatic expansion, is reached.

By varying the beam power and observing the vortex cores at the output face of nonlinear cell, one may examine the change in vortex core sizes. When the core diameters become smaller than the vortex separation distance (i.e., $2w_{\mathrm{V}} < d_{\mathrm{V}}$), the cores are expected to propagate as vortex filaments.[85] Hence, as the beam power increases, we also expect to see the vortices rotate at the output face. Luther-Davies *et al.*[142] observed that when the vortex separatin is of the same order of magnitue as the size of the Gaussian background beam ($w_0 \sim d_{\mathrm{V}}$), the vortex rotation angle decreases with increasing power. In this regime, the fluid-like behavior is not exhibited and the vortex rotation is driven by the background beam amplitude and phase profile, which are flattened by nonlinearity of the media. To examine the opposite case of a nonlinear enhancement of the rotation angle, we produced a computer-generated hologram (CGH)[16,52] of closely-spaced vortices: $w_0 >> d_{\mathrm{V}}$. Two holograms were made and then re-recorded onto DuPont™ photopolymer film HRF-150X001-38* at a fringe spacing of roughly 1 [μm] to achieve a high efficiency, high damage threshold phase hologram. The core size in the plane of the hologram was measured to be $w_{\mathrm{V}} = 30 \pm 5$ [μm] for vortices separated by $d_{\mathrm{V}} = 135 \pm 4$ [μm], and $w_{\mathrm{V}} = 45 \pm 5$ [μm] for vortices separated by $d_{\mathrm{V}} = 84 \pm 4$ [μm].

A schematic of the optical system is shown in Fig. 5.8. An Argon ion laser beam ($\lambda = 0.514$ [mm], $P \approx 6$ [W], $w_0 = 1$ [mm]) is directed through a beam-splitter (BS_1) and hologram (H) and into a vertically aligned glass cell of length, $l_c = 290$ [mm],

---

* See Section 3.5 for the description of the recording process.

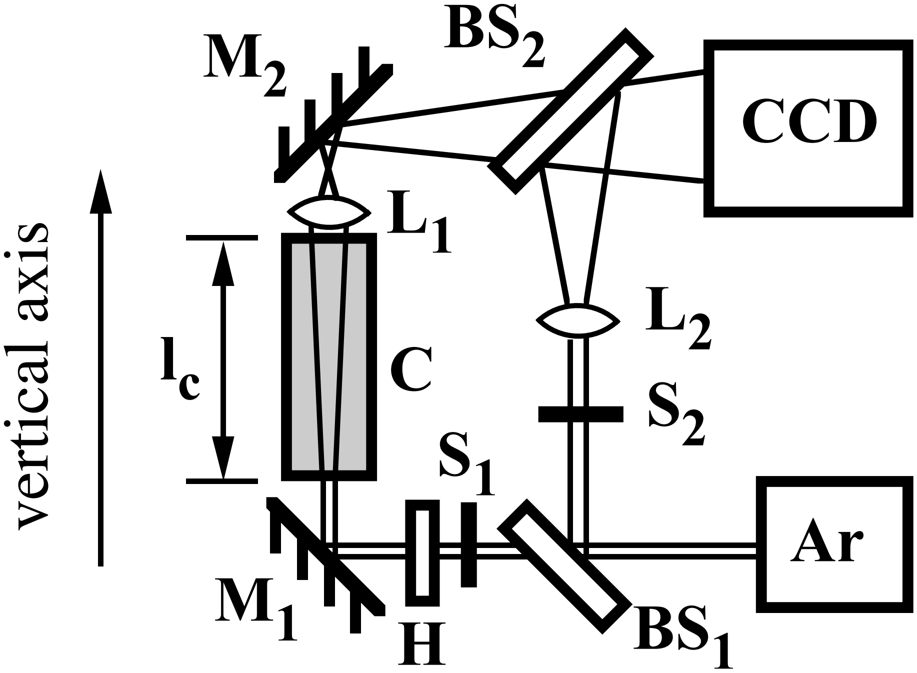

Fig. 5.8: Experimental setup: Ar - argon ion laser ($\lambda = 514$ [nm]), HRF - photopolymer hologram recording of a pair of small-core vortices, M_1 and M_2 - mirrors, C - vertical glass cell of length $l_c = 29$ [cm] filled with weakly absorbing nonlinear liquid (dyed methanol), L_1, L_2 - lenses of focal distance $f = 50$ [mm], CCD - CCD camera and frame grabber, S_1, S_2 - shutters.

containing a self-defocusing material - nigrosin dye dissolved in methanol ($n_0 = 1.33$) with an absorption coefficient, $\alpha^{-1} = 418$ [mm]†. The distance between the hologram and the input face of the cell was measured to be $l_{air} = 230$ [mm], resulting in the net optical path $l_{net} = l_{air} + n_0 l_c = 616$ [mm]. The output face of the cell was imaged with a lens (L_1) onto a camera (CCD). The beam-splitters were arranged to form a Mach-Zehnder interferometer, which allowed us to identify the center of the vortex cores. The laser provided non-uniform heating of the liquid, and a steady-state image appeared on the camera after roughly 3 [s]. The shutter, S_1, was closed between experiments to allow the methanol to return to thermal equilibrium.

The recorded intensity profiles and corresponding interferograms are shown in Fig. 5.9 at four different values of the beam power at the input face of the cell. In the low-power regime (see Fig. 5.9 (a) and (e)) the vortices at the output face have an angular displacement of ($\phi_V = 29°$ from their initial alignment ($\Theta_0 = -11.5°$ with respect to the x-axis) in the plane of the hologram, owing to linear vortex propagation dynamics.[90] Note that the vortices are unresolvable in Fig. 5.9 (a) owing to the diffraction of the vortices over the distance, lnet. As the laser power is increased to 0.4 [W], the vortex cores contract, as expected, and become resolvable owing to nonlinear refraction, as shown in Fig. 5.9 (b). At even higher powers the vortex axes appear to tilt away from the optical axis, owing to torsion,[181] and thus the cores become elliptical. This effect may be attributed to optically blooming of the background beam and radiated waves from the vortex cores. Even in this regime, however, the vortex cores remain resolvable and the interferograms allow us to clearly

---

[†] The absorption coefficient, α, was matched to achieve 50% absorption through the length of the nonlinear cell, l_c: $\exp(-\alpha l_c) = 0.5$

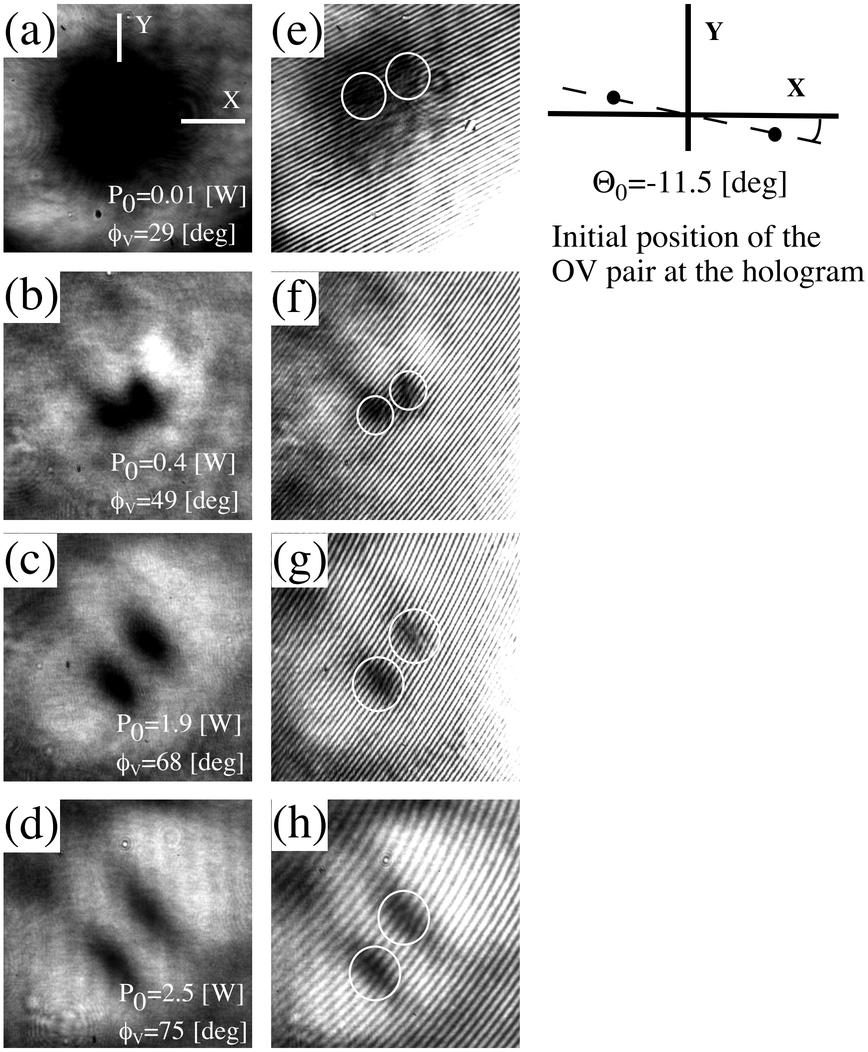

Fig. 5.9: Output intensity profiles for various values of incident power, P_0: (a) 0.01 [W], (b) 0.4 [W], (c) 1.9 [W], (d) 2.5 [W]. (e)-(h) - interference patterns corresponding to (a)-(d) intensity profiles.

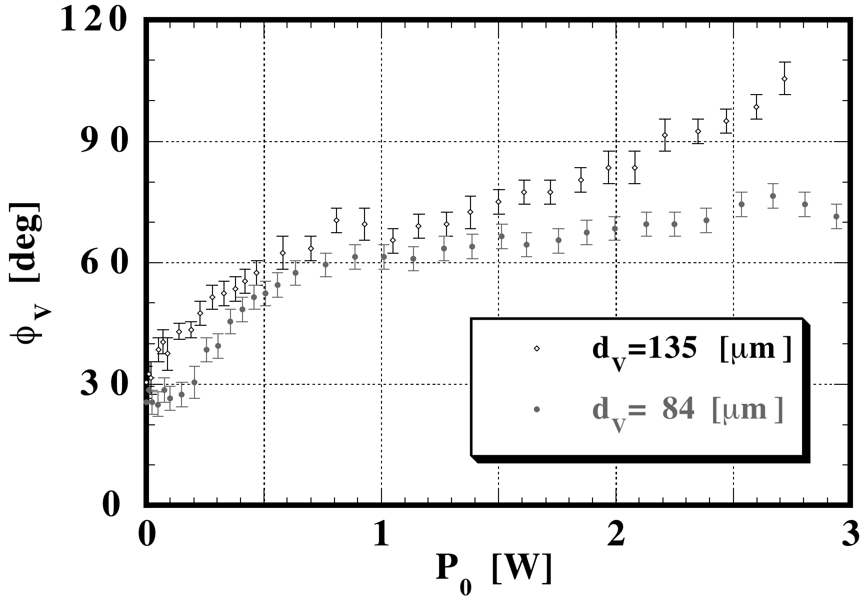

Fig. 5.10: Angular displacement of the vortex pair (measured at the output face of the cell), $\phi_{\rm V}$, plotted vs. incident power, P_0 for two values of initial vortex pair separations $d_{\rm V} = 84 \pm 4\,[\mu{\rm m}]$ and $135 \pm 4\,[\mu{\rm m}]$.

identify their positions.

The power-dependent angular displacement is plotted in Fig. 5.10 for holograms having different vortex separation distances ($d_{\rm V} \ll w_0$ in both cases). As expected, the vortex rotation initially increases as the power increases and then saturates (at $P_0 \approx 0.8\,[{\rm W}]$), once the vortex cores cease to overlap. We attribute this phenomenon to the fluid-like interaction of vortices with shrinking cores. The same characteristic saturated dependence was obtained in numerical simulations for a pair of vortices in ideal Kerr medium, shown in Fig. 5.11. Surprisingly, in our experiment for the case of $d_{\rm V} = 135\,[\mu{\rm m}]$, the saturation gives way to a second regime of rotational enhancement (see Fig. 5.10). We attribute this increase to the complex phase and intensity profile at the center of the beam which occurs at $P_0 > 1[{\rm W}]$ (see the description of high-power

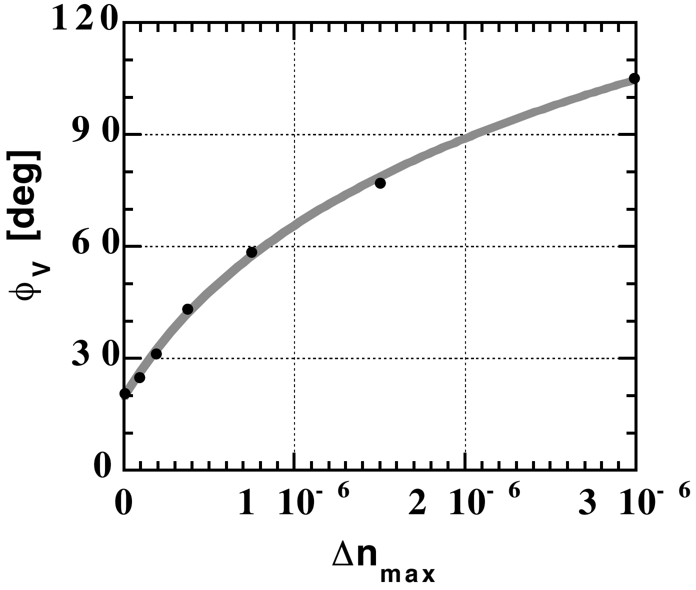

Fig. 5.11: Numerical results for angular displacement of the vortex pair, $\phi_{\rm V}$, plotted vs. the characteristic nonlinear refractive index change. Numerical simulations performed for ideal Kerr media, $d_{\rm V} = 135$ [μm], $w_{\rm V} = 30$ [μm].

regime below). In Fig. 5.12 we show the transverse trajectory of the $d_{\rm V} = 135$ [μm] vortex pair, measured at the output face of the cell.

For $d_{\rm V} = 135\,[\mu\text{m}]$ case the maximum measured angular displacement is $106\pm3°$, which is about 3.5 times greater than the linear angular displacement (30°). We also note that 106° exceeds the 90° Gouy shift[60,61] - a fundamental limit for vortex pair rotation in linear medium. For comparison if a pair of large-core vortices were to propagate in linear media[56,57] over the same distance $(l_c + l_{air})$, one could expect the angular displacement $\phi_{\rm V} \approx 5°$. For the case of $d_{\rm V} = 85\,[\mu\text{m}]$ we observe the maximum angular displacement of $77\pm3°$. At high powers a bright overshooting ring containing the vortex pair is formed at the center of the beam. The central overshooting ring is surrounded by low intensity area and a bright peripheral ring, which contains most of

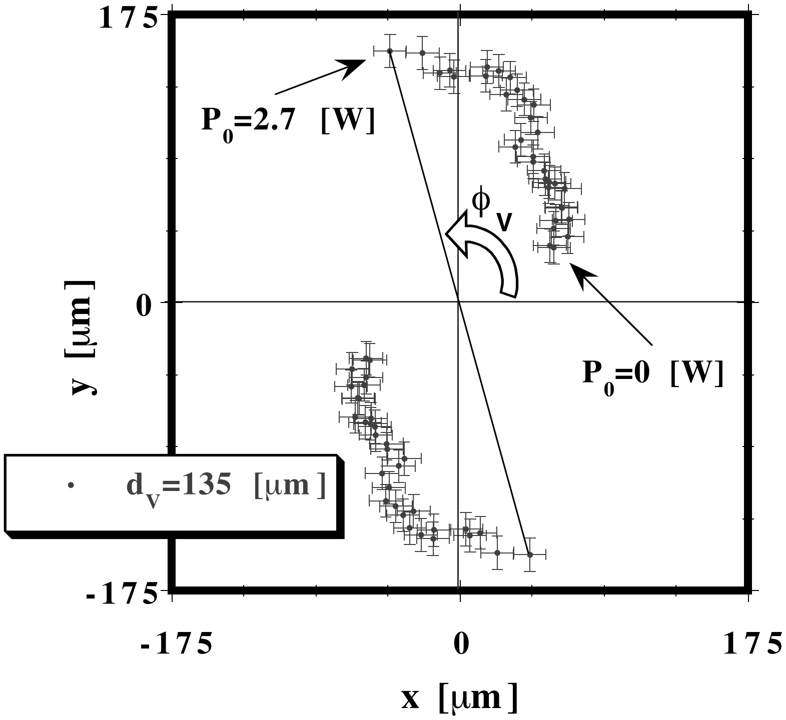

Fig. 5.12: Vortex trajectories at the output face of the cell for the vortex pair with $d_{\text{V}} = 135 \pm 4$ [μm] initial separation.

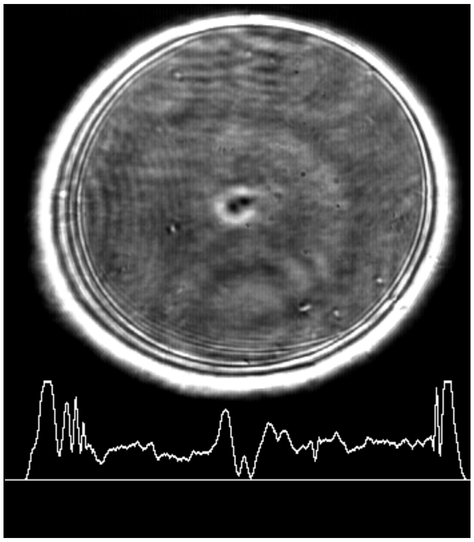

Fig. 5.13: Transverse output intensity profile of a beam with an "overshooting ring" at input power, $P_0 = 0.54\,[\mathrm{W}]$. The line plot intensity is measured along the dashed line going through vortex centers.

the intensity in the beam (see Fig. 5.13). It was impossible to increase significantly the intensity at the center by increasing the power of the input beam, since the nonlinear blooming of the beam directed the light to the outer periphereral ring.

We also investigated transient effects by closing the shutter S_2 for a long time and opening it. The following transient dynamics was observed in nonlinear regime ($P_0 > 0.5\,[\mathrm{W}]$): at the output face of the cell the angular displacement, ϕ_V, initially equal to the linear regime value ($\approx 30^\circ$), increased up to $\approx 90^\circ$ for a characteristic time $t_1 \approx 0.03$ [s] and rapidly decreased into a steady-state value. The entire beam reached the steady-state after a characteristic time of an order of $t_2 \approx 3$ [s].

The rotation of a pair of optical vortices in a weakly absorbing liquid may be affected both by the nonlinearity of the liquid and the fluid-like effective interaction[85, 90] between vortices. The fluid-like phenomenon is exhibited in regimes with

$2w_{\rm V} < d_{\rm V} \ll 2w_0$. It was previously shown in Section 4.4 (see Eq. (4.20)) that this phenomenon results in an initial vortex rotation angular rate

$$\Omega_{\rm V}(z=0) \equiv \Delta\phi_{\rm V}/\Delta z = \lambda/(\pi d_{\rm V}^2), \tag{5.6}$$

where $\Omega_{\rm V}(z=0)$ is the initial angular rotation rate in the transverse plane, $\phi_{\rm V}$ is the angular displacement of the vortex pair and λ is the wavelength. The fluid-like effect may be reduced and completely destroyed by the overlap of the vortex cores. At high intensities the defocusing nonlinearity of the medium may counter the diffraction of vortex cores resulting in sustained fluid-like behavior throughout the medium. On the other hand, heat diffusion may limit the minimum size of the vortex core and introduce transient dynamics into the system. It may also cause higher-order effects, e.g. highly asymmetric vortex core profiles and instability at high powers. Let us first examine the transient effects and then consider the steady-state situation. Consider the experimental setup shown on Fig. 5.8. The instant the power is turned on (before a significant amount of energy is absorbed in the cell) the light propagation regime is linear. Upon propagation the vortex cores will diffract and overlap. Nevertheless, at the output face of the cell we expect some fluid-like rotation due to initially small vortex cores. As the energy is absorbed by the liquid a temperature distribution, $T(r,\theta,z)$, is imposed inside the cell. The temperature dynamics in the liquid can be described by the heat equation:

$$\frac{{\rm d}T}{{\rm d}t} = D\nabla^2 T + \frac{I(r,\theta,z)\alpha}{c_p\rho}. \tag{5.7}$$

where t is time, D is the heat diffusion coefficient, I is the intensity, α is the absorption coefficient, c_p is the heat capacity and ρ is the density of the liquid. Initially, while the temperature is uniform, the heat diffusion term, $\nabla^2 T$, is negligible and the medium behavior is similar to an ideal Kerr medium. As the heat is absorbed, the nonlinearity increases, causing the shrinking of the propagating vortex cores and enhanced fluid-like rotation is exhibited. At this moment the vortex pair rotation angle at the output face of the cell will reach its maximum. Eventually, however, the temperature distribution established across the vortices will give rise to heat diffusion, expanding the vortex cores and, therefore, reducing the fluid-like rotation. We estimate the characteristic time after which the heat diffusion becomes important[108] to be equal to $t_1 \approx w_{\mathrm{V}}^2/4D$, where w_{V} is the size of the vortex at the input face of the cell. After characteristic time $t_2 \approx w_0^2/4D$ we expect the system to reach the steady state. For our system ($D \approx 10^{-7}[m^2/s]$, $w_{\mathrm{V}} \approx 100[\mu\mathrm{m}]$, $w_0 \approx 1000 \approx$) $t_1 \approx 0.025$ [s] and $t_2 \approx 2.5$ [s], which is close to the values observed in the experiment ($t_1^{exp} \approx 0.03$ [s] and $t_2^{exp} \approx 3$ [s]). The size of the vortices and the vortex separation after t_2 will determine how pronounced the hydrodynamic effect is in the steady state. To maximize nonlinear rotation enhancement for a soliton pair the initial separation distance, d_{V}, has to be small enough for the fluid-like behavior to be exhibited. However, if d_{V} is too small the vortex cores may overlap resulting in smaller or non-existent rotation enhancement.

5.4 Conclusions

In Section 5.2 we described an experiment in linear medium which showed a pair of unit-charge vortex filaments rotates at an initial rate that increases inversely with the squared distance of separation. This phenomenon is analogous to the rotation of point vortices in a fluid. Furthermore, the initially large rotation rate, which was two orders of magnitude larger than predicted for conventional optical vortices, was observed to decrease and even reverse sign once the vortex cores overlapped. Control over the initial conditions provided by computer generated holography and high resolution laser printer technology makes the observation of this linear optical effect possible, and opens rich opportunities to explore other topological vortex phenomena such as turbulence and chaos[129] using linear and nonlinear optics as a testing ground. In Section 5.3 we described an experiment in nonlinear media resulting in an enhancement of vortex pair rotation angle of 3.5 times in nonlinear regime (compared to linear). We also observed the net rotation angle exceeding the 90° Gouy shift. This experiment can be viewed as a proof of principle of the possibility of dynamic optical interconnections through the control of waveguides induced in nonlinear medium.

6. OTHER TOPICS IN VORTEX PROPAGATION

6.1 Introduction

This chapter presents two numerical studies of vortex propagation in ideal self-defocusing Kerr media. Section 6.2 describes the propagation of vortices in background fields with periodic modulation. The motion of anisotropic vortices which exhibit torsion effects is explored in Section 6.3. These results presented in this Chapter are preliminary and the research on the aforementioned subjects should be continued. Further studies may reveal the possiblity of controlling vortex motion by periodic background or anisotropy of the vortex itself.

6.2 Periodic Background Influence on Vortex Behavior

The object of this investigation is to explore the means controlling vortex propagation by modulating the background field. We hoped that periodic background fields will, upon propagation, force vortices to move along stable closed orbits in the transverse plane. On the other hand, the symmetry breaking due to the topological defect of the vortex may give rise to chaotic behavior. We chose a plane wave background field with periodic phase modulation along one axis propagating in ideal self-defocusing Kerr media for our numerical experiment.

Consider an initial field of the form given in Eq. (4.1) with a tanh-vortex

(Eq. (4.2)) on a uniform amplitude background with sinusoidal phase modulation along the x-axis:

$$\begin{aligned} G_{BG}(x, y, z = 0) &= A_0 \exp\left[i\Phi_{BG}(x, y, z = 0)\right] \\ \Phi_{BG}(x, y, z = 0) &= \left[1 + \beta \sin(2\pi x/\Lambda)\right]\Phi_0 \end{aligned} \tag{6.1}$$

where G_{BG} is the background field envelope, Φ_{BG} and A_0 are the initial field phase and constant amplitude, respectively, β is the phase modulation factor, Λ is the modulation period in along the x-axis, and Φ_0 is a constant phase factor. To prevent vortex diffraction upon propagation, self-defocusing nonlinear media was modeled. The size of the vortex was matched to the nonlinearity of the media in an attempt to create an optical vortex soliton and, therefore, reduce unnecessary radiation. The vortices were propagated over the Talbot distance,[184] $Z_T = 2\lambda/\Lambda^2$, the distance over which the initial periodic background field would repeat itself in linear media. Split-step propagation method[182] was used to calculate the field for $z > 0$. All the transverse dimensions in this Section are given in arbitrary scaled units, "pixels", equal to the physical distance between two neighboring points on the numerical grid.

To calculate the initial electric field the background field, Eq. (6.1) was multiplied by the vortex amplitude and phase functions. Since the field amplitude did not vanish at the boundaries of the 1024 × 1024 grid, elliptical Jacobi functions[185] were used to generate vortex phase and a quadrupole of vortices was propagated* (see Fig. 6.1 (a) and (d)). The intensity and phase of the vortex can be seen in Fig. 6.1 (b) and (d) (for $z = 0$); as well as in (c) and (d) (for $z = Z_T/2$). The trajectory of a vortex for 3 different values of β and fixed $\Lambda = 256$ [pixels] are plotted in Fig. 6.2.

---

* Elliptical Jacobi functions and quadrupole of vortices (instead of a single vortex) were used to satisfy phase continuity conditions for the split-step propagation method.[182]

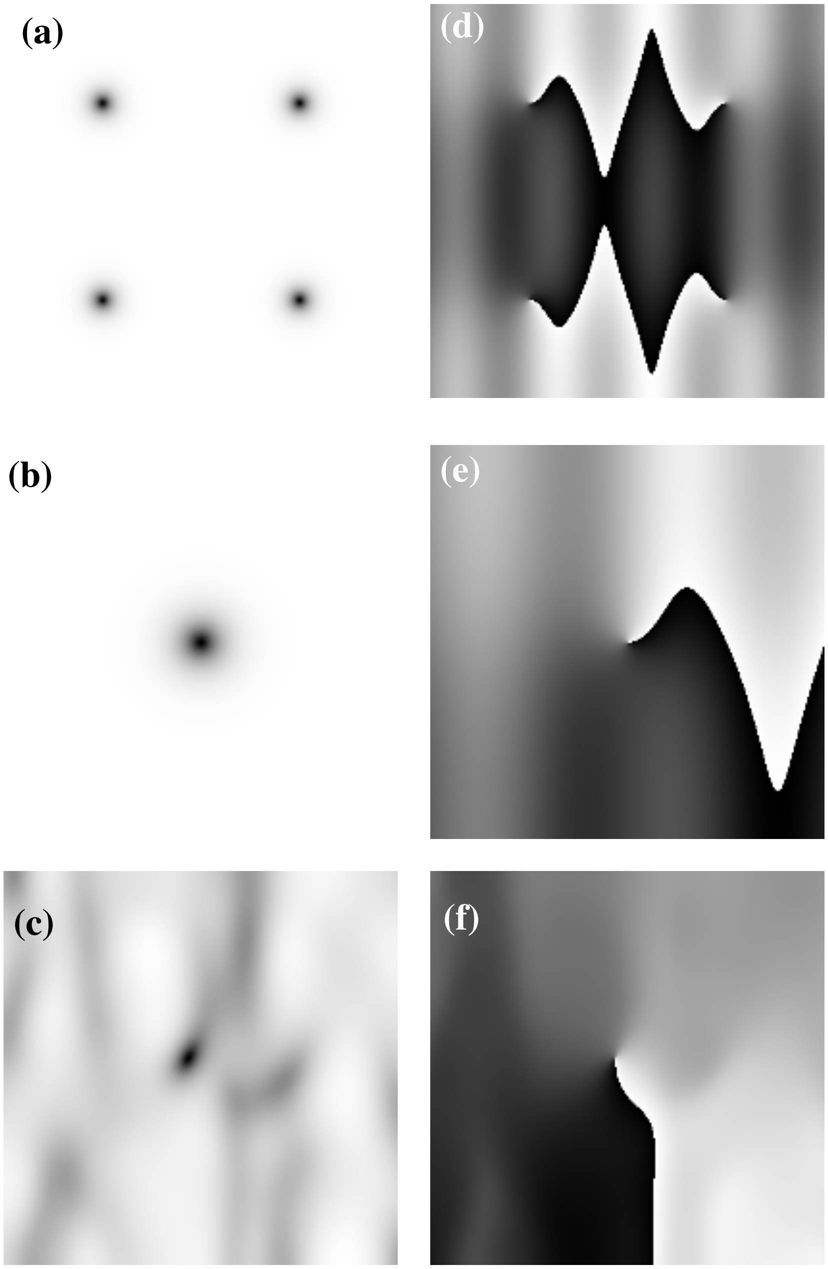

Fig. 6.1: Intensity profiles (a-c) (log scale) and phase profiles (d-f) (linear scale) for vortex propagation in a field with initial sinusoidal phase modulation. (a),(d): $z = 0$, the whole numerical grid is shown. (b),(e): $z = 0$, zoom-in on one vortex (quarter of the grid). (c),(f): same vortex at $z = Z_T/2$.

As expected, a larger value of β bring about a larger vortex orbit. Also, in the case of larger β, we can see loops and sharp changes in direction, which are not present in the case of $\beta = 0.1$. Unfortunately, no stable closed orbits were observed in the system's chaotic behavior.

An interesting phenomena was observed for the case with a smaller modulation period, $\Lambda = 64$ [pixels], and $\beta = 0.25$. Upon propagation, one can observe generation and annihilation of limited edge dislocations and vortex dipoles $(m_1 = 1, m_2 = -1)$ next to the initial vortex. The phase, intensity profiles and real and imaginary zero lines of the field with a dipole are shown in Fig. 6.3. The birth of the dipole may be attributed to an instability owing to the symmetry breaking of the background field.

In conclusion, motion of a vortex in a background field with initial periodic phase modulation was explored using numerical methods. No stable closed orbits were found. Nucleation and annihilation of vortex dipoles was observed. This system should be explored further throughout the (Λ,β,Φ_0) parameter space. Other potentially interesting initial fields should be considered, including backgrounds with periodic amplitude modulation and backgrounds with doubly periodic conditions.

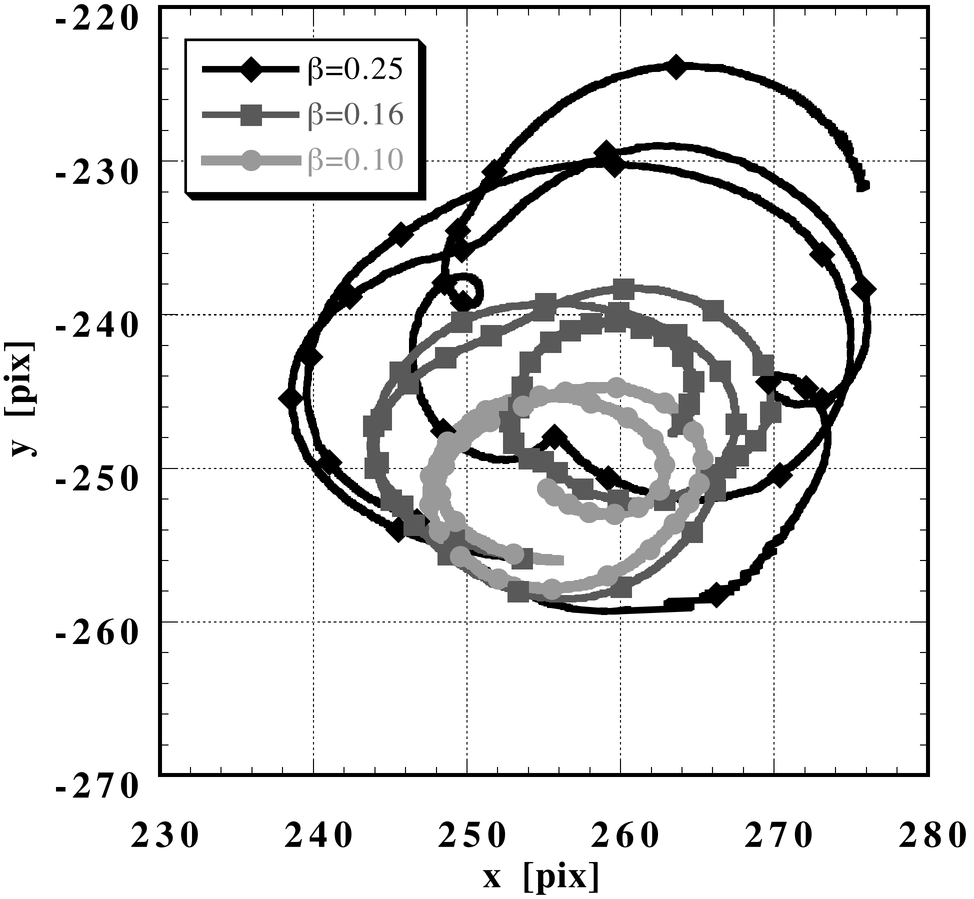

Fig. 6.2: Trajectory of vortex motion in the transverse xy plane for a vortex in a field with initial sinusoidal phase modulation. Phase modulation period $\Lambda = 256$ [pixels]. Grid size 1024×1024. Vortex coordinates are measured from the center of the grid. The initial position of the vortex is $(x_0, y_0) = (256, -256)$ [pixels]. Trajectories are shown for three values of phase modulation, β: 0.1, 0.16, 0.25; $\Phi_0 = \pi$. Propagation distance $z = Z_T$.

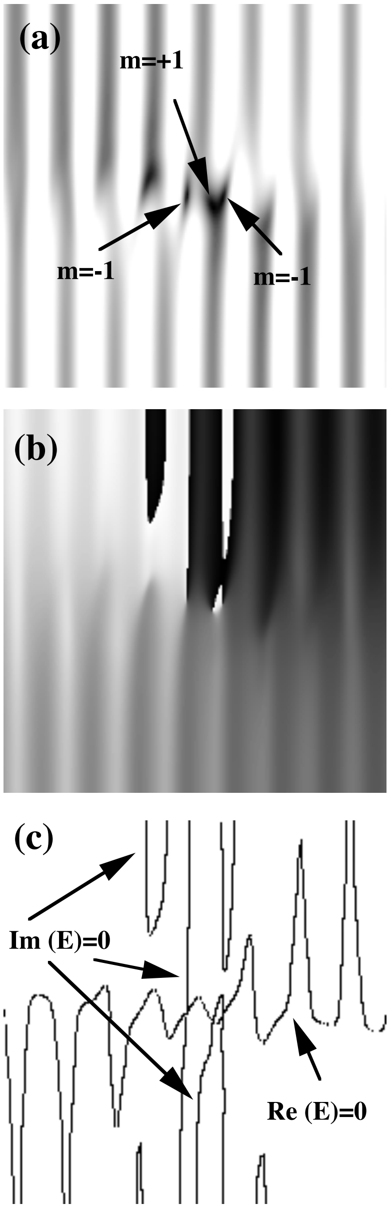

Fig. 6.3: (a) Amplitude (thresholded log gray-scale) profile, (b) phase (linear gray-scale) profile and (c) real and imaginary zero lines of a field with a vortex after propagating a distance $z = 0.063Z_T$. Sinusoidal background phase modulation parameters: $\Lambda = 64$ [pixels], $\beta = 0.25$, $\Phi_0 = \pi$.

6.3 Motion of an anisotropic optical vortex

The purpose of this Section is to investigate the motion of a vortex with an azimuthally varying phase gradient, or 'torsion'. In previous Chapters of this dissertation we assumed that an axis of the vortex is parallel to the optical axis, z, which resulted in azimuthally isotropic phase gradient. On the other hand, a vortex with torsion corresponds to a vortex axis tilted with respect to z-axis. In this Section we will show that torsion (in addition to other parameters like vortex charge, vortex amplitude core function and background field) can affect the propagation of an optical vortex, due to the optical analog of Magnus force. This result shows that the paradigm *"A vortex does not affect its own motion"* which was introduced for vortices without torsion in Sec. 4.4 is not valid for tilted vortices. Magnus effect was investigated for vortices in superconductors and superfluids[186,187] and also in optics[188–190] but not in the context of optical vortices.

We consider an optical vortex with an anisotropic phase gradient.[62] The electric field envelope of such vortex can be written as $E(r, \theta, z) = A(r) \exp[i\Phi(\theta)]$, where

$$\Phi(\theta) = m\theta + \beta \sin(\theta) \tag{6.2}$$

is the phase of the vortex. $A(r)$ is the vortex amplitude core function, m is the integer vortex charge (assumed to be equal to ± 1 in this section). From Eq. (6.2) one can see that the phase is continuos everywhere, except at the center of the singularity ($r = 0$). We will refer to parameter β as torsion. A "conventional" isotropic vortex corresponds to $\beta = 0$. Fig. 6.4 shows the vortex phase for several values of β. Note that for $\beta > 57^\circ = 1$ [rad], the gradient of the phase is reversed for some values of θ. Let us examine the propagation of a torsion vortex, initially located at the center of

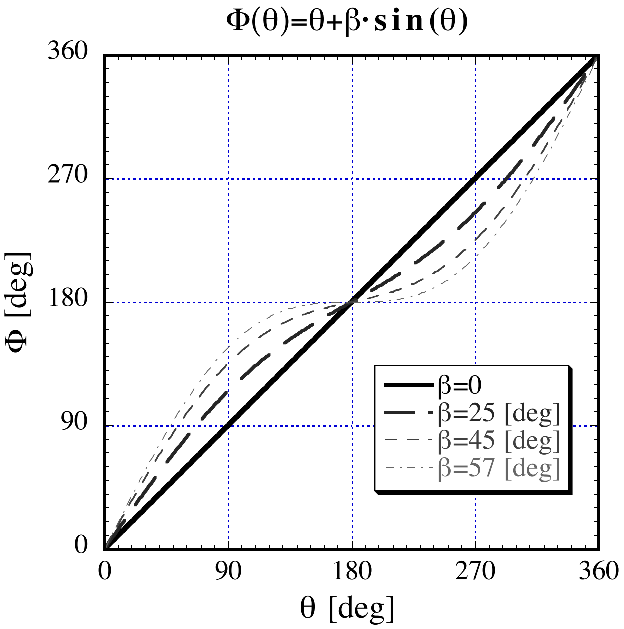

Fig. 6.4: A plot of phase Φ as a function of polar coordinate θ for four different values of torsion, β

a hyper-Gaussian beam. For this case the initial electrical field could be written as

$$E(r, \theta, z = 0) = A(r) \exp\left[-(r/w_0)^{2n_G}\right] \tag{6.3}$$

where the phase is given by Eq. (6.2), n_G is the exponent of the hyper-Gaussian beam ($n_G = 1$ corresponds to a conventional Gaussian), and w_0 is the radial size of the beam.

The motion of an isotropic vortex located in a background field with non-uniform amplitude and phase was examined in Chapter 4. Upon propagation of the beam, the isotropic vortex moves in the transverse plane in the direction antiparallel to the phase gradient and perpendicular to the amplitude gradient of the background field. We will use the same principles in case of a torsion vortex. Namely, we consider a torsion vortex to be an isotropic $A(r) \exp[im\theta]$ vortex located on a Gaussian beam background with an additional anisotropic phase factor, $\exp[i\beta\cos(\theta)]$. This phase factor introduces an effective background phase gradient, $\vec{\mathbf{k}}_\beta = -\hat{\theta}\beta\cos(\theta)/r$ where $\hat{\theta}$ is the azimuthal unit vector. Thus, we have an isotropic vortex and a background field with wavevector, $\vec{\mathbf{k}}_{beta}$ (see Fig. 6.4 (a)), resulting in vortex motion in the direction

$$\vec{\mathbf{k}}_{ph} = -\mathrm{Sgn}(\beta)\hat{\mathbf{y}}, \tag{6.4}$$

where $\mathrm{Sgn}(\beta) = \beta/|\beta|$ and $\hat{\mathbf{y}}$ is the unit vector along the y-axis. In addition, the light moving along $\vec{\mathbf{k}}_{ph}$ will create an amplitude gradient $\vec{\nabla}(A_{BG})$ parallel to $\vec{\mathbf{k}}_{ph}$ (Fig. 6.5 (b)). We use Eq. (4.14) to find the direction of motion of the vortex owing to amplitude gradient as the beam propagates in $\vec{\mathbf{k}} = \hat{\mathbf{z}}$ direction (see Fig. 6.5 (b)):

$$\vec{\mathbf{k}}_{amp} = \mathrm{Sgn}(m)\left[\vec{\mathbf{k}} \times \vec{\nabla}(A_{BG})\right] = -\mathrm{Sgn}(m)\mathrm{Sgn}(\beta)[\hat{\mathbf{z}} \times \hat{\mathbf{y}}] = \mathrm{Sgn}(m\beta)\hat{\mathbf{x}}. \tag{6.5}$$

We combine the vortex motion due to amplitude and phase gradients, $\vec{\mathbf{k}}_{amp}$ and $\vec{\mathbf{k}}_{ph}$, respectively to obtain a resultant vortex displacement in the direction shown in Fig. 6.5 (c). This phenomenon may be characterized as an optical analog of the mechanical Magnus effect on a spinning sphere moving in the air with $\vec{\mathbf{k}}_\beta$ and $-\vec{\nabla}(m\theta) = -\hat{\theta}/r$ corresponding to corresponding to center of mass velocity, $\vec{v}$, and spin velocity, $\vec{v}_{spin}$, respectively.

We have modeled numerically the propagation of a torsion vortex in nonlinear self-defocusing media for different values of initial parameters m and β. On Fig. 6.6 one can see the transverse phase and amplitude profiles for the case $m = 1$ and $\beta = 40°$. Initially the vortex is located at the center of the hyper-Gaussian beam ($n_G = 2$). As the beam propagates the vortex will move off the center in the com-

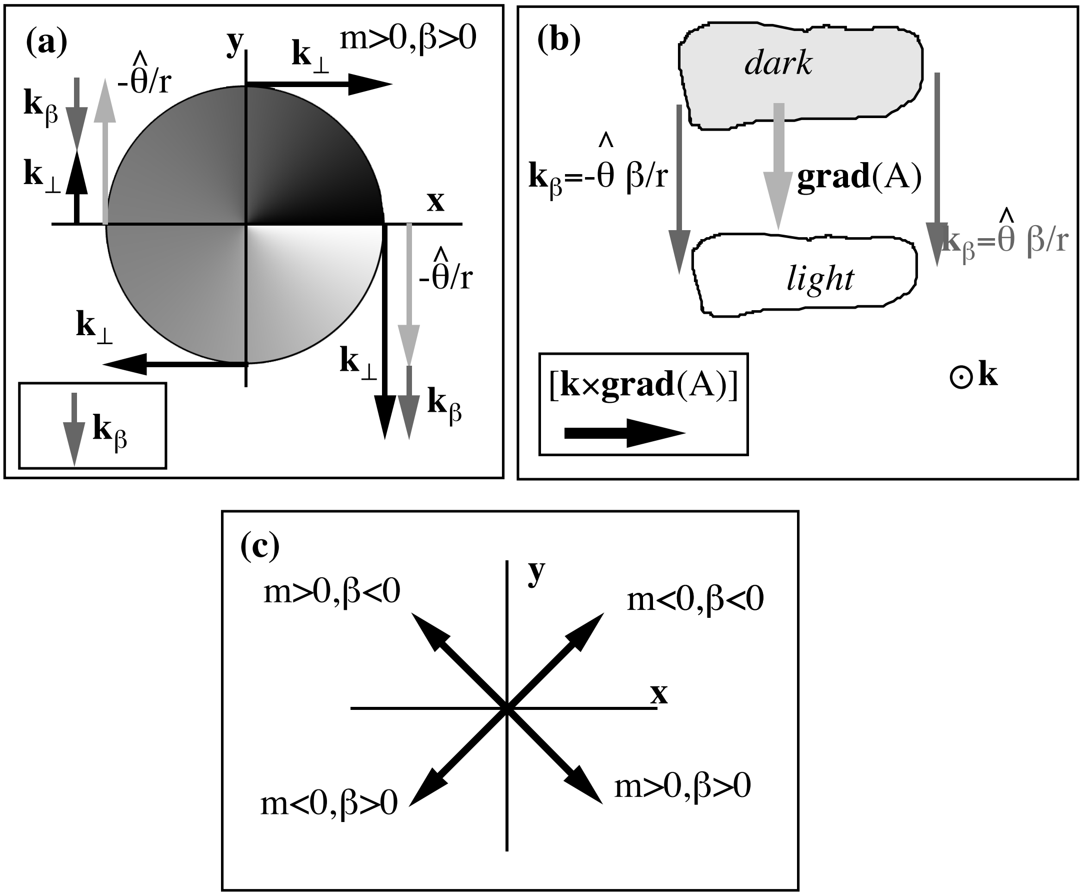

Fig. 6.5: Torsion vortex motion due to (a) phase and (b) amplitude gradients. The values of $m > 0$ and $\beta > 0$ were assumed for (a) and (b). The resultant direction of motion is shown in (c) for all possible signs of m and β.

bined direction predicted by Eqs. (6.4) and (6.5) and shown in Fig. 6.5 (c)[†]. Note the asymmetric amplitude profile in the propagated field. However, after a certain distance of propagation the torsion in the vortex disappears due to diffraction and the vortex becomes approximately isotropic. We note, however, that without initial torsion the vortex would never move off the axis of the beam.

The plot on Fig. 6.7 shows how the vortex moves off the center for different values of torsion parameter, β. One can see two distinct propagation regimes. Namely, initially the vortex is moving fast, with the slope of $r(z)$ graph proportional to β. Upon propagation the torsion is reduced due to diffraction, resulting in the in much slower vortex drift away from the center owing to the influence of the background beam on the off-axis vortex.

In conclusion, this preliminary study predicted and numerically observed behavior of vortices with torsion which is not exhibited by "conventional" isotropic vortices. This behavior is attributed to the analog of the Magnus effect. Further research may lead to a better understanding of self-action of anisotropic vortices and additional means of controlling vortex motion.

[†] This motion was also observed in the case of linear media.

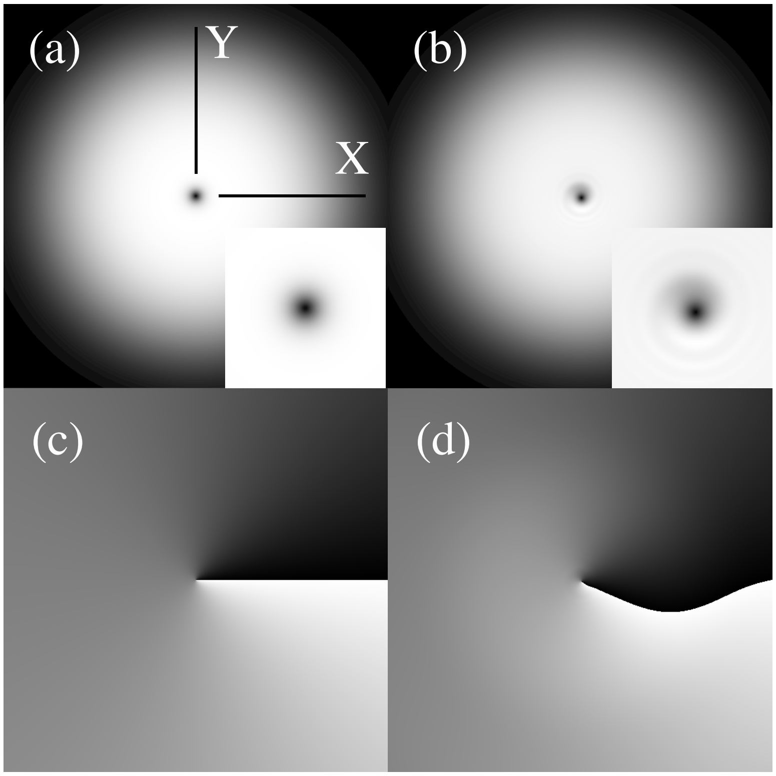

Fig. 6.6: Intensity (a-b) and phase (c-d) profiles of a propagating torsion vortex. (a) and (c) show the initial field ($z = 0$), while (b) and (d) show the near-field profiles. $\beta = 40°$.

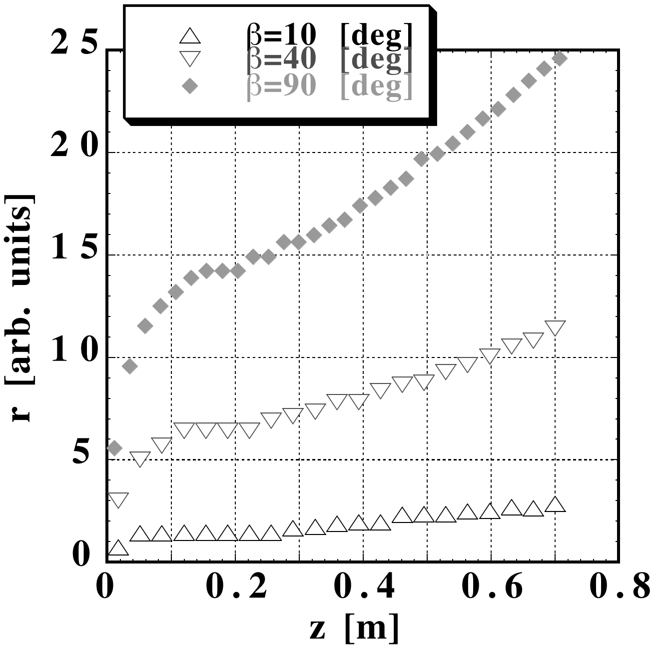

Fig. 6.7: Propagation dynamics of a radial displacement from the initial position (center of the beam) for a torsion vortex plotted for several values of β. Numerical simulation performed for the case of self-defocusing Kerr medium.

APPENDIX

A. VORTICES IN A 2-DIMENSIONAL FLUID FLOW

The purpose of this Appendix is to give a brief overview of the motion of vortex filaments in an inviscid incompressible fluid, mainly for those of the readers who are more familiar with optics than fluid dynamics. The discussion mostly follows classic hydrodynamics texts by Milne-Thomson[87] and McLeod.[183]

Complex Potential

Let us consider a case of 2-D incompressible inviscid fluid. We can confine ourselves to a 2-dimensional flow model if the velocity field of the fluid is a function of only two variables. If the flow pattern is the same in every plane perpendicular to a certain axis, it is called a *plane flow.* It is convenient to describe points and vectors in the plane in terms of complex numbers. Any point with Cartesian coordinates (x, y) can be characterized by a complex number $z = x + iy$. Similarly, any vector of the form $\vec{A} = a\hat{x} + b\hat{y}$ could be expressed as $\vec{A} = a + bi$ (here, $\hat{x}$ and $\hat{y}$ are, of course, unit vectors in along x and y axes, respectively). For a 2-D velocity field $\vec{v}(x, y) = v_x\hat{x} + v_y\hat{y}$ one can define a function $\psi(x, y)$, such that

$$v_x = -\frac{\partial\psi}{\partial y}, \quad v_y = \frac{\partial\psi}{\partial x}. \tag{A.1}$$

$\psi(x, y)$ is called the *stream function.* Eq. (A.1) requires $\div(\vec{v}) = 0$ and which can be shown to valid for an incompressible fluid (by using the continuity equation). We define a $\varphi(x, y)$, called *velocity potential* and require that $\varphi + i\psi$ is analytical. For this condition to be true $\psi(x,y)$ and $\varphi(x,y)$ have to satisfy the Cauchy-Riemann equations:

$$\frac{\partial\varphi}{\partial x} = \frac{\partial\psi}{\partial y}, \quad \frac{\partial\varphi}{\partial y} = -\frac{\partial\psi}{\partial x}. \tag{A.2}$$

From (A.1) and (A.2) one can obtain the relation between $\varphi(x,y)$ and the velocity field components:

$$v_x = -\frac{\partial\varphi}{\partial x}, \quad v_y = -\frac{\partial\varphi}{\partial y}. \tag{A.3}$$

We can now define an analytical function W, called *complex velocity potential*,

$$W = \varphi + i\psi. \tag{A.4}$$

By the nature of its definition, W has a very useful derivative with respect to complex coordinate z.

$$\frac{dW}{dz} = \frac{\partial\varphi}{\partial x} + i\frac{\partial\psi}{\partial x} = \frac{\partial\varphi}{\partial x} - i\frac{\partial\varphi}{\partial y}. \tag{A.5}$$

We can see that the negative complex conjugate of this derivative will be equal to the velocity field:

$$-\left(\frac{dW}{dz}\right)^{\star} = -\frac{\partial\varphi}{\partial x} - i\frac{\partial\varphi}{\partial y} = v_x + iv_y. \tag{A.6}$$

Let us consider a case of a vortex in a 2-D incompressible inviscid fluid. It is convenient to introduce a *vorticity* vector $\vec{w}$, such that

$$\vec{w} = \vec{\nabla}\times\vec{v}. \tag{A.7}$$

It can be shown (see Ref. 183, p. 60) that for the case of incompressible fluid $\mathrm{d}(\vec{w})/\mathrm{d}t = (\vec{w}\cdot\vec{\nabla})\vec{v}$. Let x_3 be the axis perpendicular to the plane of the flow, then the equation can be re-written as

$$\frac{d}{dt}(\vec{w}) = |\vec{w}|\frac{\partial \vec{v}}{\partial x_3}, \tag{A.8}$$

and since in a 2-D flow velocity $\vec{v} = \vec{v}(x_1, x_2)$ is independent of the third perpendicular coordinate, $(\partial\vec{v}/\partial x_3) = 0$. Therefore, $(\mathrm{d}\vec{w}/\mathrm{d}t) = 0$. *In the plane 2-D motion of an incompressible fluid vorticity is conserved.*

Cylindrical Vortex

The simplest case of a 2-D vortex is a cylindrical vortex. Imagine a region in a cylindrical tube of radius $r = a$ having a constant vorticity w. Let the fluid outside the region have zero vorticity, and let the flow pattern be symmetrical around the origin of the vortex. The polar velocity components v_r and v_θ will be both constant along any circle surrounding the origin. In the case of no sources or sinks the rate of flow in the radial direction through a circle of a fixed radius is equal to zero, and, therefore, v_r=0. From Stoke's circulation theorem, the flux of vorticity through a part of vortex tube enclosed a radius $r < a$ should be equal to the circulation of the velocity field around the circle of that radius. The flux is the product of the vorticity with the area of that part $\pi r^2 w$. Circulation is

$$\Gamma = \oint_0^{2\pi} v_\theta r \, d\theta = 2\pi v_\theta r. \tag{A.9}$$

Thus, for any $r < a$ (i.e., inside the vortex) we get $2\pi v_\theta r = \pi r^2 w$, or

$$v_\theta = \frac{rw}{2}. \tag{A.10}$$

In other words, inside the vortex the fluid is rotating at a constant angular velocity $\Omega = w/2$. At the center of the vortex $(r = 0)$ we have $v_\theta = 0$. This is a very important result. The velocity field of a vortex or *induced velocity* is equal to zero. If a vortex is superimposed on some flow, the center of the vortex will move with the same velocity of the original flow. The vortex does not induce any motion onto itself.

Outside of the vortex ($r > a$), the circulation along a circle of radius r will be equal to the total flux of vorticity produced by the vortex $\pi a^2 w$. Therefore, $2\pi v_\theta r = \pi a^2 w$ and

$$v_\theta = \frac{a^2 w}{2r}. \tag{A.11}$$

From equations (A.10), (A.11) one can see that v_θ is continuous on the boundary of the vortex ($r = a$).

Outside of the vortex, at an arbitrary point $z = r\exp(i\theta)$ the velocity will be $v = iv_\theta \exp(i\theta) = v_\theta \exp[i(\theta + \pi/2)]$. Then, the derivative of the complex potential must be

$$\frac{dW}{dz} = -v^\star = -(-i)v_\theta \exp(-i\theta) = i\frac{a^2 w}{2r}\frac{1}{\exp(i\theta)} = i\frac{a^2 w}{2z} = i\frac{\kappa}{z}, \tag{A.12}$$

where $\kappa \equiv a^2 w/2 = \Gamma_{vortex}/(2\pi)$ is the *strength of the vortex* and Γ_{vortex} is the circulation of the velocity field along the boundary of the vortex. The strength of a vortex in a fluid, κ, is equivalent to the topological charge of an optical vortex, m, except for the fact that the latter is quantized. Namely, while κ can, in principle, be any real number, m is by definition a signed integer, owing to the topological nature of an optical vortex. We can now integrate equation (A.12) to obtain

$$W = i\kappa \ln z. \tag{A.13}$$

This complex velocity potential corresponds to a vortex located at the origin. For a vortex located at point $z = Z_0$ we have

$$W = i\kappa \ln(z - Z_0). \tag{A.14}$$

Point Vortices (Vortex Filaments)

Suppose that we have a cylindrical vortex at $z = Z_0$ with its radius a shrinking to zero in such a way that its strength, κ remains constant. This vortex has a vanishing size. It is called the *point vortex*. Since vortex strength is finite the fluid velocity would approach infinity in the vicinity of the center. We shall assume, that the induced velocity of a vortex filament is equal to zero at $z = Z_0$. Thus, at any point outside the vortex (which means anywhere except $z = Z_0$) the complex velocity potential can be defined as

$$W = i\kappa \ln(z - Z_0). \tag{A.15}$$

Let us examine a case of two vortices of strengths κ_1 and κ_2 at points $z = z_1$ and $z = z_2$. The complex velocity potential will be

$$W = i(\kappa_1 \ln(z - z_1) + \kappa_2 \ln(z - z_2)). \tag{A.16}$$

At any moment of time the velocity of each vortex will depend on the position of the other one. We can write down the differential equations for the positions of each of the vortices:

$$\begin{cases} \dfrac{\mathrm{d}z_2}{\mathrm{d}t} = \left(-\dfrac{\mathrm{d}W}{\mathrm{d}z}\right)^{\star}_{z=z_2} = \left(\dfrac{-i\kappa_1}{z_2 - z_1}\right)^{\star} = \dfrac{i\kappa_1}{z_2^{\star} - z_1^{\star}}, \\[2ex] \dfrac{dz_1}{dt} = \left(-\dfrac{dW}{dz}\right)^{\star}_{z=z_1} = \ldots = \dfrac{i\kappa_2}{z_1^{\star} - z_2^{\star}}. \end{cases} \tag{A.17}$$

If we multiply the first and the second equation in the system (A.17) by $\kappa_2/(\kappa_1+\kappa_2)$ and $\kappa_1/(\kappa_1+\kappa_2)$, respectively, and add the equations, we will obtain

$$\frac{d}{dt}\left(\frac{z_1\kappa_1+z_2\kappa_2}{\kappa_1+\kappa_2}\right)=0. \tag{A.18}$$

The quantity $(z_1\kappa_1+z_2\kappa_2)/(\kappa_1+\kappa_2)$ is invariant in time. It is called the *centroid of vortices.* To examine the dynamics of this 2-vortex system, let us make a coordinate transformation that will put the centroid of vortices into the origin. Then, in our new frame of reference, the vortices will be at points $\xi_1=r_1\exp(i\theta)$ and $\xi_2=-r_2\exp(i\theta)$, with the radii r_1 and r_2 related in the following way: $r_1\kappa_1=r_2\kappa_2$. Our equations will still look as in (A.17) with ξ_1,ξ_2 replacing z_1,z_2. We notice that

$$\frac{1}{\xi_1^\star-\xi_2^\star}=\frac{1}{d_{\mathrm{V}}\exp(-i\theta)}=\frac{\exp(i\theta)}{d_{\mathrm{V}}}, \tag{A.19}$$

where d_{V} is the distance between the vortices: $d_{\mathrm{V}}=r_1+r_2$. The system of complex equations (A.17) now reduces down to a single complex equation since there are only two independent variables in the problem - one of the radii and the angle θ.

$$\frac{d\left(r_1\exp(i\theta)\right)}{dt}=\frac{i\kappa_2}{d_{\mathrm{V}}}\exp(i\theta) \tag{A.20}$$

Let us do the differentiation, cancel out the exponential phase term and equate the imaginary and real parts in the last equation. We get

$$\frac{dr_1}{dt}=0, \qquad \& \qquad ir_1\frac{d\theta}{dt}=i\frac{\kappa_2}{d_{\mathrm{V}}}. \tag{A.21}$$

Thus, $\theta=\kappa_2 t/(d_{\mathrm{V}}r_1)$. Also, $r_1=\text{const}$, and, therefore, $r_2=const$. We obtained that the distance between vortices will not change. Also, from $r_1\kappa_1=r_2\kappa_2$ and $r_1+r_2=d_{\mathrm{V}}$ we can get a better-looking expression for the angular velocity:

$$\Omega=\frac{\kappa_1+\kappa_2}{d_{\mathrm{V}}^2}. \tag{A.22}$$

Thus, the vortices remain at the initial distance from each other and they both rotate around the centroid with the angular velocity Ω.

B. MODELING LIGHT PROPAGATION NUMERICALLY

This Appendix describes the "Split-Step" or "Beam Propagation" method we used to model the propagation of light in nonlinear media. This numerical algorithm was first introduced by Feit and Fleck[182] in 1978 to simulate light propagation in optical fibers with graded refractive index.

The split-step method is an extension of a classic paraxial linear propagation algorithm which was known earlier.[178] We will first describe the linear algorithm.

Given the initial monochromatic scalar electric field envelope, $u(x, y, z = 0)$ we would like to "propagate" it in linear medium along the optical axis, z to obtain the field at arbitrary $z > 0$, $u(x, y, z)$. The initial field envelope may be written as

$$u(x, y, z = 0) = A(x, y, z = 0) \exp\left[i\Phi(x, y, z = 0)\right], \tag{B.1}$$

where $A(x, y, z = 0)$ and $\Phi(x, y, z = 0)$ are the amplitude and the phase of the initial field, respectively. To obtain the propagated field one can use the paraxial transfer function,[178] $H(z)$:

$$u(x, y, z) = \mathcal{FT}^{-1}\left\{H(z)\mathcal{FT}^{-1}\left\{u(x, y, z = 0)\right\}\right\}, \tag{B.2}$$

where

$$H(z) = \exp\left[i\pi\lambda z\left(f_x^2 + f_y^2\right)\right] \tag{B.3}$$

is the transfer function, λ is the wavelength of light, f_x and f_y are the spatial frequencies in the Fourier domain along x and y axes, respectively. The forward and inverse Fourier transforms are given by

$$\mathcal{FT}\{g(x,y)\} = \int_{-\infty}^{\infty}\int_{-\infty}^{\infty} \mathrm{d}x\mathrm{d}y \left\{g(x,y)\exp\left[-2\pi(f_x x + f_y y)\right]\right\} \tag{B.4}$$

and

$$\mathcal{FT}^{-1}\{G(f_x,f_y)\} = \int_{-\infty}^{\infty}\int_{-\infty}^{\infty} \mathrm{d}f_x\mathrm{d}f_y \left\{G(f_x,f_y)\exp\left[2\pi(f_x x + f_y y)\right]\right\}, \tag{B.5}$$

respectively. This analytical method lends itself easily to numerical implementation. The continuous electric field in the transverse xy plane is represented by a discrete 2-dimensional array (grid) of complex numbers of size $N \times N$. At each grid point (n_x, n_y) we specify the real and imaginary parts of the field, normalized to the characteristic amplitude, u_0: $u'_{\mathrm{RE}} \equiv \Re\{u/u_0\}$ and $u'_{\mathrm{IM}} \equiv \Im\{u/u_0\}$. The scaled intensity and the phase of the field at each point can be reconstructed from u'_{RE} and u'_{IM}: $I/I_0 = (u'_{\mathrm{RE}})^2 + (u'_{\mathrm{IM}})^2$ and $\Phi = \arctan(u'_{\mathrm{IM}}/u'_{\mathrm{RE}})$. To propagate the field numerically along the optical axis, z, we apply Eq. B.2 to the normalized field $u'(x,y,z)$, using a Fast Fourier Transform (FFT) algorithm.[191] FFT is a generic name applied to any Discrete Fourier Transform (DFT) method providing a better performance than the brute-force algorithm, which requires a factor of $O(N^2)$ operations for each dimension of size N. The FFT algorithms used in most of the current signal processing software have the $O(N\log_2 N)$ performance (for each dimension) and are optimized for grid size which is an integer power of 2 ($N = 2^j$, where j is an integer). FFT algorithms were popularized by Cooley and Tukey[192] in 1965, although a number of algorithms were independently discovered earlier by various researchers, including Gauss in 1805 (see Ref. 193 for the overview of the literature). For example, a widely-used Danielson-Lanczos algorithm[194] was published in 1942.

The algorithm implementing linear propagation given by Eq. (B.2) may be presented as follows:

1. Take a FFT of the initial field array.
2. Multiply each element of the array by the corresponding element of the transfer matrix H.
3. Take an inverse Fourier transform of the field obtained in the previous step.

Since the aforementioned linear algorithm uses Fourier transform, it implicitly assumes that the initial field $u'(x, y, z = 0)$ is doubly periodic in x and y, i.e. that the rectangular sampling window repeats itself infinitely throughout the transverse plane (see Fig. B.1). The periods in x and y directions are equal to the physical size of the sampling window, L_x and L_y:

$$u'(x, y, 0) = u(x + L_x p, y + L_y q, 0), \tag{B.6}$$

where p, q are arbitrary integers. We will assume a square sampling window ($L_x = L_y = L$) for simplicity. This implied periodicity gives rise to several interesting features. The first one is the Talbot distance, Z_T. It is a minimal distance after which the propagated field $u(x, y, Z_T)$ is equal to the periodic initial field $u(x, y, z = 0)$.[195, 196] We break down the propagation function in Eq. (B.3) into f_x- and f_y-dependent parts:

$$H(z) = \exp\left[i\pi\lambda z f_x^2\right] \cdot \exp\left[i\pi\lambda z f_y^2\right]. \tag{B.7}$$

It is clear from Eq. (B.2) that the propagated field will be equal to the initial periodic field when $H(z) = 1$. This will occur when both phase factors in Eq. (B.7) are equal an integer factor of 2π. For the x-axis term we obtain: $\pi\lambda z f_x^2 = 2\pi j$, therefore

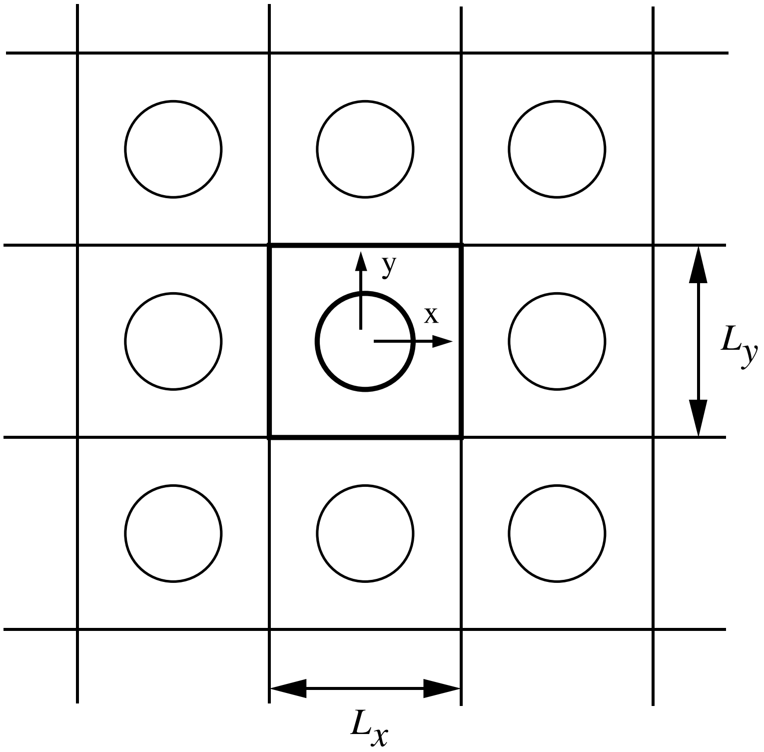

Fig. B.1: Doubly periodic FFT window. The "main" window in the center is the numerical grid which we use to propagate initial beam. In this case, a finite beam is depicted by a circle. The numerical algorithm using FFT's assumes a doubly periodic field - the initial field in the "main" window is infinitely repeated in x and y directions.

$z = 2j/(\lambda f_x^2)$, where j is an arbitrary integer. Now, Talbot distance is equal to the smallest z which results in $H(z) = 1$, thus we substitute the smallest index $j = 1$ and the largest spatial frequency $f_x = 1/L_x = 1/L$ to find

$$z_T = \frac{2L^2}{\lambda}. \tag{B.8}$$

The same result is obtained for the y-direction.

The periodic nature of FFT also gives rise to aliasing artifacts. These problems may arise in the numerical propagation of both finite-size and plane wave beams. In the former case, one has to make sure that the finite beam vanishes at the edges of the

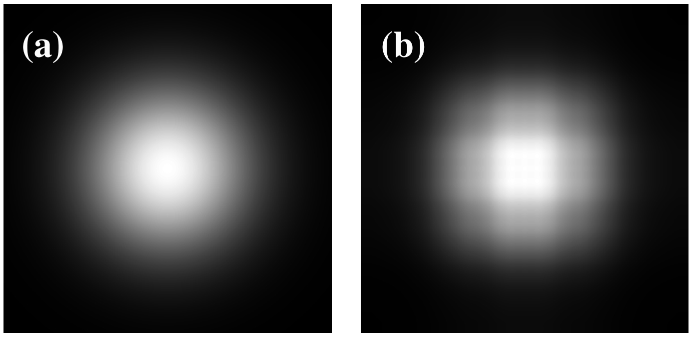

Fig. B.2: Effects of aliasing on the intensity profile of a finite-size Gaussian beam. (a) Initial beam which has non-vanishing intensity at the boundaries of the FFT window. (b) Initial beam after propagating a distance $Z_0/12$. The intensity profiles are rendered using exponential gray-scale which emphasizes artifacts due to aliasing.

numerical grid, so there is no aliasing between the "main" beam we are propagating and its mirror images in the periodic space. In Fig. B.2 we show the aliasing effects in the case of Gaussian beam propagation. The cross-like pattern is visible in the propagated field profile. One of the ways to avoid aliasing for finite-size beam is to ensure that the FFT window is large enough (compared to the beam size) to provide for zero intensity at the boundary of the window. This may be achieved through a procedure called "zero-padding". It consists of increasing the size of the numerical grid by adding additional points with zero intensity around the initial beam.

The size of the finite-size beam with respect to the size of the numerical grid may be also important from the sampling point of view. The larger the size of the beam with respect to the FFT window size, the smaller the image of the beam in the Fourier space is. This may result in inadequate representation of the spatial frequencies in the beam. Let us derive the relation between the size of the Gaussian beam in the real space and in Fourier domain. Gaussian beam in real space may be written as

$E_0 \exp(-r^2/w_0^2)$, and its Fourier transform as $E_0 w_0^2 \exp(-\pi^2 w_0^2 \rho^2)$, where ρ is the radial polar coordinate in Fourier space. The size of the Gaussian beam in real and Fourier spaces is w_0 and $1/\pi w_0$, respectively. For a $N \times N$ grid representing physical area of $L \times L$ in real space the size of a grid pixel is L/N, while in Fourier space the size of a grid pixel is $1/L$. Thus the size of the Gaussian beam, *measured in grid pixels* is $w_0 N/L$ and $L/\pi w_0$ in real and Fourier space, respectively. To have equal sampling in real and Fourier space one should set $w_0 N/L = L/\pi w_0$ which requires the size of a Gaussian in pixels to be $\sqrt{N/\pi}$ for both real and Fourier spaces. For example, for a 1024×1024 window the size of the Gaussian should about $\sqrt{1024/\pi} \approx 18$ pixels. In practice, however, resolution in Fourier space in sacrificed for resolution in real space by generating beams of sizes greater than $\sqrt{N/\pi}$ pixels.

Let us now describe the nonlinear algorithm. We follow the procedure given in Newell and Moloney in Ref.[197] The algorithm is designed to solve the Nonlinear Schrödinger (NLS) equation (see Eq. (4.7)), which, after normalization, maybe written as

$$i\frac{\partial u'}{\partial z} = \mathcal{L}u' + \mathcal{N}(z)u', \tag{B.9}$$

where $u' = u'(x, y, z)$ is the normalized field, the coordinates x and y are normalized by w_{NL} and z is normalized by z_{NL}*, $\mathcal{L}$ is a linear operator ($\nabla_\perp^2$ in case of NLS) and $\mathcal{N}(z)$ is a nonlinear operator which depends on u' (in case of ideal Kerr medium it is equal to a phase correction proportional to $n_2|u'|^2$).

To obtain the field u' after propagation over a small distance Δz we can formally

---

* These nonlinear scaling factors are described in Chapter 4

integrate Eq. (B.9):

$$u'(x,y,\Delta z) = \exp\left[-i\left(\mathcal{L}\Delta z + \int\limits_0^{\Delta z} \mathrm{d}\tau \mathcal{N}(\tau)\right)\right] u'(x,y,0) \tag{B.10}$$

In general the formal operator expression given by Eq. (B.10) is hard to evaluate, since operators $\mathcal{L}$ and $\mathcal{N}$ do not commute. We can approximate this expression as

$$u'(x,y,\Delta z) = \exp\left[-i\mathcal{L}\Delta z/2\right] \exp\left[-i\int\limits_0^{\Delta z} \mathrm{d}\tau \mathcal{N}(\tau)\right] \exp\left[-i\mathcal{L}\Delta z/2\right] u'(x,y,0). \tag{B.11}$$

The Eq. (B.11) can be shown to approximate the operator in Eq. (B.10) with an error of $O((\Delta z)^2)$. Since $\mathcal{N} = \mathcal{N}(|u'|^2)$ for Kerr medium we can take $\mathcal{N}$ outside of the integral to obtain $-i\mathcal{N}(|u'(x,y,0)|^2)\Delta z$ as an argument of the second exponential function in Eq. (B.11). On the other hand, $\mathcal{L}$ is just $\nabla_\perp^2$, $\exp[-i\mathcal{L}\Delta z/2]$ corresponds to multiplication in Fourier space by linear transfer function $H(\Delta z/2)$ as described in Eqs. (B.2) and (B.3). The complete algorithm may be written as

$$\begin{aligned} u'(x,y,\Delta z) =& \mathrm{FFT}^{-1}[H(\Delta z/2) \times \\ & \mathrm{FFT}\{\exp(i\mathcal{N}(u'|x,y,0|^2)\Delta z)\mathrm{FFT}^{-1}[H(\Delta z/2)\mathrm{FFT}\left(u'(x,y,0)\right)]\}]. \end{aligned} \tag{B.12}$$

To propagate a field over distance Z using steps of size Δz we will go through the following steps:

1. Propagate the initial field half a step in linear medium - over distance $\Delta z/2$:
   (a) Apply a Fourier transform to the field.
   (b) Multiply by transfer function $H(\Delta z/2)$.
   (c) Apply an inverse Fourier transform to the field.

2. Multiply by the nonlinear correction factor $\exp[-\mathcal{N}(|u'|^2)\Delta z]$.
3. Propagate the field full step in linear medium:
    (a) Apply a Fourier transform to the field.
    (b) Multiply by transfer function $H(\Delta z)$.
    (c) Apply an inverse Fourier transform to the field.
4. Go back to Step 2 until propagation distance is $z = Z - \Delta z/2$.
5. Propagate the field half a step in linear medium:
    (a) Apply a Fourier transform to the field.
    (b) Multiply by transfer function $H(\Delta z/2)$.
    (c) Apply an inverse Fourier transform to the field.

The size of the algorithm step, Δz, has to be adjusted so that the nonlinear phase correction is relatively small $N(|u'|^2)\Delta z/2\pi \ll 1$.

C. SIGN CONVENTIONS IN PARAXIAL BEAM PROPAGATION

The purpose of this appendix is to establish the sign conventions to use in calculations of paraxial beam propagation. The signs need to be determined for the following expressions

- plane wave propagating in $+z$ direction phase factor
- free-space propagation function
- Fourier transform phase factor
- charge $m = +1$ vortex phase factor

The choice of aforementioned signs will determine the sign of the off-center vortex rotation in a propagating Gaussian beam.

Plane Wave Propagating in $+z$ Direction

The phase factor of a plane wave propagating in $+z$ direction is $\exp[+i\sigma_z kz]$, where σ_z is the chosen sign factor ($\sigma_z = \pm 1$). Goodman,[178] Gaskill[198] and Indebetouw[57] chose $\sigma_z = +1$. For $\sigma_z = +1$ the light propagates in the direction of the phase gradient. For $\sigma_z = -1$ the light propagates *against* the phase gradient. Thus, the kz phase factor in the electric field will have the form:

$$\exp[+i\sigma_z kz] \tag{C.1}$$

The Free-Space Propagation Transfer Function

One can easily show how the transfer function, $H(\rho, z) = \exp[-i\sigma_z \pi\lambda z\rho^2]$, is affected by the choice of σ_z. Here λ is the wavelength and ρ is the radial coordinate in Fourier spatial frequency domain. Following Goodman,[178] we find that the "total" transfer function of wave propagation phenomenon is (Eq. 3-74 in Ref. 178):

$$\mathcal{H}(\rho, z) = \exp\left[i\sigma_z kz\sqrt{1-(\lambda\rho)^2}\right]. \tag{C.2}$$

For paraxial beams $(\lambda\rho)^2 \ll 1$, thus, we can approximate the total transfer function in Eq. (C.2) by the first two terms of the Laurent series:

$$\mathcal{H}(\rho, z) \approx \exp\left[i\sigma_z kz\left(1-\frac{1}{2}(\lambda\rho)^2\right)\right] = \exp[i\sigma_z kz]\exp[-i\sigma_z\pi\lambda z\rho^2]. \tag{C.3}$$

We can re-write it as $\mathcal{H} = \exp[i\sigma_z kz]H(\rho, z)$, where $H(\rho, z) = \exp\left[-i\sigma_z\pi\lambda z\rho^2\right]$. *Note*: we use the script letter $\mathcal{H}$ for the "total" transfer function (which includes the term $\exp[i\sigma_z kz]$) and the itallic capital letter H for the part of the transfer function excluding the term $\exp[i\sigma_z kz]$. In the further discussion we only refer to H.

It is clear from the previous paragraph the sign of the phase in $H(\rho, z)$ should be opposite to the sign of the phase in the plane wave factor $\exp[+i\sigma_z kz]$. Both Goodman[178] and Gaskill[198] adhere to this paradigm. Indebetouw,[57] however, sets both signs to be positive.

Fourier and Fourier-Bessel Transforms

The sign of the phase factor, σ_{FT}, in the Fourier and Fourier-Bessel transforms is *irrelevant* to the propagated field (at least in the case of a Gaussian beam with

$r\exp(\pm i\theta)$ vortices). Obtaining the propagated field involves taking both forward and inverse Fourier (or Fourier-Bessel) transforms and the signs cancel out.

Forward Fourier transform:

$$\mathcal{FT}\{g(x,y)\} = \int\limits_{-\infty}^{\infty}\int\limits_{-\infty}^{\infty} \mathrm{d}x\mathrm{d}y\,\{g(x,y)\exp\left[+\sigma_{\mathrm{FT}}2\pi(f_x x + f_y y)\right]\}\,. \tag{C.4}$$

Inverse Fourier transform:

$$\mathcal{FT}^{-1}\{G(f_x,f_y)\} = \int\limits_{-\infty}^{\infty}\int\limits_{-\infty}^{\infty} \mathrm{d}f_x\mathrm{d}f_y\,\{G(f_x,f_y)\exp\left[-\sigma_{\mathrm{FT}}2\pi(f_x x + f_y y)\right]\}\,. \tag{C.5}$$

Forward Fourier-Bessel transform:

$$\mathcal{FT}\{g(r,\theta)\} = \int\limits_{-\infty}^{\infty} r\mathrm{d}r \oint\limits_{0}^{2\pi} \mathrm{d}\theta\{g(r,\theta)\exp\left[+i\sigma_{\mathrm{FT}}2\pi\rho r\cos(\theta-\phi)\right]\}. \tag{C.6}$$

Inverse Fourier-Bessel transform:

$$\mathcal{FT}^{-1}\{G(\rho,\phi)\} = \int\limits_{-\infty}^{\infty} \rho\mathrm{d}\rho \oint\limits_{0}^{2\pi} \mathrm{d}\phi\{G(\rho,\phi)\exp\left[-i\sigma_{\mathrm{FT}}2\pi\rho r\cos(\theta-\phi)\right]\}, \tag{C.7}$$

where $\sigma_{\mathrm{FT}} = \pm 1$. x,y and f_x, f_y are Cartesian coordinates and spatial frequencies, r,θ and ρ,ϕ are cylindrical coordinates and spatial frequencies, respectively. The choice of σ_{FT} will only affect the field in Fourier plane (imposing a π phase difference). The propagated field is not affected. Goodman[178] and Gaskill[198] chose $\sigma_{\mathrm{FT}} = -1$.

Vortex Phase Term

One can write down the vortex phase term as $\exp[+i\sigma_V]$, where m is the charge of the vortex (signed integer). In the transverse x-y plane a vortex of charge m will have the light circulating in the direction of $\mathrm{Sgn}(\sigma_z\sigma_V m)$ ↺, where $\mathrm{Sgn}(x) = |x|/x$ and ↺ indicates counter-clockwise (CCW) rotation. Let us chose from angular momentum considerations. The angular momentum is going to be positive (i.e. pointing along $+z$) if the light is circulating CCW in the transverse x-y plane as it propagates in the $+z$ direction. If we require charge $m = +1$ vortex to have positive angular momentum, then we want $\sigma_z \sigma_V = 1$, or $\sigma_z = \sigma_V$. If we choose $\sigma_z = -\sigma_V$, then a vortex with positive charge will have negative angular momentum.

The following table shows conventions adopted by various authors:

σ_z	σ_V	Reference No.
$+1$	$+1$	$7, 57, 162, 199$
-1	-1	$14, 158, 200$
-1	$+1$	$56, 84, 85, 90$

Propagated Field

The field of a vortex of charge m initially located at the center of a Gaussian beam can be written as:

$$E(r,\theta,z) = \frac{E_0 (r/w_r)^{|m|}}{\left[1+(z/z_0)^2\right]^{(|m|+1)/2}} \exp\left[-\frac{r^2}{w^2(z)}\right] \exp\left[i\Phi(r,\theta,z)\right], \tag{C.8}$$

where $\Phi(r,\theta,z) = \sigma_V m\theta + \sigma_z\left[-(|m|+1)\arctan(z/z_0) + kr^2/R(z) + kz\right]$, $w(z) = [1+(z/z_0)^2]^{1/2}$ and $1/R(z) = z/(z^2+z_0^2)$.

The field of a vortex of charge $m = \pm 1$ initially located at (r_0, θ_0) may be written as:

$$\begin{aligned} E(r,\theta,z) = & \frac{E_0}{\left[1+(z/z_0)^2\right]^{1/2}} \exp\left[-\frac{r^2}{w^2(z)}\right] \exp\left[i\Phi(r,\theta,z)\right] \\ & \times \frac{1}{w_{\mathrm{V}}}\left[\frac{r\exp[i\Phi_2(\theta,z)]}{(1+(z/z_0)^2)^{1/2}} - r_0\exp[i\sigma_V m\theta_0]\right], \end{aligned} \tag{C.9}$$

where the phases are expressed as $\Phi_1(r,\theta,z) = \sigma_z\left[-\arctan(z/z_0) + kr^2/R(z) + kz\right]$ and $\Phi_2(\theta,z) = \sigma_V m\theta - \sigma_z \arctan(z/z_0)$. The location of the vortex, $(r_{\mathrm{V}},\theta_{\mathrm{V}})$, may be found by requiring both the real and the imaginary parts of the field in equation Eq. (C.9) to be equal to zero, $E(r_{\mathrm{V}},\theta_{\mathrm{V}},z) = 0$. After solving for r_{V} and θ_{V}, we obtain

$$r_{\mathrm{V}} = r_0\left[1 + (z/z_0)^2\right]^{1/2}, \tag{C.10a}$$

$$\theta_{\mathrm{V}} = \theta_0 + \mathrm{Sgn}(\sigma_z\sigma_V m)\arctan(z/z_0). \tag{C.10b}$$

BIBLIOGRAPHY

[1] A. L. Fetter, "Vortices in an Imperfect Bose Gas. I. The Condensate.," Phys. Rev. **138,** A429–A437 (1965).

[2] V. L. Ginzburg and L. P. Pitaevskii, "On the theory of superfluidity," Zh. Eks. Teor. Fiz. **34,** 1240–1245 (1958), [Sov. Phys. JETP **7**, 858-861 (1958)].

[3] L. P. Pitaevskii, "Vortex lines in an imperfect Bose gas," Zh. Eks. Teor. Fiz. **40,** 646–651 (1961), [Sov. Phys. JETP **13**, 451-454 (1961)].

[4] R. J. Donnelly, *Quantized vortices in Helium II* (Cambridge University Press, New York, 1991).

[5] H. J. Lugt, *Vortex Flow in Nature and Technology* (Wiley & Sons, New York, 1983).

[6] P. Coles, *Cosmology; The Origin and Evolution of Cosmic Structure* (Wiley & Sons, New York, 1995).

[7] G. A. Swartzlander, Jr. and C. T. Law, "Optical Vortex Solitons Observed in Kerr Nonlinear Media," Phys. Rev. Lett. **69,** 2503–2506 (1992).

[8] A. W. Snyder, L. Poladian, and D. J. Mitchell, "Stable black self-guided beams of circular symmetry in a bulk Kerr medium," Opt. Lett. **17,** 789–791 (1992).

[9] G. A. Swartzlander, Jr., D. L. Drugan, N. Hallak, M. O. Freeman, and C. T. Law, “Optical transistor effect using an optical vortex soliton,” Laser Physics **5,** 704–709 (1995).

[10] A. Ashkin, “Forces of a single-beam gradient laser trap on a dielectric sphere in array optic regime,” Biophys. J. **61,** 569–582 (1992).

[11] N. B. Simpson, L. Allen, and M. J. Padgett, “Optical tweezers and optical spanners with Laguerre-Gaussian modes,” J. Mod. Opt. **43,** 2485–2491 (1996).

[12] K. T. Gahagan and G. A. Swartzlander, Jr., “Optical vortex trapping of particles,” Opt. Lett. **21,** 827–829 (1996).

[13] G. A. Swartzlander, Jr., A. M. Deykoon, D. W. Jackson, and C. T. Law, “Numerical Modeling of Nonlinear Beam Propagation Phenomena,” In *Materials Research Society symposia proceedings, Materials for Optical Limiting II*, **479,** 269 (1998).

[14] M. W. Beijersbergen, L. Allen, H. E. L. O. van der Veen, and J. P. Woerdman, “Astigmatic laser mode converters and transfer of orbital angular momentum,” Opt. Comm. **96,** 123–132 (1993).

[15] G. A. Turnbull, D. A. Robertson, G. M. Smith, L. Allen, and M. J. Padgett, “The generation of free-space Laguerre-Gaussian modes at millimetre-wave frequencies by use of a spiral phaseplate,” Opt. Comm. **127,** 183–188 (1996).

[16] V. Y. Bazhenov, M. V. Vasnetsov, and M. S. Soskin, “Laser beams with screw dislocations in their wavefronts,” Pis’ma Zh. Eks. Teor. Fiz. **52,** 1037–1039 (1990), [JETP Lett. **52**,429-431 (1990)].

[17] R. Courant and D. Hilbert, *Methods of mathematical physics* (Interscience Publishers, New York, 1953–1962).

[18] S. Ramo, J. R. Whinnery, and T. Van Duzer, *Fields and Waves in Communication Electronics* (Wiley & Sons, New York, 1965).

[19] G. Goubau and F. Schwering, "On the guided propagation of electromagnetic wave beams," IRE Trans. Antennas Propag. **9,** 248–256 (1961).

[20] J. M. Vaughan and D. V. Willetts, "Temporal and interference fringe analysis of TEM^*_{01} laser modes," J. Opt. Soc. Am. **73,** 1018–1021 (1983).

[21] A. G. White, C. P. Smith, N. R. Heckenberg, H. Rubinsztein-Dunlop, R. McDuff, C. O. Weiss, and C. Tamm, "Interferometric measurements of phase singularities in the output of a visible laser," J. Mod. Opt. **38,** 2531–2541 (1991).

[22] E. Abramochkin and V. Volostnikov, "Beam transformations and nontransformed beams," Opt. Comm. **83,** 123–135 (1991).

[23] L. M. Pismen and A. A. Nepomnyashchy, "On interaction of spiral waves," Physica D **54,** 183–193 (1992).

[24] L. A. Lugiato, C. Oldano, and L. M. Narducci, "Cooperative frequency locking and stationary spatial structures in lasers," J. Opt. Soc. Am. B **5,** 879–888 (1988).

[25] P. Coullet, L. Gil, and F. Rocca, "Optical vortices," Opt. Comm. **73,** 403–408 (1989).

[26] G. L. Lippi, T. Ackemann, L. M. Hoffer, A. Gahl, and W. Lange, "Interplay of linear and nonlinear effects in the formation of optical vortices in a nonlinear resonator," Phys. Rev. A **48,** R4043–R4046 (1993).

[27] J. W. Grantham, H. M. Gibbs, G. Khitrova, J. F. Valley, and X. Jianjin, "Kaleidoscopic Spatial Instability: Bifurcations of Optical Transverse Solitary Waves," Phys. Rev. Lett. **66,** 1422–1425 (1991).

[28] C. Tamm and C. O. Weiss, "Bistability and optical switching of spatial patterns in a laser," J. Opt. Soc. Am. B **7,** 1034–1038 (1990).

[29] M. Brambilla *et al.*, "Dynamical transverse laser patterns. I. Theory," Phys. Rev. A **49,** 1427–1451 (1994).

[30] M. Brambilla, F. Battipede, L. A. Lugiato, V. Penna, F. Pratti, C. Tamm, and C. O. Weiss, "Transverse laser patterns. I. Phase singularity crystals.," Phys. Rev. A **43,** 5090–5113 (1991).

[31] G. Indebetouw and D. R. Korwan, "Model of vortices nucleation in a photorefractive phase-conjugate resonator," J. Mod. Opt. **41,** 941–950 (1994).

[32] G. Šlėkys, K. Staliūnas, and C. O. Weiss, "Motion of phase singularities in a class-B laser," Opt. Comm. **119,** 433–446 (1995).

[33] K. Staliūnas and C. O. Weiss, "Nonstationary vortex lattices in large-aperture class B lasers," J. Opt. Soc. Am. B **12,** 1142–1149 (1995).

[34] N. R. Heckenberg, M. Vaupel, J. T. Malos, and C. O. Weiss, "Optical-vortex pair creation and annihilation and helical astigmatism of a nonplanar ring resonator," Phys. Rev. A **54,** 1–10 (1996).

[35] W. J. Firth and A. Lord, "Two-dimensional solitons in a Kerr cavity," J. Mod. Opt. **43,** 1071–1077 (1996).

[36] C. O. Weiss, C. Tamm, and P. Coullet, "Temporal and spatial laser instabilities," J. Mod. Opt. **37,** 1825–1837 (1990).

[37] M. Vaupel and C. O. Weiss, "Circling optical vortices," Phys. Rev. A **51,** 4078–4085 (1995).

[38] K. Staliūnas, "Dynamics of optical vortices in a laser beam," Opt. Comm. **90,** 123–127 (1992).

[39] K. Staliūnas, "Optical vortices during three-way nonlinear coupling," Opt. Comm. **91,** 82–86 (1992).

[40] K. Staliūnas, A. Beržanskis, and V. Jarutis, "Vortex statistics in optical speckle fields," Opt. Comm. **120,** 23–28 (1995).

[41] C. O. Weiss, H. R. Telle, and K. Staliūnas, "Restless optical vortex," Phys. Rev. A **47,** R1616–R1619 (1993).

[42] D. Y. Tang, N. R. Heckenberg, and C. O. Weiss, "Phase-dependent helical pattern formation in a laser," Opt. Comm. **114,** 95–100 (1995).

[43] V. B. Taranenko, K. Staliūnas, and C. O. Weiss, "Spatial soliton laser: Localized structures in a laser with a saturable absorber in a self-imaging resonator," Phys. Rev. A **56,** 1582–1591 (1997).

[44] J. F. Nye and M. V. Berry, "Dislocations in wave trains," Proc. R. Soc. Lond. A **336,** 165–190 (1974).

[45] M. V. Berry, "Singularities in Waves and Rays," in *Physics of Defects*, *Les Houches Sessions XXXV*, R. Balian, M. Kleman, and J.-P. Poirier, eds., (North Holland, Amsterdam, 1981), pp. 453–543.

[46] N. B. Baranova, B. Ya. Zel'dovich, A. V. Mamaev, N. F. Pilipetskii, and V. V. Shkunov, "Dislocations of the wavefront of a speckle-inhomogeneous field (theory and experiment)," Pis'ma Zh. Eks. Teor. Fiz. **33,** 206–210 (1981), [JETP Lett. **33**, 195-199 (1981)].

[47] N. B. Baranova, A. V. Mamaev, N. F. Pilipetsky, V. V. Shkunov, and B. Ya. Zel'dovich, "Wave-front dislocations: topological limitations for adaptive systems with phase conjugation," J. Opt. Soc. Am. **73,** 525–528 (1983).

[48] N. R. Heckenberg, R. McDuff, C. P. Smith, and A. G. White, "Generation of optical phase singularities by computer-generated holograms," Opt. Lett. **17,** 221–223 (1992).

[49] F. S. Roux, "Diffractive optical implementation of rotation transform performed by using phase singularities," Appl. Opt. **32,** 3715–3719 (1993).

[50] F. S. Roux, "Branch-point diffractive optics," J. Opt. Soc. Am. A **11,** 2236–2243 (1994).

[51] Z. S. Sacks, *Construction of Vortex Phase Holograms*, Master's thesis, Worcester Polytechnic Institute, Worcester, MA, 1995.

[52] Z. S. Sacks, D. Rozas, and G. A. Swartzlander, Jr., "Holographic formation of optical vortex filaments," J. Opt. Soc. Am. B **15,** 2226–2234 (1998).

[53] V. Y. Bazhenov, M. S. Soskin, and M. V. Vasnetsov, “Screw dislocations in light wavefronts,” J. Mod. Opt. **39,** 985–990 (1992).

[54] S. N. Khonina, V. V. Kotlyar, M. V. Shinkaryev, V. A. Soifer, and G. V. Uspleniev, “The phase rotor filter,” J. Mod. Opt. **39,** 1147–1154 (1992).

[55] N. R. Heckenberg, R. McDuff, C. P. Smith, H. Rubinsztein-Dunlop, and M. J. Wegener, “Laser beams with phase singularities,” Opt. Quant. Electr. **24,** S951–S962 (1992).

[56] I. V. Basistiy, V. Y. Bazhenov, M. S. Soskin, and M. V. Vasnetsov, “Optics of light beams with screw dislocations,” Opt. Comm. **103,** 422–428 (1993).

[57] G. Indebetouw, “Optical vortices and their propagation,” J. Mod. Opt. **40,** 73–87 (1993).

[58] M. W. Beijersbergen, R. P. C. Coerwinkel, M. Kristensen, and J. P. Woerdman, “Helical-wavefront laser beams produced with a spiral phaseplate,” Opt. Comm. **112,** 321–327 (1994).

[59] F. B. de Colstoun, G. Khitrova, A. V. Fedorov, T. R. Nelson, C. Lowry, T. M. Brennan, B. G. Hammons, and P. D. Maker, “Transverse modes, vortices and vertical-cavity surface-emitting lasers,” Chaos, Solitons & Fractals **4,** 1575–1596 (1994).

[60] L. G. Gouy, “Sur une propriete nouvelle des ondes lumineuses,” Compt. Rend. Acad. Sci. Paris **110,** 1251–1253 (1890).

[61] L. G. Gouy, “Sur la propagation anomale des ondes,” Ann. Chim. Phys. Ser. 6 **24,** 145–213 (1891).

[62] I. Freund, N. Shvartsman, and V. Freilikher, “Optical dislocation networks in highly random media,” Opt. Comm. **101,** 247–264 (1993).

[63] I. Freund, “Optical vortices in Gaussian random wave fields: statistical probability densities.,” J. Opt. Soc. Am. A **11,** 1644–1652 (1994).

[64] N. Shvartsman and I. Freund, “Vortices in Random Wave Fields: Nearest Neighbor Anticorrelations,” Phys. Rev. Lett. **72,** 1008–1011 (1994).

[65] I. Freund and N. Shvartsman, “Wave-field phase singularities: The sign principle,” Phys. Rev. A **50,** 5164–5172 (1994).

[66] N. Shvartsman and I. Freund, “Wave-field phase singularities: near-neighbor correlations and anticorrelations,” J. Opt. Soc. Am. A **11,** 2710–2718 (1994).

[67] I. Freund and N. Shvartsman, “Structural correlations in Gaussian random wave fields,” Phys. Rev. E **51,** 3770–3773 (1995).

[68] N. Shvartsman and I. Freund, “Speckle spots ride phase saddles sidesaddle,” Opt. Comm. **117,** 228–234 (1995).

[69] I. Freund, “Saddles, singularities, and extrema in random phase fields,” Phys. Rev. E **52,** 2348–2360 (1995).

[70] I. Dana and I. Freund, “Vortex-lattice wave fields,” Opt. Comm. **136,** 93–113 (1997).

[71] I. Freund, “Critical-point level-crossing geometry in random wave fields,” J. Opt. Soc. Am. A **14,** 1911–1927 (1997).

[72] I. Freund and V. Freilikher, “Parameterization of anisotropic vortices,” J. Opt. Soc. Am. A **14,** 1902–1910 (1997).

[73] I. Freund, “Vortex derivatives,” Opt. Comm. **137,** 118–126 (1997).

[74] I. Freund, “Intensity critical point correlation functions in random wave fields,” Opt. Comm. **128,** 315–324 (1996).

[75] I. Freund, “Critical point explosions in two-dimensional wave fields,” Opt. Comm. (1999).

[76] B. Ya. Zel’dovich, N. F. Pilipetsky, and V. V. Shkunov, *Principles of Phase Conjugation* (Springer-Verlag, New York, 1985).

[77] G. A. Swartzlander, Jr. and C. T. Law, “The Optical Vortex Soliton,” Optics & Photonics News **4,** 10 (1993).

[78] C. T. Law and G. A. Swartzlander, Jr., “Optical vortex solitons and the stability of dark solitons stripes,” Opt. Lett. **18,** 586–588 (1993).

[79] A. V. Mamaev, M. Saffman, D. Z. Anderson, and A. A. Zozulya, “Propagation of light beams in anisotropic nonlinear media: From symmetry breaking to spatial turbulence,” Phys. Rev. A **54,** 870–879 (1996).

[80] A. V. Mamaev, M. Saffman, and A. A. Zozulya, “Propagation of Dark Stripe Beams in Nonlinear Media: Snake Instability and Creation of Optical Vortices,” Phys. Rev. Lett. **76,** 2262–2265 (1996).

[81] V. Tikhonenko, J. Christou, B. Luther-Davies, and Y. S. Kivshar, “Observation

of vortex solitons created by the instability of dark soliton stripes," Opt. Lett. **21,** 1129–1131 (1996).

[82] B. Luther-Davies, J. Chirstou, V. Tikhonenko, and Y. S. Kivshar, "Optical vortex solitons: experiment versus theory," J. Opt. Soc. Am. B **14,** 3045–3053 (1997).

[83] E. A. Kuznetsov and S. K. Turitsyn, "Instability and collapse of solitons in media with a defocusing nonlinearity," Zh. Eks. Teor. Fiz. **94,** 119–129 (1988), [Sov. Phys. JETP **67**, 1583-1588 (1988)].

[84] F. S. Roux, "Dynamical behavior of optical vortices," J. Opt. Soc. Am. B **12,** 1215–1221 (1995).

[85] D. Rozas, C. T. Law, and G. A. Swartzlander, Jr., "Propagation dynamics of optical vortices," J. Opt. Soc. Am. B **14,** 3054–3065 (1997).

[86] A. Sommerfeld, *Mechanics of Deformable Bodies* (Academic Press, London, 1950).

[87] L. M. Milne-Thomson, *Theoretical Hydrodynamics* (MacMillan, New York, 1968).

[88] H. Lamb, *Hydrodynamics* (Cambridge Univ. Press, Cambridge, 1993), p. 220.

[89] G. A. Swartzlander, Jr., Z. S. Sacks, X. Zhang, D. Rozas, and C. T. Law, "Formation and propagation of optical vortices," In *International Quantum Electronics Conference*, OSA Technical Digest, p. 31 (Optical Society of America, Washington, D. C., 1996).

[90] D. Rozas, Z. S. Sacks, and G. A. Swartzlander, Jr., "Experimental Observation of Fluidlike Motion of Optical Vortices," Phys. Rev. Lett. **79,** 3399–3402 (1997).

[91] D. Rozas and G. A. Swartzlander, Jr., "Enhanced Vortex Rotation in Nonlinear Refractive Media," In *Quantum Electronics and Laser Science Conference*, OSA Technical Digest, p. 100 (Optical Society of America, Washington, D.C., 1999).

[92] D. Rozas and G. A. Swartzlander, Jr., "Enhanced Rotation of Optical Vortex Solitons," in preparation (1999).

[93] T. Ackemann, E. Kriege, and W. Lange, "Phase singularities via nonlinear beam propagation in sodium vapor," Opt. Comm. **115,** 339–346 (1995).

[94] A. V. Ilyenkov, A. I. Khizhnyak, L. V. Kreminskaya, M. S. Soskin, and M. V. Vasnetsov, "Birth and evolution of wave-front dislocations in a laser beam passed through a photorefractive $\mathrm{LiNbO_3 : Fe}$ crystal," Appl. Phys. B **62,** 465–471 (1996).

[95] A. V. Ilyenkov, L. V. Kremninskaya, M. S. Soskin, and M. V. Vasnetsov, "Birth, evolution and annihilation of phase singularities in the propagation of a laser beam passed through a self-focusing Strontium Barium Niobate crystal," Journal of Nonlinear Optical Physics and Materials **6,** 169–180 (1997).

[96] L. V. Kreminskaya, M. S. Soskin, and A. I. Khizhnyak, "The Gaussian lenses give birth to optical vortices in laser beams," Opt. Comm. **145,** 377–384 (1998).

[97] L. V. Kreminskaya, M. S. Soskin, and A. I. Khizhnyak, "Gaussian lenses initiate

optical vortices in laser beams during self-action in Kerr-like medium," Chaos, Solitons & Fractals **10,** 737–744 (1999).

[98] A. M. Deykoon, M. S. Soskin, and G. A. Swartzlander, Jr., "Nonlinear optical catastrophe from a smooth initial beam," to appear in Opt. Lett. (1999).

[99] F. J. Wright, "The Stokes set of the cusp diffraction catastrophe," J. Phys. A: Math. Gen. **13,** 2913–2928 (1980).

[100] J. F. Nye, "Optical caustics in the near field from liquid drops," Proc. R. Soc. Lond. A **361,** 21–41 (1978).

[101] J. F. Nye, "The catastrophe optics of liquid drop lenses," Proc. R. Soc. Lond. A **403,** 1–26 (1986).

[102] J. L. Elliot, R. G. French, E. Dunham, P. J. Gierasch, J. Veverka, C. Church, and S. Carl, "Occultation of ε Geminorum by Mars. II. The structure and extinction of the Martian upper atmosphere," The Astrophysical Journal **217,** 661–679 (1977).

[103] C. S. Gardner, J. M. Greene, M. D. Kruskal, and R. M. Miura, "Method for solving the Korteweg-deVries equation," Phys. Rev. Lett. 19 (1967).

[104] V. E. Zakharov and A. B. Shabat, "Interaction between solitons in a stable medium," Zh. Eks. Teor. Fiz. **64,** 1627–1639 (1973), [Sov. Phys. JETP **37**, 823-828 (1973)].

[105] A. Hasegawa and F. Tappert, "Transmission of stationary nonlinear optical pulses in dispersive dielectric fibers. I. Anomalous dispersion.," Appl. Phys. Lett. **23,** 142–144 (1973).

[106] A. Hasegawa and F. Tappert, “Transmission of stationary nonlinear optical pulses in dispersive dielectric fibers. II. Normal dispersion.,” Appl. Phys. Lett. **23,** 171–172 (1973).

[107] P. L. Kelley, “Self-focusing of optical beams,” Phys. Rev. Lett. **15,** 1005–1007 (1965).

[108] J. P. Gordon, R. C. C. Leite, R. S. Moore, S. P. S. Porto, and J. R. Whinnery, “Long-Transient Effects in Lasers with Inserted Liquid Samples,” J. Appl. Phys. **36,** 3–8 (1965).

[109] R. C. C. Leite, R. S. Moore, and J. R. Whinnery, “Low absorption measurements by means of the thermal lens effect using a He-Ne Laser,” Appl. Phys. Lett. **5,** 141–143 (1964).

[110] R. Y. Chiao, E. Garmire, and C. H. Townes, “Self-trapping of optical beams,” Phys. Rev. Lett. **13,** 479–489 (1964).

[111] W. G. Wagner, H. A. Haus, and J. H. Marburger, “Large-Scale Self-Trapping of Optical Beams in the Paraxial Ray Approximation,” Phys. Rev. **175,** 256–266 (1968).

[112] S. V. Manakov, “Nonlinear Fraunhofer diffraction,” Zh. Eks. Teor. Fiz. **65,** 1392–1398 (1973), [Sov. Phys. JETP **38**, 693-695 (1974)].

[113] S. A. Akhmanov, R. V. Khokhlov, and A. P. Sukhorukov, “Self-Focusing, Self-Defocusing and Self-Modulation of Laser Beams,” in *Laser Handbook*, F. T. Arecchi and E. O. Schulz-Dubois, eds., (North-Holland, Amsterdam, 1972), Vol. 2, pp. 1151–1228.

[114] A. W. McCord, R. J. Ballagh, and J. Cooper, "Dispersive self-focusing in atomic media," J. Opt. Soc. Am. B **5,** 1323–1334 (1988).

[115] G. A. Swartzlander, Jr., H. Yin, and A. E. Kaplan, "Continuous-wave self-deflection effect in sodium vapor," J. Opt. Soc. Am. B **6,** 1317–1325 (1989).

[116] G. A. Swartzlander, Jr., "Dark-soliton prototype devices: analysis by using direct-scattering theory," Opt. Lett. **17,** 493–495 (1992).

[117] G. A. Swartzlander, Jr., D. R. Andersen, J. J. Regan, H. Yin, and A. E. Kaplan, "Spatial Dark-Soliton Stripes and Grids in Self-Defocusing Materials," Phys. Rev. Lett. **66,** 1583–1586 (1991).

[118] G. A. Swartzlander, Jr., D. R. Andersen, and J. J. Regan, "Spatial dark-soliton stripes and grids in self-defocusing materials," Phys. Rev. Lett. **66,** 1583–1585 (1991).

[119] N. B. Abraham and W. J. Firth, "Overview of transverse effects in nonlinear-optical systems," J. Opt. Soc. Am. B **7,** 951–962 (1990).

[120] L. Poladian, A. W. Snyder, and D. J. Mitchell, "Low-interaction solitary waves," Opt. Comm. **91,** 97–98 (1992).

[121] M. Shalaby, F. Reynaud, and A. Barthelemy, "Experimental observation of spatial soliton interactions with a $\pi/2$ relative phase difference," Opt. Lett. **17,** 778–780 (1992).

[122] G. S. McDonald, K. S. Syed, and W. J. Firth, "Optical vortices in beam propagation through a self-defocusing medium," Opt. Comm. **94,** 469–476 (1992).

[123] S.-L. Liu, W.-Z. Wang, and J.-Z. Xu, "(2+1)-dimensional fundamental spatial dark soliton," Appl. Phys. Lett. **66,** 665–666 (1995).

[124] G. S. McDonald, K. S. Syed, and W. J. Firth, "Dark spatial soliton break-up in the transverse plane," Opt. Comm. **95,** 281–288 (1993).

[125] K. Staliūnas, "Vortices and Dark Solitons in the Two-dimensional Nonlinear Schrödinger Equation," Chaos, Solitons & Fractals **4,** 1783–1796 (1994).

[126] D. V. Petrov and L. Torner, "Observation of topological charge pair nucleation in parametric wave mixing," Phys. Rev. E **58,** 7903–7907 (1998).

[127] R. Y. Chiao, I. H. Deutsch, J. C. Garrison, and E. M. Wright, "Solitons in Quantum Nonlinear Optics," in *Frontiers in nonlinear optics : the Serge Akhmanov memorial volume*, H. Walther, ed., (Adam Hilger, Bristol, UK, 1992), pp. 151–182.

[128] E. M. Wright, R. Y. Chiao, and J. C. Garrison, "Optical Anyons: Atoms Trapped on Electromagnetic Vortices," Chaos, Solitons & Fractals **4,** 1797–1803 (1994).

[129] C. T. Law and G. A. Swartzlander, Jr., "Polarized Optical Vortex Solitons: Instabilities and Dynamics in Kerr Nonlinear Media," Chaos, Solitons & Fractals **4,** 1759–1766 (1994).

[130] I. Velchev, A. Dreischuh, D. Neshev, and S. Dinev, "Interactions of optical vortex solitons superimposed on different background beams," Opt. Comm. **130,** 385–392 (1996).

[131] Y. Chen and J. Atai, “Dynamics of optical-vortex solitons in perturbed nonlinear medium,” J. Opt. Soc. Am. B **11,** 2000–2003 (1994).

[132] W. Krolikowski and B. Luther-Davies, “Dark optical solitons in saturable nonlinear media,” Opt. Lett. **18,** 188–190 (1993).

[133] J. Christou, V. Tikhonenko, Y. S. Kivshar, and B. Luther-Davies, “Vortex soliton motion and steering,” Opt. Lett. **21,** 1649–1651 (1996).

[134] Y. S. Kivshar, J. Christou, V. Tikhonenko, B. Luther-Davies, and L. M. Pismen, “Dynamics of optical vortex solitons,” Opt. Comm. **152,** 198–206 (1998).

[135] Y. S. Kivshar and X. Yang, “Perturbation-induced dynamics of dark solitons,” Phys. Rev. E **49,** 1657–1670 (1994).

[136] Y. S. Kivshar and B. Luther-Davies, “Dark optical solitons: physics and applications,” Physics Reports **298,** 81–197 (1998).

[137] D. V. Scriabin and W. J. Firth, “Dynamics of self-trapped beams with phase dislocation in saturable Kerr and quadratic nonlinear media,” Phys. Rev. E **58,** 3916–3930 (1998).

[138] G. H. Kim, J. H. Jeon, Y. C. Noh, K. H. Ko, H. J. Moon, J. H. Lee, and J. S. Chang, “An array of phase singularities in a self defocusing medium,” Opt. Comm. **147,** 131–137 (1998).

[139] D. Neshev, A. Dreischuh, M. Assa, and S. Dinev, “Motion control of ensembles of ordered optical vortices generated on finite extent background,” Opt. Comm. **151,** 413–421 (1998).

[140] M. S. El Naschie, ed., "Special Issue: Nonlinear Optical Structures, Patterns, Chaos," Chaos, Solitons & Fractals **4**, No. 8/9 (1994).

[141] A. M. Deykoon and G. A. Swartzlander, Jr., "The pinched optical vortex soliton," in preparation (1999).

[142] B. Luther-Davies, R. Powles, and V. Tikhonenko, "Nonlinear rotation of three-dimensional dark spatial solitons in a Gaussian laser beam," Opt. Lett. **19,** 1816–1818 (1994).

[143] G. Duree, M. Morin, G. Salamo, M. Segev, B. Crosignani, P. DiPorto, E. Sharp, and A. Yariv, "Dark photorefractive spatial solitons and photorefractive vortex solitons," Phys. Rev. Lett. **74,** 1978–1981 (1995).

[144] A. V. Mamaev, M. Saffman, and A. A. Zozulya, "Vortex evolution and bound pair formation in anisotropic nonlinear optical media," Phys. Rev. Lett. **77,** 4544–4547 (1998).

[145] G. Duree, M. Morin, G. Salamo, M. Segev, B. Crosignani, P. Di Porto, E. Sharp, and A. Yariv, "Dark Photorefractive Spatial Solitons and Photorefractive Vortex Solitons," Phys. Rev. Lett. **74,** 1978–1981 (1995).

[146] J. Feinberg, "Asymmetric self-defocusing of an optical beam from the photorefractive effect," J. Opt. Soc. Am. **72,** 46–51 (1982).

[147] K. T. Gahagan, *Optical manipulation of microparticles and biological structures*, Ph.D. thesis, Worcester Polytechnic Institute, Worcester, MA, 1998.

[148] C. S. Buer, K. T. Gahagan, G. A. Swartzlander, Jr., and P. J. Weathers, "Insertion of Microscopic Objects Through Plant Cell Walls Using Laser Microsurgery," Biotechnology and Bioengineering (1998).

[149] G. A. Askar'yan, "Effects of the gradient of a strong electromagnetic beam on electrons and atoms," Sov. Phys. JETP **15,** 1088–1090 (1962).

[150] M. E. J. Friese, J. Enger, H. Rubinsztein-Dunlop, and N. R. Heckenberg, "Optical angular-momentum transfer to trapped absorbing particles," Phys. Rev. A **54,** 1593–1596 (1996).

[151] H. He, M. E. J. Friese, N. R. Heckenberg, and H. Rubinsztein-Dunlop, "Direct Observation of Transfer of Angular Momentum to Absorptive Particles from a Laser Beam with a Phase Singularity," Phys. Rev. Lett. **75,** 826–829 (1995).

[152] H. He, N. R. Heckenberg, and H. Rubinsztein-Dunlop, "Optical particle trapping with higher-order doughnut beams produced using high-efficiency computer generated holograms," J. Mod. Opt. **42,** 217–223 (1995).

[153] K. T. Gahagan and G. A. Swartzlander, Jr., "Simultaneous Trapping of Low-index and High-Index Microparticles With an Optical Vortex Trap," J. Opt. Soc. Am. B **16,** 533–537 (1999).

[154] N. B. Simpson, K. Dholakia, L. Allen, and M. J. Padgett, "Mechanical equivalent of spin and orbital angular momentum of light: an optical spanner," Opt. Lett. **22,** 52–54 (1997).

[155] A. Ashkin, J. M. Dziedzic, J. E. Bjorkholm, and S. Chu, "Observation of a

single-beam gradient force optical trap for dielectric particles," Opt. Lett. **11,** 288–290 (1986).

[156] K. Sasaki, M. Koshioka, H. Misawa, N. Kitamura, and H. Masuhara, "Optical trapping of a metal particle and a water droplet by a scanning laser beam.," Appl. Phys. Lett. **60,** 807–809 (1992).

[157] K. T. Gahagan and G. A. Swartzlander, Jr., "Trapping of Low-index Microparticles in an Optical Vortex," J. Opt. Soc. Am. B **15,** 524–534 (1998).

[158] L. Allen, M. W. Beijersbergen, R. J. C. Spreeuw, and J. P. Woerdman, "Orbital angular momentum and the transformation of Laguerre-Gaussian modes," Phys. Rev. A **45,** 8185–8189 (1992).

[159] K. Dholakia, N. B. Simpson, M. J. Padgett, and L. Allen, "Second-harmonic generation and the orbital angular momentum of light," Phys. Rev. A **54,** R3742–R3745 (1996).

[160] A. Beržanskis, A. Matijošius, A. Piskarkas, V. Smilgevičius, and A. Stabinis, "Conversion of topological charge of optical vortices in a parametric frequency converter," Opt. Comm. **140,** 273–276 (1997).

[161] P. Di Trapani, A. Beržanskis, S. Minardi, S. Sapone, and W. Chinaglia, "Observation of optical vortices and J(0) Bessel-like beams in quantum-noise parametric amplification," Phys. Rev. Lett. **81,** 5133–5136 (1998).

[162] M. S. Soskin and M. V. Vasnetsov, "Nonlinear singular optics," Pure App. Opt. **7,** 301–311 (1998).

[163] I. D. Maleev, A. M. Deykoon, G. A. Swartzlander, Jr., M. S. Soskin, and A. V. Sergienko, “Violation of conservation of topological charge in optical down conversion,” In *Quantum Electronics and Laser Science Conference*, OSA Technical Digest, p. 99 (Optical Society of America, Washington, D.C., 1999).

[164] J. Courtial, K. Dholakia, D. A. Robertson, L. Allen, and M. J. Padgett, “Measurement of the Rotational Frequency Shift Imparted to a Rotating Light Beam Possessing Orbital Angular Momentum,” Phys. Rev. Lett. **80,** 3217–3219 (1998).

[165] M. Born and E. Wolf, *Principles of optics*, 6th ed. (Cambridge U. Press, New York, 1997).

[166] H. Kogelnik, “Coupled wave theory for thick hologram gratings,” Bell Syst. Tech. J. **48,** 2909–2947 (1969).

[167] W. J. Gambogi, A. M. Weber, and T. J. Trout, “Advances and applications of DuPont holographic photopolymers,” in *Photopolymers: Physics, Chemistry, and Applications*, Vol. 114 of *SPIE milestone series*, R. A. Lessard and G. Manivannan, eds., (1995), pp. 375–386.

[168] W. J. Gambogi, W. A. Gerstadt, S. R. Mackara, and A. M. Weber, “Holographic transmission elements using improved photopolymer films,” Proc. SPIE **1555,** 256–266 (1991).

[169] J. A. Cox, “Diffraction efficiency of binary optical elements,” In *Computer and Optically Formed Holographic Elements*, I. Cindrich and S. Lee, eds., Proc. SPIE **1211,** 116–124 (1990).

[170] J. A. Cox, B. S. Fritz, and T. Werner, "Process-dependent kinoform performance," In *Holographic Optics III: Principles and Applications*, G. M. Morris, ed., Proc. SPIE **1507,** 100–109 (1991).

[171] M. W. Farn and J. W. Goodman, "Effect of VLSI fabrication errors on kinoform efficiency," In *Computer and Optically Formed Holographic Elements*, I. Cindrich and S. Lee, eds., Proc. SPIE **1211,** 125–136 (1990).

[172] S. Babin and V. Danilov, "Variable shaped electron-beam lithography application to subwavelength and computer generated diffractive optics fabrication," Journal of vacuum science and technology. B, Microelectronics processing and phenomena **13,** 2767–2771 (1995).

[173] E. Di Fabrizio, L. Grella, M. Baciocchi, M. Gentili, D. Peschiaroli, L. Mastrogiacomo, and R. Maggiora, "One step electron-beam lithography for multipurpose diffractive optical elements with 200 nm resolution.," Journal of vacuum science and technology. B, Microelectronics processing and phenomena **14,** 3855–3859 (1996).

[174] J. A. Cox, J. Gieske, K. Hewitt, and T. R. Werner, "CO-OP DOE Foundry Process Error Summary," Technical report, Honeywell Technology Center, 3660 Technology Drive, Minneapolis, Minnesota 55418 (1996) , also available at http://co-op.gmu.edu/workshops/doe/page9.html.

[175] G. J. Swanson, "Binary Optics Technology: The Theory and Design of Multilevel Diffractive Optical Elements," Technical Report No. 854, MIT Lincoln Laboratory (1989) .

[176] P.-G. de Gennes, *Superconductivity of Metals and Alloys* (Addison-Wesley, Reading, MA, 1989), pp. 177–182.

[177] A. E. Siegman, *Lasers* (University Science Books, Mill Valley, CA, 1986).

[178] J. W. Goodman, *Introduction to Fourier Optics*, 2^{nd} ed. (McGraw-Hill, New York, 1996).

[179] G. A. Swartzlander, Jr., "Optical Vortex Filaments," in *Optical Vortices*, Vol. 228 of *Horizons in World Physics*, M. V. Vasnetsov and K. Staliūnas, eds., (Nova Science, 1999).

[180] C. Nore, M. E. Brachet, and S. Fauve, "Numerical study of hydrodynamics using the nonlinear Schrödinger (NLS) equation," Physica D **65,** 154–162 (1993).

[181] R. Betchov, "On the curvature and torsion of an isolated vortex filament," J. Fluid Mech. **22,** 471–479 (1965).

[182] M. D. Feit and J. A. Fleck, Jr., "Light propagation in graded-index optical fibers," Appl. Opt. **17,** 3990–3998 (1978).

[183] E. B. McLeod, *Introduction to Fluid Dynamics* (MacMillan, New York, 1963).

[184] B. E. A. Saleh and M. C. Teich, in *Fundamentals of Photonics*, *Wiley Series in Pure and Applied Optics*, J. W. Goodman, ed., (Wiley & Sons, New York, 1991).

[185] P. M. Morse and H. Feshbach, *Methods of Theoretical Physics* (McGraw-Hill, New York, 1953).

[186] P. Ao and D. J. Thouless, “Berry’s Phase and the Magnus Force for a Vortex Line in a Superconductor,” Phys. Rev. Lett. **70,** 2158–2161 (1993).

[187] E. B. Sonin, “Magnus force in superfluids and superconductors,” Phys. Rev. B **55,** 485–501 (1997).

[188] B. N. Bolotovskii and S. N. Stolyarov, “Optical Analog of the Magnus effect,” Pis’ma Zh. Eks. Teor. Fiz. **25,** 148–150 (1977), [Sov. Phys. JETP Lett. **25**, 135-137 (1977)].

[189] A. V. Dugin, B. Ya. Zel’dovich, N. D. Kundikova, and V. S. Lieberman, “Optical analog of Magnus effect,” Zh. Eks. Teor. Fiz. **100,** 1474–1482 (1991), [Sov. Phys. JETP **73**, 816-820 (1991)].

[190] M. Stone, “Spectral flow, Magnus force, and mutual friction via the geometric optics limit of Andreev reflection,” Phys. Rev. B **54,** 13222–13229 (1996).

[191] W. H. Press, S. A. Teukolsky, W. T. Vetterling, and B. P. Flannery, *Numerical Recipes in C*, 2^{nd} ed. (Cambridge University Press, New York, 1992).

[192] J. W. Cooley and J. W. Tukey, “An Algorithm for the Machine Calculation of Complex Fourier Series,” Mathematics of Computation **19,** 297–301 (1965).

[193] E. O. Brigham, *The Fast Fourier Transform* (Prentice-Hall, Eaglewood Ciffs, NJ, 1974).

[194] G. C. Danielson and C. Lanczos, “Some improvements in practical Fourier analysis and their application to X-ray scattering from liquids,” J. Franklin Institute **233,** 365–380 and 435–452 (1942).

[195] W. W. Clendenin, “Fresnel diffraction of the plane phase grating,” J. Opt. Soc. Am. **53,** 267–273 (1963).

[196] J. T. Winthrop and C. R. Worthington, “Theory of Fresnel images. I. Plane periodic objects in monochromatic light,” J. Opt. Soc. Am. **55,** 373–381 (1965).

[197] A. C. Newell and J. V. Moloney, *Nonlinear optics* (Addison-Wesley, Redwood City, Calif., 1992).

[198] J. D. Gaskill, *Linear Systems, Fourier Transforms and Optics* (Wiley & Sons, New York, 1978), p. 320.

[199] M. S. Soskin, V. N. Gorshkov, M. V. Vasnetsov, J. T. Malos, and N. R. Heckenberg, “Topological charge and angular momentum of light beams carrying optical vortices,” Phys. Rev. A **56,** 4064–4074 (1997).

[200] M. J. Padgett and L. Allen, “The Poynting vector in Laguerre-Gaussian laser modes,” Opt. Comm. **121,** 36–40 (1995).